LAGRANGIAN METHODS OF COSMIC WEB CLASSIFICATION

Justin David Fisher

UNIVERSITY OF THE
WITWATERSRAND,
JOHANNESBURG

A Research Report submitted to the Department of Physics, Faculty of Science, University of the Witwatersrand, Johannesburg, in partial fulfilment of the requirements for the degree of Master of Science.

Signed on the 24^{th} March 2016 in Johannesburg.

Declaration

I declare that this Research Report is my own, unless otherwise indicated. It is being submitted for the Degree of Master of Science at the University of the Witwatersrand, Johannesburg. It has not been submitted before for any degree or examination at any other University.

(Justin David Fisher)

on the 4^{th} day of June 2016 in Johannesburg

Abstract

This research report uses cosmological N-body simulations to examine the the large scale mass distribution of the Universe, known as the cosmic web. The cosmic web can be classified into nodes, filaments, sheets and voids - each with its own characteristic density and velocity fields. In this work, the author proposes a new Lagrangian cosmic web classification algorithm, based on smoothed particle hydrodynamics. This scheme offers adaptive resolution, resolves smaller substructure and obeys similar statistical properties with existing Eulerian methods. Using the new classification scheme, halo clustering dependence on cosmic web type is examined. The author finds halo clustering is significantly correlated with web type. Consequently, the mass dependence of halo clustering may be explained by the fractions of web types found for a particular halo mass. Finally, an analysis of dark matter halo spin, shape and fractional anisotropy is presented per web type to suggest avenues for future work.

Dedication

To my family.
To Dad and Wouter for encouraging me.
To Danielle for your unwavering support and your lonely nights.

Acknowledgements

I would like to acknowledge the generous support from the National Astrophysics and Space Science Programme (NASSP). A fantastic programme that has allowed me to achieve things I never thought I would. From funding to friendships and all the coursework in between, it has truly been a life changing journey. I would also like to thank my supervisor, Professor Andreas Faltenbacher, for his patience, understanding and tireless work ethic. His knowledge, expertise and guidance were crucial to the development of this thesis as well as my own ongoing personal development as a researcher.

Contents

List of Figures

List of Tables

List of Symbols, Acronyms

- DM - Dark Matter
- SPH - Smoothed particle hydrodynamics
- FOF - Friends of friends
- PBC - Periodic boundary conditions
- $\mathbf{r}$ - **Bold** face letters indicate vector quantities
- $\dot{\mathbf{r}}$ - A single dot above a quantity indicates the time derivative $\partial/\partial t$
- $\ddot{\mathbf{r}}$ - A double dot above a quantity indicates the second time derivative $\partial^2/\partial t^2$

1. Introduction

> "Cosmology is among the oldest subjects to captivate our species. And it's no wonder. We're storytellers, and what could be more grand than the story of creation?"
>
> Brian Greene

Cosmology is the study of the origin, evolution and eventual fate of the Universe. One looks to understand the how the Universe came to be, its dynamical structure and its evolution into the future. Cosmological numerical simulations have played a significant role in the development of the well established ΛCDM cosmological theory, particularly in the case of structure formation models, as they bridge the gap between theory and observation (Bertschinger 1998). Models of structure formation begin with initial conditions (i.e. a given cosmological model and a set of cosmological parameters) and are typically solved using gravitational N-body simulations.

The first gravitational N-body simulation was performed by Holmberg (1941) using the flux of 37 light bulbs and an optical computer to display the gravitational interactions between galaxies. With the advent of the digital computer came the numerical revolution, allowing von Hoerner (1960) and Aarseth & Hoyle (1963) to perform N-body simulations of $\sim$100 particles, exploring stellar dynamics and galaxy clustering respectively.

As technology progressed with Moore's law, so too did the size of the simulations. Larger simulations to test clustering and structure formation were performed by Peebles (1970), who observed the interactions of galaxies within a cluster resemble a simulated cloud of particles with no initial velocities undergoing gravitational collapse. White (1976) proved that dark matter cannot reside inside galaxies by simulating the collapse of 700 particles with unequal mass. The results showed that if one assigns the mass of the cluster to individual galaxies, two-body scattering takes place that prevents the natural clustering one expects.

The seminal work of Press & Schechter (1974) offered new ideas about cosmological evolution. By using a simulation of 1000 bodies, Press & Schechter (1974) found one is able to describe the number of objects (e.g. galaxies, clusters) within a given mass bin, within a Universal volume through hierarchical structure formation. Structure formation models rely on the ability to adequately set up initial conditions and solve the N-body interactions through time.

1.1. The Cosmic Web

The early Universe is said to be homogeneous and isotropic with small density perturbations that undergo gravitational collapse producing the web-like structure one observes today. This process can be described using the Zeldovich theory (Zel'dovich 1970) of pancaking whereby the medium undergoes gravitational collapse into planar sheets or pancakes. These sheets flow into filaments, finally intersecting in the nodes. The baryonic matter traces the DM distribution with galaxies flowing through the sheets and filaments. Galaxy clusters form where these flows coalesce within the nodes.

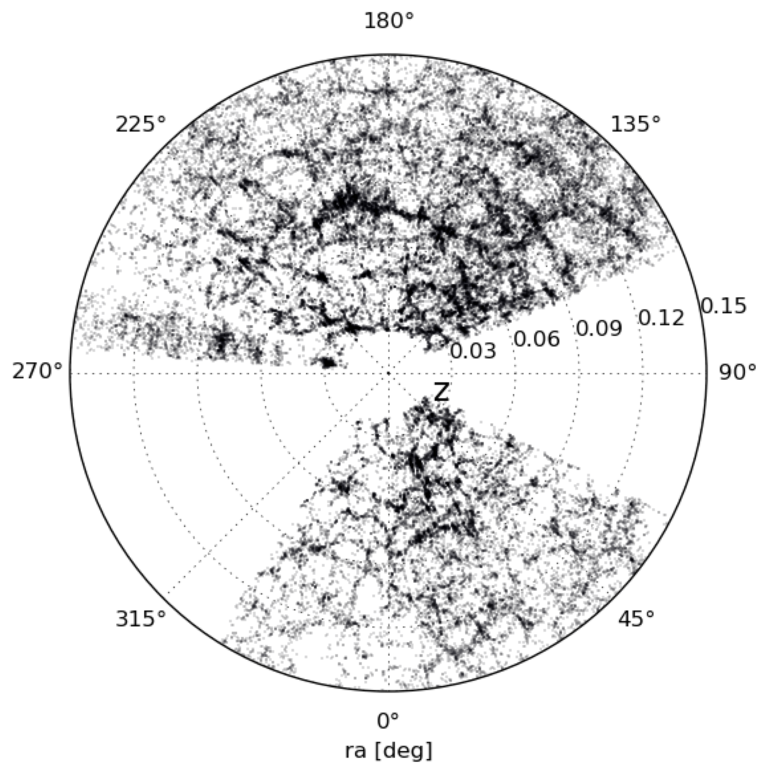

Fig. 1.— The equatorial distribution of 85 000 galaxies up to redshift z = 0.15 projected onto the declination axis. The large scale structure of the Universe is evident as darker regions signal overdensities while lightly-shaded regions devoid of galaxies signify underdense regions. Regions of over and underdensity can be classified into distinct web types. Data is provided by Ivezić et al. (2014).

Bond et al. (1996) coined the term 'cosmic web' to describe the large scale distribution of matter in the Universe. The cosmic web is characterised by its filamentary structure with regions of increasing density, classified as voids, sheets, filaments and nodes respectively.

N-body simulations can be used to replicate the gravitational collapse of Dark matter (DM) particles in accordance with the ΛCDM model through which one gains an understanding of structure formation and the role the environment plays on galaxy formation and evolution.

N-body simulations and galaxy redshift surveys such as the cfA (Huchra et al. 1983), 2dF (Colless et al. 2001) and SDSS (York et al. 2000) show a remarkable statistical correlation in the distribution of matter. Observe Fig. 1, a spectroscopic sample of 85 000 SDSS galaxies between a declination angle of -0.17 and 1.12 degrees, taken from the SDSS Data Release 8. Data is provided by Ivezić et al. (2014).

One is able to observe the distribution of galaxies out to a redshift of 0.15 in Figure 1. This shows the large scale structure of the Universe with very overdense (dark) regions being classified as filaments and the lightly-shaded regions signal underdense web types such as sheets and voids. Visually, moving from $z = 0.15 \rightarrow z = 0$ in Fig. 1 is very similar to the evolution of the Gadget-2 simulation seen in Fig. 4, albeit on a much smaller evolution scale. Galaxies are significantly more clumped together in darker regions at smaller redshifts while sparsely distributed at higher redshifts.

Galaxy properties have already been shown to vary with environment (e.g. Dressler 1980; Blanton et al. 2005; Gao et al. 2005b; Faltenbacher et al. 2009) and classifying the cosmic web allows one to explore further how different web types affect halo properties (Hahn et al. 2007b,a; Aragón-Calvo et al. 2007b; Libeskind et al. 2012b,a) and the galaxies within the halos (Nuza et al. 2014; Metuki et al. 2014) to probe the poorly understood processes underlying how galaxies are formed from a homogeneous Universe and how galaxies then evolve over time.

1.2. Classification Algorithms

Classifying the cosmic web using dynamical information was first proposed by Hahn et al. (2007b) and Aragón-Calvo et al. (2007a), later elaborated by Forero-Romero et al. (2009). The basic algorithm constructs a mesh inside the cosmological volume and for each cell calculates the tidal tensor

$$T_{ij} = \frac{\partial^2 \phi}{\partial r_i \partial r_j} \tag{1}$$

The tidal tensor is constructed using the Hessian of the gravitational potential and fully describes the linear dynamics of the local density field (Hahn et al. 2007b). Since T_{ij} is symmetric, the eigenvalues of the the tidal tensor are real and the number of positive eigenvalues greater than zero allows one to classify the cosmic web. Void, sheet, filament and node mesh cells have 0, 1, 2 and 3 positive eigenvalues respectively Hahn et al. (2007b).

More complex and sophisticated algorithms have since been developed. Aragón-Calvo et al. (2010a) used the SpineWeb Framework to identify topologically substructure using the Watershed algorithm (Platen et al. 2007), tracing the density field between voids, known as 'watershed basins'.

The Origami phase space classifier, given by Falck et al. (2012), is Lagrangian in nature and counts the number of folds that a three dimensional Lagrangian manifold undergoes in six dimensional phase. Aragón-Calvo et al. (2007a, 2010b) and Sousbie (2011) have borrowed techniques from discrete Morse theory (Colombi et al. 2000) and Delaunay Tessellation (Schaap & van de Weygaert 2000) to classify cosmological density fields into its constituent substructures.

This research report will concentrate on the classification algorithm given by Hoffman et al. (2012) who compared the classification scheme based on tidal torque theory, dubbed the 'T-web', versus a new classification method based on velocity shear tensor, also known as the 'V-web'.

Hoffman et al. (2012) based the analysis on the mass conservation equation[1] seen in Eq. 2, and showed that the two fields that characterise the simulation, namely the density and velocity field are intimately related.

$$\frac{1}{\rho}\frac{D\rho}{Dt} = -(\nabla\cdot\mathbf{v}) \tag{2}$$

The divergence is defined as the flux of some medium, per unit volume, through a closed surface. A cubic fluid element that has a outward flow or positive divergence can be seen by the black arrows in Fig 2. Conversely, a negative divergence results in an inward flow shown by the red arrows so that negative divergence results in compression of the fluid element while positive divergence is associated with an expansion of the fluid element.

Hoffman et al. (2012) provides evidence for a one-to-one correspondence between voids and a positive divergent velocity field. Velocity divergence is demonstrated to strongly trace the density field. The seminal work by Bond et al. (1996) showed that the filamentary structure of the cosmic web is a result of the strain of the DM fluid. The velocity shear tensor is of particular interest as the diagonal elements represent the strain (rate of compression or expansion) along a given eigenvector. The 'V-web' classification method is a similar mesh based construction as the tidal based scheme. It differs in that one obtains the eigenvalues of the velocity shear tensor. The classification is then performed using a visually defined threshold value, often chosen to be greater than zero.

[1] $\frac{D\rho}{Dt} = \frac{\partial\rho}{\partial t} + \mathbf{v}\cdot\nabla\rho$ is the comoving derivative

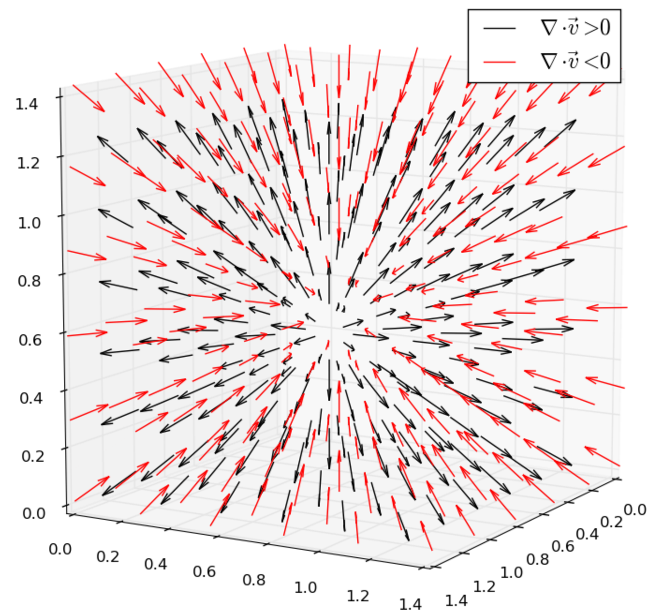

Fig. 2.— Positive (black arrows) and negative (red arrows) divergence showing the outward and inward flow respectively.

1.3. Aim & Objectives

The aim of this research report is to to reproduce the cosmic web classification 'V-web' results found by Hoffman et al. (2012) using Eulerian mesh based techniques. This is to offer comparison for a newly proposed Lagrangian classification scheme using techniques borrowed from smoothed particle hydrodynamics (SPH).

The research report is organised as follows: A description of the background information regarding N-body simulations and their methods, including the GADGET-2 and halo finding codes used for cosmological simulations within, can be found in Section 2.1. A brief introduction into the SPH formalism can be found in Section 3. In Section 4, the SPH based velocity shear tensor classification scheme is developed and the results are compared with the Eulerian based 'V-web' classification scheme.

N-body simulations have long since been used to test cosmological theories of formation of structure formation and clustering (e.g., Klypin & Shandarin 1983; Davis et al. 1985). Section 5 explores the clustering relationships for the various web types which are classified using the Lagrangian based classification scheme. Halo properties such as sphericity, triaxality, fractional anisotropy and spin have been shown to vary with web type (e.g. Hahn et al. 2007b,a; Aragón-Calvo et al. 2010b; Libeskind et al. 2012b). The goal of Section 6 is to examine said properties under a Lagrangian classification scheme that incorporates the properties of the local environment. This section sets the foundation for an outlook into future work. Concluding remarks are offered in Section 7.

2. Background

"And thus Nature will be very conformable to her self and very simple, performing all the great Motions of the heavenly Bodies by the Attraction of Gravity which intercedes those Bodies, and almost all the small ones of their Particles by some other attractive and repelling Powers which intercede the Particles."

Sir Iaasc Newton

2.1. N-body Simulations

The N-body problem was first discussed by Isaac Newton and it attempts to predict the orbital motions of N celestial objects under forces of mutual gravitation. While the case for N=2 was completely solved by Johann Bernoulli, for N $\geq$3 we have a dynamical system with no analytical solutions and hence problems of this nature must be studied numerically (Aarseth 2003).

For cosmological simulations, where the large scale density field is modelled with $N \leq 10^{11}$ particles, the force per unit mass for the i^{th} particle is given by (Aarseth 2003) as:

$$\ddot{\mathbf{r}}_i = -G \sum_{j=1;j\neq i}^{N} \frac{m_j(\mathbf{r}_i - \mathbf{r}_j)}{|\mathbf{r}_i - \mathbf{r}_j|^3} \ , \tag{3}$$

where m_j is the mass of the j^{th} particle and $\mathbf{r}_i$, $\mathbf{r}_j$ are the coordinates of the i^{th} and j^{th} particle respectively. Calculating Eq. 3 using the direct summation can prove to be computationally intensive for billions of particles. Various codes now exist that use different methodologies to solve the N-body problem. These include the Particle Mesh (PM) code (Hockney & Eastwood 1981); which interpolates the particles onto a 3D mesh. The density and velocity of each mesh cell is then evaluated using a clouds in cells (CIC) assignment. This method is extremely efficient, with a computational complexity of $\mathcal{O}(N_g \log N_g)$, where N_g is the number of grid points, however the resolution is limited by the grid size (Klypin 2000). The particle mesh assignment is easily implemented in Fourier space where derivatives are trivial to calculate using a finite difference scheme, while also inducing automatic periodic boundary conditions (Bertschinger & Gelb 1991) (see Sec. 2.1.1).

The CIC scheme interpolates the mass density between mesh cells by uniformly distributing the particle mass within a cubical cloud. When the particles move, the mass of the cell is then distributed among its neighbours according to how much overlap exists between the current cell and its surrounding 8 mesh cells (Hockney & Eastwood 1981).

P^3M or PPPM (Hockney & Eastwood 1981; Efstathiou et al. 1985) uses a PM code for long range forces and a Particle-Particle algorithm for small scale forces. This improves the resolution when compared to an ordinary PM code however the direct sum calculation for the Particle-Particle interactions become computationally expensive at small redshifts where the collapse of structure is prominent Bertschinger & Gelb (1991).

Another common solution for gravitational N-body evolution is the hierarchical Barnes-Hut Tree Algorithm (Appel 1985; Barnes & Hut 1986). The tree algorithm calculates the nearest neighbours by dividing the simulation space into eight child cubes by planes parallel to the 3 axes passing through the middle of the cube, yielding an 'octree'. The child cubes are recursively subdivided until a predefined distance d is reached. The algorithm then groups neighbouring particles into increasingly larger cells so that the gravitational potential is accounted for using a hierarchical multipole expansion, 'walking up the tree', reducing the computation from $\mathcal{O}(N)$ interactions to just $\mathcal{O}(\log N)$ interactions per particle (Barnes & Hut 1986; Bertschinger 1998; Springel 2005).

The Adaptive Refinement Tree (ART) code, given by Kravtsov et al. (1997), has also been a staple mainstream cosmological N-body algorithm as it has a high force resolution and is extremely fast, i.e. CPU time scales with the number of cells - $\mathcal{O}(N_c)$ Kravtsov et al. (1997); Bertschinger (1998). The algorithm begins by using a PM assignment (whose cells do not necessarily have to be square) and recursively creates a finer mesh refined on the highest density regions creating a sequence of meshes that have a resolution hierarchy covering the densest areas of the simulation. Each cell in the ART mesh is evaluated in a recursive manner and a decision to refine or de-refine the cell is made based on some density threshold. In each iteration, the density fields are then evaluated using a CIC algorithm (Kravtsov et al. 1997).

Current ΛCDM theory suggests that dark matter constitutes $\approx 85\%$ of the gravitating mass in the universe (Peter 2012), thus understanding the kinematics of DM alone (neglecting baryonic matter) will give one insight into structure formation and the galaxy environment. DM is said to be cold, dark and collisionless due to the fact that it only interacts gravitationally (not interacting electromagnetically) and moves at non-relativistic speeds (Springel et al. 2005a). One may represent DM particles in a cosmological simulation by sampling the phase space through the evolution in time at regular intervals. DM particles evolve according to Newtons laws given in comoving coordinates by Peebles (1980) in Eq. 4.

$$
\begin{aligned}
\dot{\mathbf{x}} &= \frac{1}{a}\mathbf{v} \\
\ddot{\mathbf{x}} + 2H\dot{\mathbf{x}} &= -\frac{1}{a^2}\nabla\phi \\
\nabla^2\phi &= 4\pi G a^2[\rho(\mathbf{x},t) - \bar{\rho}(t)] = \frac{3}{2}\Omega_0 H^2 \frac{\delta\rho}{\rho}
\end{aligned}
\tag{4}
$$

where $\mathbf{x}$ and $\mathbf{v}$ are the position and peculiar velocity of the particle respectively, $a = (1+z)^{-1}$ is the cosmic expansion factor and $H = \dot{a}/a$ is the Hubble factor. ρ and $\bar{\rho}$ are the density and mean spatial cosmic density respectively and ϕ is the gravitational potential.

$\Omega_0 = 8\pi G\bar{\rho}/3H^2$ is the cosmological density parameter and determines the geometry of space. $\Omega_0 < 1$ implies a negatively curved open Universe or hyperbolic shape whose eventual fate will expand forever while $\Omega_0 > 1$ implies a closed or spherical shaped Universe that will eventually collapse. $\Omega_0 \simeq 1$ implies a Euclidean Universe that will continually expand at a decelerating rate (Bertschinger & Gelb 1991).

The simulations begin with setting up the initial conditions by specifying the initial density power spectrum P(k), assigning a random density field to a cubic mesh (Bertschinger & Gelb 1991). P(k) statistically describes the Gaussian random field with small amplitude fluctuations mimicking the distribution of the early Universe (Bertschinger & Gelb 1991). The positions and velocities of the DM phase space elements can then be obtained from the density fluctuations using the Zeldovich approximation (Zel'dovich 1970). Given a homogeneous and collisionless matter distribution, the Zeldovich approximation states that the Eulerian coordinates of particles can be described at time t as:

$$
\begin{aligned}
\mathbf{r}(\mathbf{q},t) &= a(t)\,(\mathbf{q} + \mathbf{s}(\mathbf{q},t)) \\
&\approx a(t)[\mathbf{q} + b(t)\mathbf{s}_0(q)]
\end{aligned}
\tag{5}
$$

where $\mathbf{q}$ are the Lagrangian coordinates, a(t) is again the Hubble expansion factor, b(t) is the growing rate of linear fluctuations and $\mathbf{s}(q)$ is the particle displacement with respect to the the Lagrangian initial conditions. If $\phi_0(q)$ is the potential originating from the initial linear fluctuations then we have that the displacement is related to $\phi_0(q)$ by:

$$
\mathbf{s}_0(q) = \nabla\phi_0(q) \tag{6}
$$

For a flat universe $b(t) \propto a(t) \propto t^{2/3}$ and the displacement field $\mathbf{s}(q)$ is related to the density perturbation field by

$$
\frac{\delta\rho}{\rho} = -\nabla\cdot\ \mathbf{s} \qquad \nabla\times\mathbf{s} = 0 \tag{7}
$$

The vorticity of the displacement field is zero as it is thought any primordial rotation vanishes as the Universe undergoes expansion, meanwhile gravitational collapse at later times is responsible for a divergent field (Bertschinger & Gelb 1991). Typically the linear displacement equation (Eq. 7) is computed in Fourier space using a Fast Fourier Transform (FFT) and the particle positions and velocities are perturbed using Eq. 5.

The phase space is then allowed to evolve under self gravitation. To describe the phase space density distribution for the DM clustered component, one combines the collisionless Boltzmann equation, known as the Vlasov equation, with the Poisson equation to numerically yield the matter density in six dimensional phase space. The density distribution function is described by the function $f_i(\mathbf{x}, \dot{\mathbf{x}}, t)$ and the Vlasov Poisson equations are a 6N system of first order differential equations given by Klypin (2000) as:

$$\begin{aligned} 0 &= \frac{\partial f_i}{\partial t} + \dot{\mathbf{x}}\frac{\partial f_i}{\partial \mathbf{x}} - \nabla\phi\frac{\partial f_i}{\partial \mathbf{p}} \\ \nabla^2\phi &= 4\pi G a^2(\rho(\mathbf{x},t) - \langle\rho_{DM}(t)\rangle)) = 4\pi G a^2 \Omega_{DM}\delta_{DM}\rho_{cr,0} \\ \delta_{DM}(\mathbf{x},t) &= (\rho_{DM} - \langle\rho_{DM}\rangle)/\langle\rho_{DM}\rangle \\ \rho_{DM}(\mathbf{x},t) &= a^{-3}\sum_i m_i \int d^3\mathbf{p} f_i(\mathbf{x},\dot{\mathbf{x}},t) \end{aligned} \tag{8}$$

where the momentum is given by $\mathbf{p} = a^2\dot{\mathbf{x}}$. Ω_{DM} is the density of the dark matter within the universe and $\rho_{cr,0}$ denotes the critical density at z=0.

2.1.1. Periodic Boundary Conditions

Cosmological simulations are somewhat different from ordinary N-body simulations in that they need to account for an infinite Universe. Since simulating an infinite Universe is impossible, periodic boundary conditions (PBC) are used to achieve a smooth gravitational potential as well as to obtain the isotropic nature of the universe within a cube (Bertschinger & Gelb 1991; Sousbie 2011).

As a result of PBCs, there are no interactions between particles that are separated by more than half the length of the box one is simulating in. This is accomplished by first considering the distance between two particles $x_{ji} = x_j - x_i$ and testing for if $|x_{ji}| > 0.5L_{cube}$. If it is the case that the interaction is occurring over more than half the length of the box then one applies the following algorithm:

$$\begin{aligned} \text{if } x_{ji} > 0.5L_{cube} &\quad \rightarrow x_{ji} = x_j - x_i - L_{box} \\ \text{else if } x_{ji} < -0.5L_{cube} &\quad \rightarrow x_{ji} = x_j - x_i + L_{box} \end{aligned} \tag{9}$$

Fig 3 shows a simple 1D example of periodic boundary conditions. If the length of the cell is given as 5Mpc, one observes the distance between the two particles is larger than half the length of the box ($3.7 > 2.5$ to be exact). Applying Eq. 9, $|x_{ji}|$ is now modified to a value of 1.3, which gives $x_i = -0.3 = x_j - x_{ji,2}$ a position outside the cell. This is not a problem as one is attempting to simulate an infinite Universe and PBCs have the effect of replicating the cells in all directions to artificially construct an infinite Universe (Bagla & Padmanabhan 1997). Neglecting PBCs will, in effect, lead to all the matter collapsing inwards, exaggerating the growth rate of perturbations (Bagla & Padmanabhan 1997).

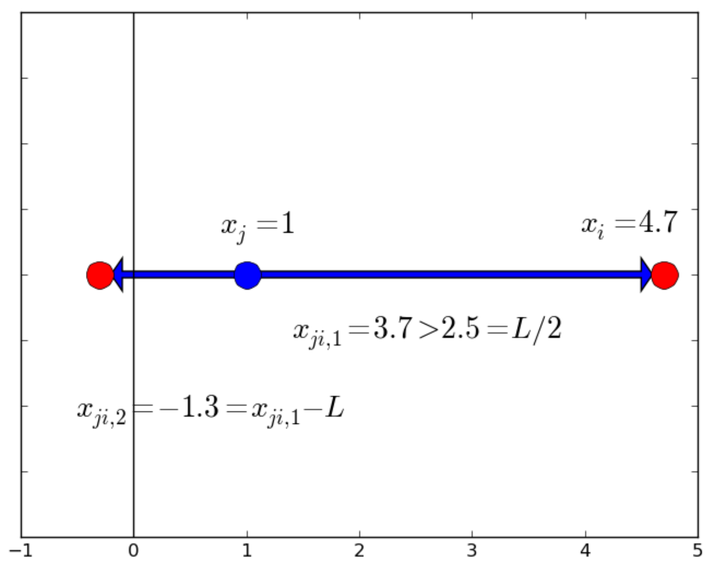

Fig. 3.— An example of periodic boundary conditions in the 1D case. The distance between particles is too great, one applies the PBC algorithm to find a new distance $|x_{ji,2}|$, effectively moving x_i to a new cell attached the left of the old cell. Done for many particles in 3 dimensions, this artificially constructs cells around cells simulating an infinite Universe.

2.2. GADGET-2 Code

Galaxy and Dark Matter Gas Interact - 2 (GADGET-2) (Springel 2005) is a TreeSPH (Hernquist & Katz 1989) N-body cosmological simulation code used to follow a collisionless fluid undergoing gravitational evolution, combined with a SPH method to follow an ideal gas (Springel 2005).

GADGET-2, computes the forces between particles using a hybrid algorithm combining the Particle Mesh (PM) method for long range forces, with a Tree algorithm for short range forces resulting in an aptly named TreePM method (Xu 1995). A synthesis of the PM and Tree algorithm improves the spatial resolution in the short range forces while using the faster PM scheme for the long range forces (Springel 2005). The details of the Tree and PM schemes can be found in Sec. 2.1.

In order to integrate Eq. 8 with respect to time, GADGET-2 employs a second order symplectic leapfrog integration, preserving the energy of the system. The integration equations that update the particle positions and velocities are given by Eq. 10 & 11 respectively.

$$x_{i+1} = x_i + \Delta t v_{(i+1)/2} \tag{10}$$

$$v_{i+3/2} = v_{i+1/2} + \Delta t F(x_{i+1}) \tag{11}$$

$F(x)$ is given as the acceleration parameter dv/dt. These equations may be incremented in time provided one knows x_0 and $v_{1/2}$. When deciding on a time-step Δt, GADGET-2 uses two different time-steps; one for the long range force and one for the short range force as in the TreePM method. The PM integration uses a much larger time-step as the time evolution for this force is comparatively small while the short range forces require much smaller time-steps as this force varies significantly on shorter time scales (Springel 2005). The leapfrog integration is not symplectic when using two different time-steps however Springel (2005) argues that collectively computing the force in this manner produces accuracy levels comparable with symplectic integration (i.e. phase space conserving).

Fig. 4 shows a sample GADGET-2 simulation using a 64Mpc length box and 256^3 particles beginning when the Universe was $\sim$ 36 million years old. The cosmology uses Planck 2013 parameters. A 1 Mpc/h slice of the simulation volume has been taken along the z axis, projected onto the x-y plane. At z=60, one is able to clearly observe the DM particles are homogeneously distributed upon a mesh with faint seeds of structure. The evolution is subdued from $z = 60 \rightarrow 20$ as particles are still largely separated by their initial mesh positions. The gravitational forces ($\propto 1/d^2$) are still very weak between particles due to the large separations and very few particles are collapsing into structures.

Between z=20 and z=7 there exists a high degree of large scale structure formation. At z=7, the collapse of particles into the filamentary web like structures are seen by the the darkest regions forming the ‘skeleton’ of the Universe. Indeed, these structures only get darker and denser as the simulation progresses. Zeldovich pancaking (Zel’dovich 1970) is evident through the evolution of the middle of panel of Fig. 4. Planar sheets are forming and flowing into long thread-like structures known as filaments. The gravitational collapse leaves behind growing underdense regions known as voids.

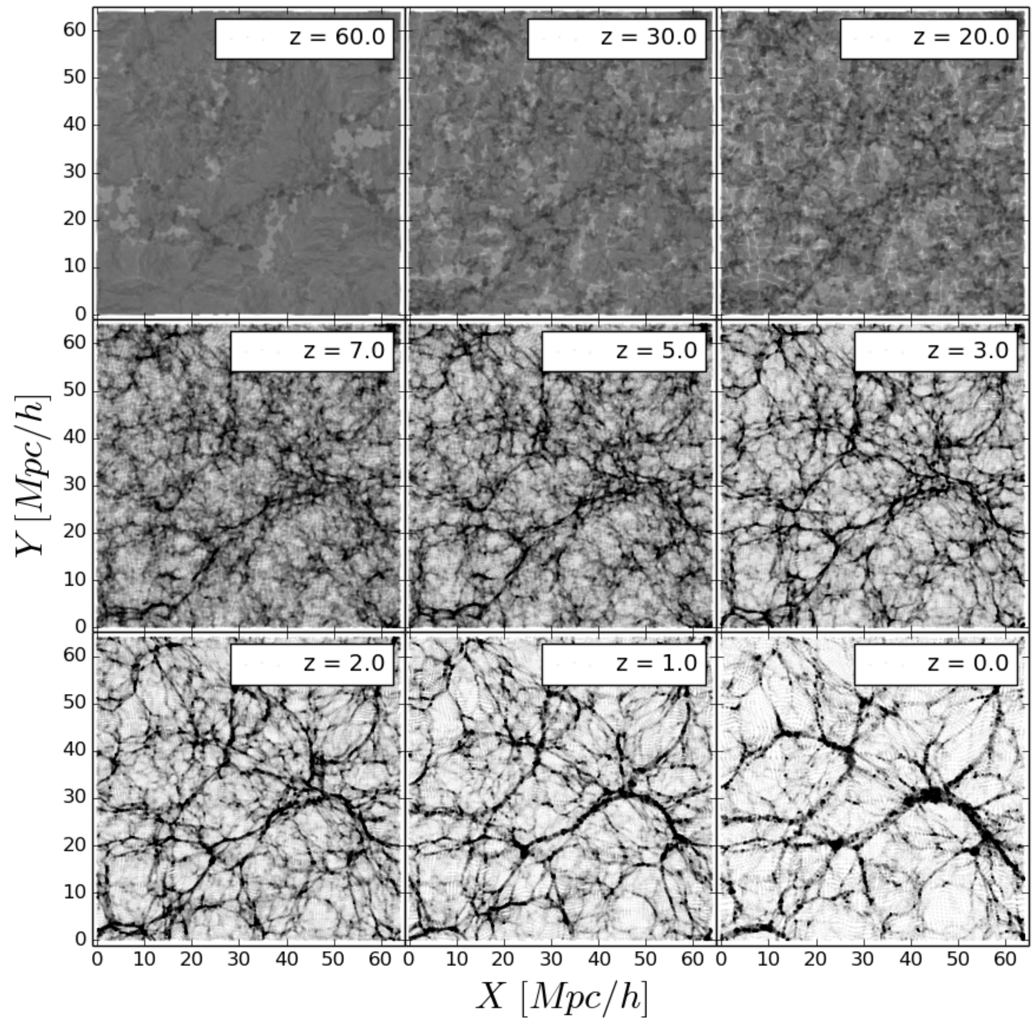

Fig. 4.— A 1 Mpc/h slice from a Gadget-2 simulation using a cube length of 64Mpc, 256^3 particles and Planck 2013 cosmological parameters. The legend indicates the time (redshift) of the simulation. At early times (large redshifts), one is able to see a relatively homogeneous distribution of DM particles. As time progresses, one is able to observe clustering and structure formation take place.

Voids become increasingly apparent at z=2 and grow larger moving left to right in the bottom panel of Fig 4. Many filaments begin to intersect at z=2, coalescing to form node structures. These nodes become extremely detailed by z=0 with small dense clumps of DM embedded in the filament intersections. A full compliment of increasingly dense substructure collectively known as voids, sheets, filaments and nodes may be seen at z=0.

2.3. Galaxy Halo Identification

The DM particles used in simulations constitute the building blocks for DM halos, which are thought to contain galaxies. The goal of a halo finder is to identify halos within the dense clumps of DM particles that have undergone gravitational collapse. The identification of halos is no trivial task and rely on more than just the overdensity within a given region.

Detecting gravitationally bound objects in the phase space may be done using a variety of methods however halo finders generally take on two distinct methodologies namely; (i) the Spherical Overdensity (SO) method (Press & Schechter 1974) also known as density peak locators and (ii) the Friends of Friends (FOF) algorithm (Davis et al. 1985) or particle collectors (Knebe et al. 2011).

Density peak locators construct a sphere around each particle - the radius of which is determined by how big the sphere needs to be to include a number particles that satisfy some predefined density limit (Knebe et al. 2011).

Particle collector codes rely on connecting and linking particles, either in 3D Eulerian coordinates or 6D phase space by constructing a sphere around each particle of size bd/2, where b is known as the linking parameter and is equal to 0.2 by convention. d is known as the mean distance between particles e.g if a simulation has a cube length given by 500Mpc and 256^3 particles, then b = 500/256 Mpc $\sim$ 1.95 Mpc. The particles within each sphere of radius bd/2 are collected and the halo is identified by linking particles within spheres that overlap.

Fig 5 shows a 2D example of the FOF algorithm. Beginning with the particle at the centre of the red circle, one construct a circle with hypothetical radius bd/2 = 0.5Mpc. All the particles within the red circle are then linked, becoming friends. The same is done for the blue circle. Notice that the blue circle and the red circle overlap so that there exists particles that belong in both friend groups. This allows one to link the particles between groups, creating friends of friends particles, and defines the basic groups and subgroups for halo identification.

2.3.1. Rockstar Halo Finder

The halo identifier used in this project is the Rockstar halo finder. This algorithm and its details below are taken from Behroozi et al. (2013). Rockstar halo finder relies on the FOF algorithm to initially separate the groups of particles, before normalising the particle positions and velocities according to their group properties. This helps define a phase space

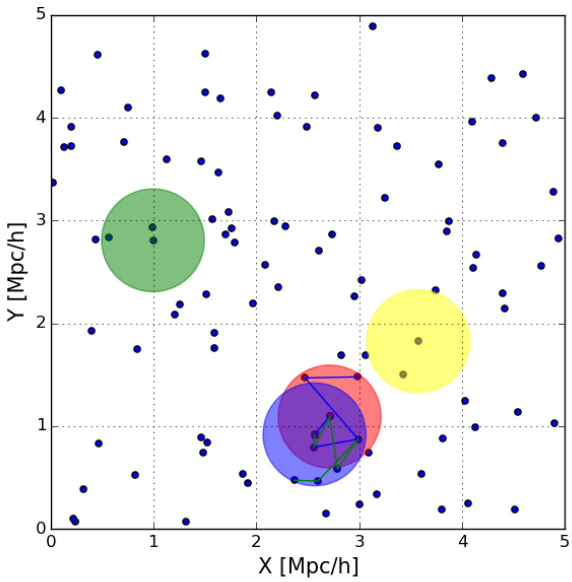

Fig. 5.— A 2D example of the FOF algorithm with a radius of 0.5Mpc. The overlapping blue and red circles indicate particles that have been linked together within their respective groups (the friends) as well as with the particles in the overlapping circle (the friends of friends).

metric $d(p_1, p_2)$ between two particles p_1 and p_2, given by Gottloeber et al. (1998) in equation 12.

$$d(p_1, p_2) = \left(\frac{|\mathbf{x}_1 - \mathbf{x}_2|^2}{\sigma_x^2} + \frac{|\mathbf{v}_1 - \mathbf{v}_2|^2}{\sigma_v^2} \right)^{1/2} \tag{12}$$

where σ_x and σ_v are the particle position and velocity dispersions with respect to their FOF groups respectively. The algorithm progresses by partitioning the FOF groups into sub-groups using a variable phase space linking length to ensure 70% of the groups particles are assigned a sub-group.

To find further substructure, the process outlined above is repeated so that for each sub-group one renormalises the particle positions and velocities and identifies sub-sub-groups using a new linking length, moving to a lower level of substructure.

Seed' halos are assigned to the lowest levels of substructure and particles are assigned to their nearest seed halo based on the shortest distance in the phase space. Unbound particles are removed and the halo finder calculates halo properties.

Fig. 6 shows the same GADGET-2 simulation slices as in Fig. 4, however now the halos identified by the ROCKSTAR halo finder are over-plotted in red. Immediately one observes

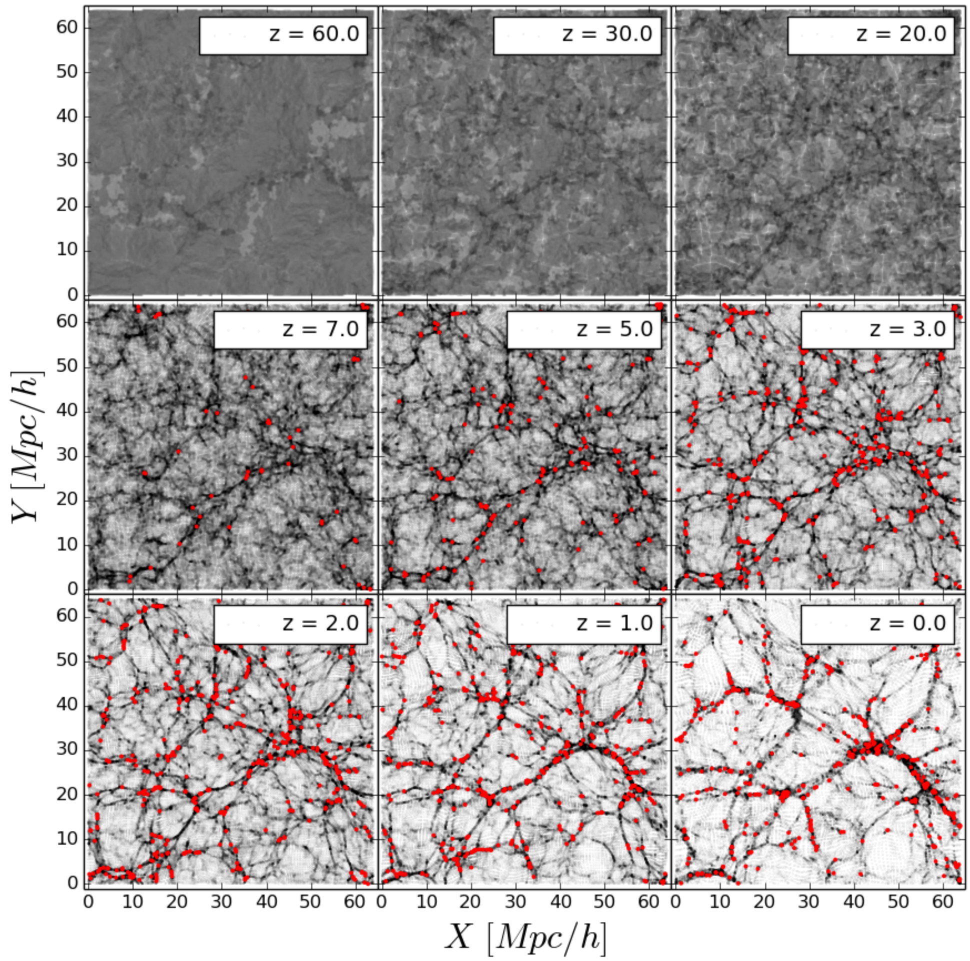

Fig. 6.— The same slices of the simulation cube as in Fig. 4 over-plotted with the halos (in red) identified using the ROCKSTAR (Behroozi et al. 2013) halo finder. The halos clearly trace the densest regions of the cosmic web

that halos trace the densest regions of the cosmic web. The number of halos increase as redshift decreases (i.e. as substructure forms). A few, small, sparsely distributed halos can be seen at a redshift of ~ 7. Moving to a redshift of 0, the halos increase in number and size, extending through the elongated filaments and clumping in the node regions where substructure is fully developed.

3. Smoothed Particle Hydrodynamics

> "My goal is simple. It is a complete understanding of the universe, why it is as it is and why it exists at all."
>
> Stephen Hawking

Examining the methods set out in Sec. 2.1 one observes that all methods use some variation of an Eulerian mesh to define the density and velocity fields. Conversely, smoothed particle hydrodynamics (SPH) is a Lagrangian mesh-free particle method, pioneered by Lucy (1977), Gingold, R. A. and Monaghan (1977), to analyse fluid flows. In the SPH approach, one follows the set of particles representing the state of the system while under the laws of hydrodynamics.

Since its inception, this technique has been used to study a wide range of astrophysical problems such as the collision of binary stars (Benz 1988), supernova (Hultman & Pharasyn 1999), galaxy formation and evolution (Monaghan & Lattanzio 1991) as well as the coalescing of black hole-neutron star binaries (Kluźniak & Lee 1998).

Eulerian meshes are fixed in space and transfer physical properties (e.g. mass, energy, momentum) through the cell boundary (Liu & Liu 2003). The SPH approach is Lagrangian in nature as it follows individual particles. The SPH method has good conservation properties, is Galilean invariant and does not possess any advection errors (Springel 2010). Unlike mesh based methods, the resolution in the SPH approach is adaptive when using a constant neighbour number. Regions of significant gravitational collapse have many particles located in a small region with plenty of neighbour numbers. This ensures a small smoothing length. In contrast, underdense regions will require large smoothing lengths to obtain the required neighbour number. This ensures the resolution follows the mass of the simulation (Liu & Liu 2003).

3.1. SPH Formulation

The following definitions and formulation are based on the ideas found in Lucy (1977); Gingold, R. A. and Monaghan (1977); Monaghan (1985). The basis for the mathematical definition of the SPH method, relies on the integral representation of a function $f = f(\mathbf{x})$

defined using the following identity:

$$f(\mathbf{x}) = \int\limits_{\Omega} f(\mathbf{x}')\delta(\mathbf{x}-\mathbf{x}')d\mathbf{x}' \tag{13}$$

where Ω is the integrable volume surrounding a 3 dimensional position vector $\mathbf{x}$ and $\delta(\mathbf{x}-\mathbf{x}')$ is the Dirac delta function defined as:

$$\delta(\mathbf{x}-\mathbf{x}') = \begin{cases} 1 & \mathbf{x} = \mathbf{x}' \\ 0 & \mathbf{x} \neq \mathbf{x}' \end{cases} \tag{14}$$

Replacing the Dirac delta function with a smoothing kernel function $W(\mathbf{x}-\mathbf{x}', h)$, where h is given as the smoothing length, yields the definition of the smoothed function $< f(\mathbf{x}) >$ in Eq. 15

$$< f(\mathbf{x}) >= \int\limits_{\Omega} f(\mathbf{x}')W(\mathbf{x}-\mathbf{x}', h)d\mathbf{x}' \tag{15}$$

One is able to show that the SPH method is second order accurate by Taylor expanding $f(\mathbf{x}')$ about the point $\mathbf{x}$ shown in Eq. 16 (Benz 1990; Monaghan 1992)

$$< f(\mathbf{x}) > \; = \int\limits_{\Omega} \left[f(\mathbf{x}) + f'(\mathbf{x})(\mathbf{x}'-\mathbf{x}) + \mathcal{O}((\mathbf{x}'-\mathbf{x})^2) \right] W(\mathbf{x}-\mathbf{x}', h)d\mathbf{x}' \tag{16}$$

$$= f(\mathbf{x}) \int\limits_{\Omega} W(\mathbf{x}-\mathbf{x}', h)d\mathbf{x}' + f'(\mathbf{x}) \int\limits_{\Omega} (\mathbf{x}'-\mathbf{x})W(\mathbf{x}-\mathbf{x}', h)d\mathbf{x}' + \mathcal{O}(h^2) \tag{17}$$

W is typically taken as an even function (Liu & Liu 2003) with respect to $\mathbf{x}$, so that $(\mathbf{x}'-\mathbf{x})W(\mathbf{x}-\mathbf{x}', h)$ is an odd function and thus the integral over the odd function is zero. Exploiting a kernel property, known as the *unity condition* , $\int_{\Omega} W(\mathbf{x}-\mathbf{x}', h)d\mathbf{x}' = 1$, one obtains the following result:

$$< f(\mathbf{x}) >= f(\mathbf{x}) + \mathcal{O}(h^2) \tag{18}$$

Eq. 15 defines an averaged field over the support function W and it is then assumed $< f(\mathbf{x}) >\approx f(\mathbf{x})$. The particle representation of the SPH method is found by discretising Eq. 15 (i.e. the integral becomes a sum over N particles in the volume of the kernel). This takes the form:

$$< f(\mathbf{x}) >= \sum_{j=1}^{N} f(\mathbf{x}'_j)W(\mathbf{x}-\mathbf{x}'_j, h)\Delta V_j \tag{19}$$

where $\Delta V_j = m_j/\rho_j$ is the finite volume of the particle defined as the ratio of the mass and density of the j^{th} particle. Assuming particle i is located at $\mathbf{x}$ and particle j is located at $\mathbf{x}'$,

$r_{ij} = |\mathbf{x}_i - \mathbf{x}_j|$, then we may define some particle properties such as the smoothed particle density and velocity in Eq. 20 and Eq. 21 respectively.

$$< \rho_i > \;=\; \sum_{j=1}^{N} \rho_j W(r_{ij}, h) \frac{m_j}{\rho_j} = \sum_{j=1}^{N} m_j W(r_{ij}, h) \tag{20}$$

$$< \mathbf{v}_i > \;=\; \sum_{j=1}^{N} \frac{m_j}{\rho_j} \mathbf{v}_j W(r_{ij}, h) \tag{21}$$

Finally, a note on the spatial derivatives of SPH defined quantities. Taking the gradient of Eq. 15 with respect to the i^{th} particle, one observes that the derivative of the function results in the derivative just being applied to the kernel (i.e. considering the derivative with respect to $\mathbf{x}$, the j^{th} particle is a function of $\mathbf{x}'$ and only the kernel is a function $\mathbf{x}$), as seen in Eq. 22 (Price 2012). This is very useful as the derivative of the kernel can be calculated analytically and no numerical differentiation is required.

$$< \nabla f(\mathbf{x}) > \;=\; \frac{\partial}{\partial \mathbf{x}} \int_{\Omega} f(\mathbf{x}') W(\mathbf{x} - \mathbf{x}', h) d\mathbf{x}' + \mathcal{O}(h^2) \tag{22}$$

$$= \sum_{j=1}^{N} \frac{m_j}{\rho_j} f_j \nabla W(r_{ij}, h) \tag{23}$$

3.2. Kernel Interpolants

Smoothing kernels are chosen with a few important properties in mind. As mentioned above, one defines the kernel so that the integral over the domain is one. Eq. 15 demands that

$$\lim_{h \to 0} W(\mathbf{x} - \mathbf{x}', h) = \delta(\mathbf{x} - \mathbf{x}')$$

This is known as the *Delta function property* (Liu & Liu 2003). The final condition a kernel interpolant must satisfy is the *compact condition* which states $W(\mathbf{x} - \mathbf{x}', h) = 0$ when $|\mathbf{x} - \mathbf{x}'| > \kappa h$ for some constant κ related to the kernel definition. κh is known as the support domain for the smoothing kernel (Liu & Liu 2003).

Fig. 7 shows the support domain of the kernel defined by κh and the kernel interpolant W is shown by the green Gaussian shaped curve. The particle in question sits at $\mathbf{x}_i$ and one compares the distance between the given particle and all its neighbours within the support domain. The contribution of the neighbouring particles to $f(\mathbf{x}_i)$ is then weighted by the smoothing kernel.

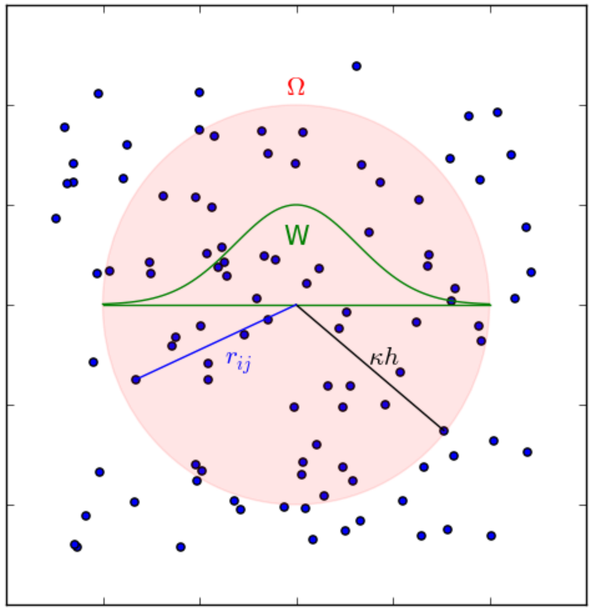

Fig. 7.— The SPH kernel support domain, adapted from Liu & Liu (2003). All particles within κh are weighted by W according to the distance r_{ij} between $\mathbf{x}_i$ and $\mathbf{x}_j$.

Smoothing kernels should satisfy 3 main properties to offer accurate approximations for smoothed fields, these are given as (Price 2012):

i Kernels should be monotonically decreasing as r_{ij} increases and the weighting should be positive

ii Kernels should be symmetric (i.e. $W(\mathbf{x}-\mathbf{x}', h) = W(\mathbf{x}'-\mathbf{x}, h) = W(|\mathbf{x}-\mathbf{x}'|, h)$)

iii Kernels should posses a flatter central region so as to reduce the impact of small changes in positions of near neighbours

A Gaussian kernel may seem a natural choice, however this kernel has a radius that extends out infinitely thus one needs to account for all the particles in the box. Better is to choose a similar Gaussian shape that, at a finite radius, is truncated to zero. Popular kernels include the B-spline functions (M_n) (Monaghan & Lattanzio 1985; Monaghan 1985), where n is the order of the kernel. Higher order kernels result in better Gaussian approximations. Letting

$q = r_{ij}/h$, $W(r_{ij}, h) = w(q)$ the M_4 cubic B-spline is given as:

$$w(q) = \frac{\sigma}{h^d} \begin{cases} \frac{1}{4}(2-q)^3 - (1-q)^3 & 0 \leq q < 1 \\ \frac{1}{4}(2-q)^3 & 1 \leq q < 2 \\ 0 & q \geq 2 \end{cases} \tag{24}$$

where $\sigma = [2/3, 10/7\pi, 1/\pi]$ for dimensions $d = 1, 2, 3$ respectively. The M_5 quartic kernel is defined by (Morris 1996) as:

$$w(q) = \frac{\sigma}{h^d} \begin{cases} (\frac{5}{2}-q)^4 - 5(\frac{3}{2}-q)^4 + 10(\frac{1}{2}-q)^4 & 0 \leq q < 1/2 \\ (\frac{5}{2}-q)^4 - 5(\frac{3}{2}-q)^4 & 1/2 \leq q < 3/2 \\ (\frac{5}{2}-q)^4 & 3/2 \leq q < 5/2 \\ 0 & q \geq 5/2 \end{cases} \tag{25}$$

where the normalisation factor $\sigma = [1/24, 96/1199\pi, 1/20\pi]$. The final kernel this research report will look at it the M_6 quintic (Eq. 26) with normalisation factors $\sigma = [1/120, 7/478\pi, 1/120\pi]$(Morris 1996). Again this kernel is progressively more representative of a Gaussian compared to the cubic and quartic kernels respectively.

$$w(q) = \frac{\sigma}{h^d} \begin{cases} (3-q)^5 - 6(2-q)^5 + 15(1-q)^5 & 0 \leq q < 1 \\ (3-q)^5 - 6(2-q)^5 & 1 \leq q < 2 \\ (3-q)^5 & 2 \leq q < 3 \\ 0 & q \geq 3 \end{cases} \tag{26}$$

The B-spline kernels mentioned above can be seen in the top panel of Fig. 8. Observe the effect of increasing the order: the kernels' peaks fall and the tails become fatter, extending out further, more representative of a Gaussian kernel. Derivatives of the kernels are shown in the bottom panel of Fig. 8. The derivatives of the respective kernels are not symmetric about q=0. Applying gradients to smoothed quantities as in Eq. 22 may result in a negative contribution to the gradient of the smoothed field, from the derivative of the kernel weighting. Increasing the order has the same effect as in the top panels. Peaks and troughs become flatter and the curves tend to zero at a slower rate.

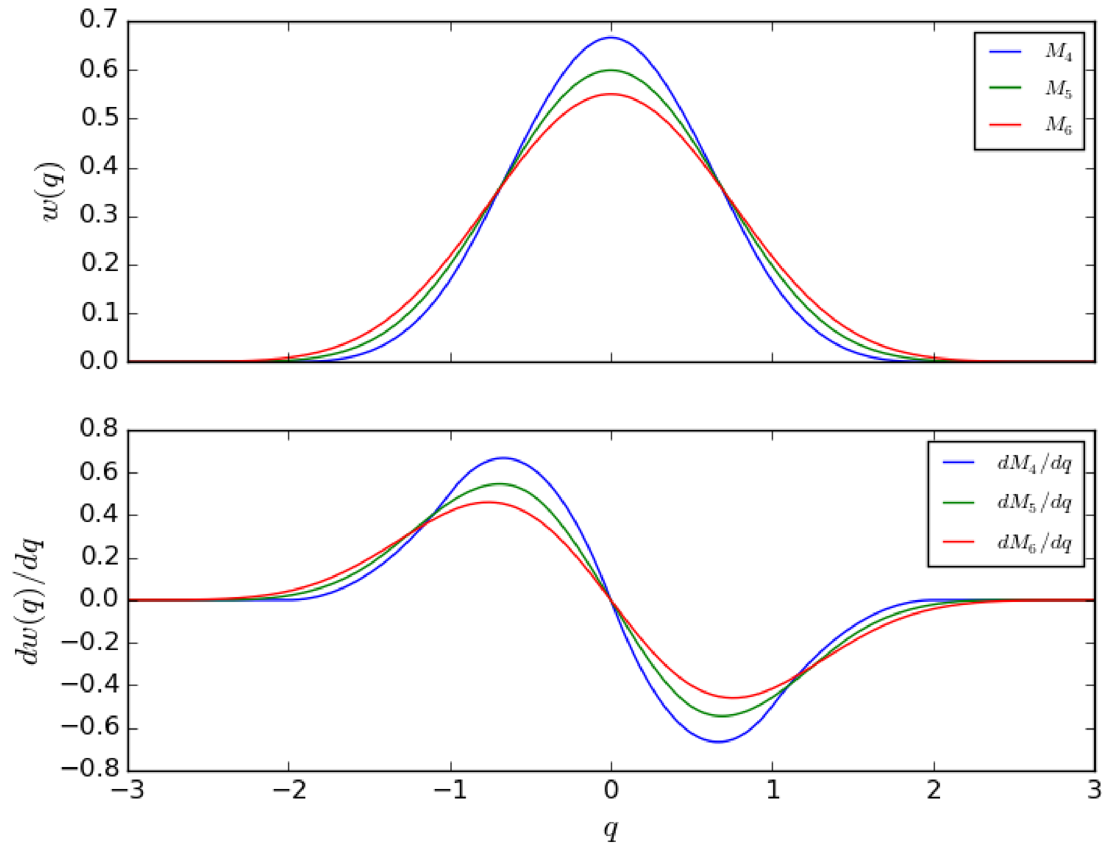

Fig. 8.— The cubic (M_4), quartic (M_5) and quintic (M_6) B-spline kernels as well as their derivatives.

4. Lagrangian Classification Scheme

> "Nature uses only the longest threads to weave her patterns, so that each small piece of her fabric reveals the organization of the entire tapestry."
>
> Richard Feynman

In this chapter, the Eulerian 'V-web' classification scheme is developed on a state of the art GADGET-2 Springel (2005) simulation. The results are shown to be consistent with those found in Hoffman et al. (2012). The SPH velocity shear tensor is then defined and the Lagrangian classification scheme is employed on the same simulation, first on dark matter particles and subsequently on dark matter halos. Finally a comparison is drawn between the two classification methods. The full development of this chapter is presented in the paper published in Fisher et al. (2016).

4.1. Velocity Shear Tensor Background

Initial attempts to classify the the cosmic web, given by Hahn et al. (2007b); Aragón-Calvo et al. (2007b); Forero-Romero et al. (2009), used Tidal Torque Theory to calculate the Hessian of the density field to obtain the tidal tensor. Classification of the cosmic web is done by counting the number of positive eigenvalues of the tidal tensor greater than zero. This has come to be known as the T-web approach. Later, Hoffman et al. (2012) showed that the V-web velocity shear tensor is able to improve on the resolution of the T-web, resolving smaller structures, to better study halo properties. The velocity field, when compared to the gravitational field, retains a better memory of the initial conditions of the early Universe and as a result traces the underlying mass distribution better Kitaura et al. (2012).

The deformation a fluid undergoes is a result of velocity gradients. Following the analysis by Libeskind et al. (2014), one may Taylor expand the peculiar velocity field $\mathbf{v}(\mathbf{r})$ about the point $\mathbf{r}_0$ to first order obtaining Eq 27.

$$\mathbf{v}_\alpha(\mathbf{r}) = \mathbf{v}_\alpha(\mathbf{r}_0) + \left[\frac{\partial v_\alpha}{\partial r_\beta}\right]_{\mathbf{r}_0} d\mathbf{r}_\beta \tag{27}$$

where $d\mathbf{r} = \mathbf{r} - \mathbf{r}_0$ and $\alpha, \beta = x, y, z$. $\partial v_\alpha / \partial r_\beta$ is known as the rate of deformation tensor and represents velocity gradients. The deformation tensor can be further decomposed into its shear rate (symmetric) and vorticity (anti-symmetric) components respectively, show in

Eq 28.

$$\frac{\partial v_\alpha}{\partial r_\beta} = \frac{1}{2}\left(\frac{\partial v_\alpha}{\partial r_\beta} + \frac{\partial v_\beta}{\partial r_\alpha}\right) + \frac{1}{2}\left(\frac{\partial v_\alpha}{\partial r_\beta} - \frac{\partial v_\beta}{\partial r_\alpha}\right) \tag{28}$$

Hoffman et al. (2012) defines the symmetric component of the deformation tensor, or rate of strain tensor, as the V-web velocity shear tensor, $\Sigma_{\alpha\beta}$, scaled by the Hubble constant as:

$$\Sigma_{\alpha\beta} = -\frac{1}{2H_0}\left(\frac{\partial v_\alpha}{\partial r_\beta} + \frac{\partial v_\beta}{\partial r_\alpha}\right) \tag{29}$$

The velocity shear tensor is scaled by the Hubble constant to make the units dimensionless and may be diagonalised to obtain the eigenvalues λ_i. Defining the shear tensor in Eq 29 with a negative sign and sorting the eigenvalues so that $\lambda_1 \geq \lambda_2 \geq \lambda_3$ allows for a useful interpretation as now the largest eigenvalue of the shear tensor corresponds to the eigenvector with the fastest rate of collapse. This provides an explanation for the formation of nodes, sheets, filaments and voids. Various web types will collapse with varying strengths along a different number of axes. The classification algorithm given by Hoffman et al. (2012) uses the eigenvalues of the shear tensor to examine the collapse or expansion of the fluid at a given point.

4.2. Classification Algorithm

Hoffman et al. (2012)'s algorithm to classify the cosmic web consists of constructing the shear tensor at a given point, finding the eigenvalues, λ_i and for the shear tensor and comparing the eigenvalues to a given threshold value λ^{th} to obtain four cases:

$$\text{Web Type} = \begin{cases} \text{Node} & \lambda_1 \geq \lambda_2 \geq \lambda_3 \geq \lambda^{th} \\ \text{Filament} & \lambda_1 \geq \lambda_2 \geq \lambda^{th} \geq \lambda_3 \\ \text{Sheet} & \lambda_1 \geq \lambda^{th} \geq \lambda_2 \geq \lambda_3 \\ \text{Void} & \lambda^{th} \geq \lambda_1 \geq \lambda_2 \geq \lambda_3 \end{cases}$$

The eigenvectors $\mathbf{e}_i$ define an orthonormal basis preserving the linear and metric properties of $\mathbb{R}^3$. Historically, λ^{th} has been chosen by visual inspection of the cosmic web with a popular value being $\lambda^{th} = 0.44$ (Hoffman et al. 2012; Libeskind et al. 2012b,a) however this value may vary with different simulation parameters. Observe that when all three eigenvalues are greater than λ^{th}, all 3 axes are collapsing yielding a node classification while voids are classified with zero eigenvalues greater than λ^{th} indicative of an expansion along all 3 axes. Filaments exhibit a characteristic collapse along 2 axes with an expansion along the third while sheets collapse along 1 axis and expand along 2 axes.

4.3. Paper Credit

Credit for the work appearing in Fisher et al. (2016) must be assigned as follows. The idea of a new mesh-free method defined in SPH terms was a result of fruitful discussions between Faltenbacher and Fisher, based on previous work. The Eulerian mesh code was developed by Faltenbacher however all subsequent analysis code was done by Fisher.

The basic Lagrangian classification code was developed in tandem with Faltenbacher and Fisher. The computation of the kd-tree was done by M. Johnson. Fisher is responsible for the theoretical development of the SPH velocity shear tensor as well as all analysis code relating to the Lagrangian classification. The research paper was also drafted by Fisher. The paper that follows has been compressed for the online version of the research report due to the file constraints imposed. Should one wish to view the online version, please visit `http://mnras.oxfordjournals.org/cgi/content/full/stw370?ijkey=h2D8qsBAnAIrK1X&keytype=ref`

Monthly Notices of the ROYAL ASTRONOMICAL SOCIETY

MNRAS **458,** 1517–1528 (2016) doi:10.1093/mnras/stw370
Advance Access publication 2016 February 16

Lagrangian methods of cosmic web classification

J. D. Fisher,★ A. Faltenbacher and M. S. T. Johnson
Department of Physics, University of Witwatersrand, Braamfontein 2000, South Africa

Accepted 2016 February 12. Received 2016 February 12; in original form 2015 November 19

ABSTRACT

The cosmic web defines the large-scale distribution of matter we see in the Universe today. Classifying the cosmic web into voids, sheets, filaments and nodes allows one to explore structure formation and the role environmental factors have on halo and galaxy properties. While existing studies of cosmic web classification concentrate on grid-based methods, this work explores a Lagrangian approach where the V-web algorithm proposed by Hoffman et al. is implemented with techniques borrowed from smoothed particle hydrodynamics. The Lagrangian approach allows one to classify individual objects (e.g. particles or haloes) based on properties of their nearest neighbours in an adaptive manner. It can be applied directly to a halo sample which dramatically reduces computational cost and potentially allows an application of this classification scheme to observed galaxy samples. Finally, the Lagrangian nature admits a straightforward inclusion of the Hubble flow negating the necessity of a visually defined threshold value which is commonly employed by grid-based classification methods.

Key words: hydrodynamics – methods: numerical – dark matter – large-scale structure of Universe.

1 INTRODUCTION

The large-scale distribution of matter throughout the Universe is originally described by Bond, Kofman & Pogosyan (1996) as the cosmic web, exhibiting a filamentary structure with regions of increasing density classified as voids, sheets, filaments and nodes. Cosmological numerical simulations are used to explore the large-scale structure and have contributed significantly to the establishment of the ΛCDM model of structure formation. Cold dark matter (DM) is said to constitute ∼85 per cent of the gravitating mass within the Universe, thus understanding the kinematics of DM allows one to probe into the evolution of the Universe in both the linear and non-linear regime. We use pure DM simulations, neglecting the baryonic matter component, to represent the *N*-body problem as a fluid under gravitational evolution using the Vlasov–Poisson equations (Kuhlen, Vogelsberger & Angulo 2012).

Galaxy morphology has been shown to vary with the cosmic environment (Dressler 1980; Blanton et al. 2005; Gao, Springel & White 2005; Faltenbacher 2010) and exploring this link is crucial to the development of a consistent cosmological theory of galaxy formation and evolution. Galaxy redshift surveys and DM *N*-body simulations have shown a significant statistical correlation in filamentary structure with the different web types thought to be a result of small density perturbations in the early universe that have undergone gravitational collapse.

Initial attempts to classify different web types with kinematical information were presented in Aragón-Calvo et al. (2007a), Hahn et al. (2007a) and Forero-Romero et al. (2009) using tidal torque theory, evaluating the Hessian of the gravitational potential. Since then, more sophisticated algorithms have been introduced to describe the topology of the phase space and identify substructure. Aragón-Calvo et al. (2010b) used the SpineWeb framework based on the watershed algorithm (Platen, Van De Weygaert & Jones 2007) to segment the density field.

Falck, Neyrinck & Szalay (2012) showed that one is able to classify morphological structures using the ORIGAMI method: counting the number of orthogonal folds in the Lagrangian phase space sheet. Various methods have borrowed techniques from discrete Morse theory (Colombi, Pogosyan & Souradeep 2000) using the Delaunay Tessellation Field Estimator (Schaap & van de Weygaert 2000) to identify substructure in the cosmological density fields (Aragón-Calvo et al. 2007a, 2010b; Sousbie 2011).

Hoffman et al. (2012) introduced a classification scheme based on the shear of the velocity field (V-web) and showed it is able to improve on the resolution of the tidal tensor-based method (T-web), resolving smaller structures, to better study halo properties. DM simulations are characterized by the density and velocity fields with these two fields being related by equation (1), the familiar mass conservation equation:[1]

$$\frac{1}{\rho}\frac{D\rho}{Dt} = -(\nabla\cdot\boldsymbol{v})\,. \tag{1}$$

★ E-mail: 302186@students.wits.ac.za

[1] $\frac{D\rho}{Dt} = \frac{\partial\rho}{\partial t} + \boldsymbol{v}\cdot\nabla\rho$ is the comoving derivative.

Hoffman et al. (2012) provide evidence of the velocity divergence field tracing the density field; a divergent velocity field being associated with underdense regions. The velocity field can also be used to trace the cosmic web *backwards* throughout time providing one with better insights into the initial conditions of the early universe (Frisch et al. 2002). Bond et al. (1996) showed that the strain field of the fluid is directly related to the filamentary structure of the cosmic web. Thus, the velocity shear tensor is closely related to the density field as it is a measure of the strain of the DM fluid, represented by the diagonal elements of the shear tensor. The classification algorithm given by Hoffman et al. (2012) uses information regarding the strain of the fluid, given by the shear tensor, to classify the cosmic web according to the number of eigenvalues of the symmetric shear tensor greater than a given threshold value. Classifying the cosmic web allows one to explore how different web types affect halo properties (Aragón-Calvo et al. 2007b; Hahn et al. 2007a,b; Aragón-Calvo, Van De Weygaert & Jones 2010a; Cautun, van de Weygaert & Jones 2012; Libeskind et al. 2012a,b; Cautun et al. 2014) and the galaxies within the haloes (Metuki et al. 2014; Nuza et al. 2014).

The aim of this paper is to compare existing cosmic web classification methods with a new approach using a smoothed particle hydrodynamics (SPH) formalism borrowed from the SPH simulation technique that incorporates information from locally defined neighbours to construct the velocity shear tensor. The approach can be applied to haloes directly and produces statistics consistent with current literature (Cautun et al. 2012; Hoffman et al. 2012; Libeskind et al. 2012a,b; Metuki et al. 2014; Nuza et al. 2014). The method allows one to easily incorporate the Hubble flow, which is difficult to account for in grid-based approaches. Thus, by accounting for the expansion between particles, it is shown that a natural explanation can be given for the threshold value adopted in grid-based approaches.

2 THE SIMULATION

The following analysis is based on an N-body simulation employing the GADGET-2 simulation code (Springel 2005) with a cube length of $64\,h^{-1}$ Mpc, a total of 1024^3 particles and a particle mass $m_{\rm p} = 2.1 \times 10^7\,h^{-1}{\rm M}_{\odot}$. Each particle is comprised entirely of DM and the collisional component is ignored. A ΛCDM cosmological model with Planck 2013 parameters was used such that at z=0 the total matter density $\Omega_{\rm m} = 0.31$, cosmological constant $\Omega_\Lambda = 0.69$, baryon density $\Omega_{\rm B} = 0.049$, Hubble constant $H_0 = 100\,h$ km s^{-1} Mpc^{-1} and Hubble parameter $h = 0.678$. The primordial power spectrum index, $n = 0.961$ with a normalization value $\sigma_8 = 0.826$. Classifications were performed at a redshift of 0.

3 METHOD

This section revises the cosmic web classification scheme based on the velocity shear tensor given by Hoffman et al. (2012) and discusses the implementations for the Eulerian and the Lagrangian methods using the full set of simulation particles. Subsequently, we demonstrate that the Lagrangian method can be easily applied to the halo sample, forgoing the need to interpolate the halo classifications from the grid cells. The section concludes with a discussion on the implementation of the Hubble flow which effects a shift of the eigenvalues and, by extension the threshold value needed, permitting a more natural interpretation of the eigenvalues of the velocity shear tensor.

3.1 Web classification using the velocity shear tensor

The rate of deformation of a fluid is a result of velocity gradients. In three-dimensional Cartesian coordinates, the deformation tensor can be expressed as $\partial v_\alpha/\partial r_\beta$ for α, $\beta = x, y, z$. One is able to decompose the rank 2 deformation tensor into its shear (symmetric) and vorticity (antisymmetric) components, respectively, to obtain equation (2).

$$\frac{\partial v_\alpha}{\partial r_\beta} = \frac{1}{2}\left(\frac{\partial v_\alpha}{\partial r_\beta} + \frac{\partial v_\beta}{\partial r_\alpha}\right) + \frac{1}{2}\left(\frac{\partial v_\alpha}{\partial r_\beta} - \frac{\partial v_\beta}{\partial r_\alpha}\right). \quad (2)$$

The shear tensor is of particular interest as the diagonal elements represent the strain (rate of compression or expansion) along a given eigenvector. Hoffman et al. (2012) defines the symmetric component of the deformation tensor as the V-web velocity shear tensor, $\Sigma_{\alpha\beta}$, scaled by the Hubble constant as

$$\Sigma_{\alpha\beta} = -\frac{1}{2H_0}\left(\frac{\partial v_\alpha}{\partial r_\beta} + \frac{\partial v_\beta}{\partial r_\alpha}\right). \quad (3)$$

Exploiting a mathematical property of tensor symmetry, the trace of shear tensor is equal to the sum of the eigenvalues and is proportional to the rate of change of density within the simulation for a comoving observer, since

$$\Sigma^\alpha{}_\alpha = \lambda_1 + \lambda_2 + \lambda_3 = -\frac{1}{H_0}\partial_\alpha v^\alpha = \frac{-(\nabla\cdot \boldsymbol{v})}{H_0} \propto \frac{D\rho}{Dt}, \quad (4)$$

where here we have denoted $\partial_\alpha v^\alpha = \partial v_\alpha/\partial r_\alpha$ while employing summation notation. Defining the V-web shear tensor with a negative sign (equation 3) and sorting the eigenvalues so that $\lambda_1 \geq \lambda_2 \geq \lambda_3$ allows for a useful interpretation as now the largest eigenvalue corresponds to the eigenvector with the fastest rate of collapse. Classification of the cosmic web into four possible environments for DM phase space elements is done by counting the number of eigenvalues above a threshold value $\lambda^{\rm th}$. Historically, $\lambda^{\rm th}$ has been chosen by visual inspection of the cosmic web with a popular value being $\lambda^{\rm th} = 0.44$ (Hoffman et al. 2012; Libeskind et al. 2012a,b); however, this value may vary with different simulation parameters. Voids, sheets, filaments and nodes correspond to 0, 1, 2 or 3 eigenvalues greater than the threshold value, respectively. Observe that when all three eigenvalues are greater than $\lambda^{\rm th}$, all three axes are collapsing yielding a node classification while voids are classified with zero eigenvalues greater than $\lambda^{\rm th}$ indicative of an expansion along all three axes. Filaments exhibit a characteristic collapse along two axes with an expansion along the third, while sheets collapse along one axis and expand along two axes.

3.2 Grid-based method

In order to obtain a benchmark model for the subsequent development of the Lagrangian-based approach, we first present a classification based on the traditional grid-based method. For that purpose, the velocity and density fields are constructed on 128^3, 256^3 and 512^3 grid sizes using 'clouds in cells' (CIC) interpolation over 2 cell lengths.

Increasing the grid size for a fixed particle number inevitably causes empty cells within the grid, particularly at a redshift of zero. The empty cells have an associated zero velocity and impact the CIC algorithm significantly at large grid sizes. For the 256^3 grid, we find one empty cell in the entire simulation volume whereas for the 512^3 grid there are $\sim 2 \times 10^6$ empty cells. This is remedied by assigning a mass averaged velocity to the empty cell using the neighbouring cells contained within a sphere of 3 cell lengths. Empty cells are generally located in underdense regions where the fluid experiences little or no turbulence, thus, the solution is believed to be a reasonable approximation for laminar-like flow.

To remove numerical artefacts introduced by the CIC interpolation, the fields are smoothed with a Gaussian kernel using $\sigma = 1$ cell length. For simplicity, the derivatives are evaluated in k-space after employing a fast Fourier transform of the velocity field. Each grid cell then has an associated shear tensor and a set of three eigenvalues for classification.

3.3 Lagrangian method applied to DM particles

An alternative to grid-based, Eulerian methods for analysing fluid flows is the Lagrangian SPH approach first pioneered by Lucy (1977) and Gingold & Monaghan (1977) whereby the continuous fluid is divided into a set of N discrete fluid elements that are followed throughout the simulation while under the laws of hydrodynamics. SPH methods have long been used for a wide range of astrophysical problems and, due to its Lagrangian nature, the numerical solutions do not suffer from advection errors, possesses good conservation properties and overdensities can be dynamically resolved, see Hernquist & Katz (1989), Valdarnini (2012), Springel (2010) and references within. By analogy one may use a Lagrangian, grid-free, SPH-kernel-based method instead of a grid-based, Eulerian method for computing the gradients of the velocity field. In the following, we will address this method as the smoothed particle dynamics (SPD) approach which uses SPH-kernels exclusively for the computation of dynamical quantities.

The SPH-approach employs a particle representation of the fluid where each particle has a given mass and an associated volume. The physical properties of the fluid at a given position $\boldsymbol{r}$, which may be the location of a particle itself, is then given as a function of the properties of the neighbouring particles located at $\boldsymbol{r}'$ within the smoothing length, h. The smoothing length is an adaptive quantity in that it is commonly chosen to be distance to the nth neighbour. The neighbouring particles' properties are weighted by a kernel function $W(r, h)$ with $r = |\boldsymbol{r} - \boldsymbol{r}'|$. Any smoothed interpolated field $F_{\rm s}(\boldsymbol{r})$ of some field $F(\boldsymbol{r})$ in x dimensions is defined as

$$F_{\rm s}(\boldsymbol{r}) = \int F(\boldsymbol{r}')W(|\boldsymbol{r} - \boldsymbol{r}'|, h)\mathrm{d}^x\boldsymbol{r}', \tag{5}$$

where $W(\boldsymbol{r} - \boldsymbol{r}', h) \to \delta(\boldsymbol{r} - \boldsymbol{r}')$ in the limit as $h \to 0$. This is essentially a convolution of the neighbouring particle properties with the kernel.

In this work, we adopt the cubic spline given by (Springel 2010) with $W(r, h) = w(q)/h^d$, d is the dimension and $q = r/h$. In three dimensions the kernel is given by

$$w(q) = \frac{8}{\pi h^3}\begin{cases} 1 - 6q^2 + 6q^3, & 0 \le q \le \frac{1}{2} \\ 2(1-q)^3, & \frac{1}{2} < q \le 1 \\ 0, & \text{Otherwise} \end{cases} \tag{6}$$

with the kernel dropping to zero at $r = h$. The kernel has the important property of being normalized to 1.

Each particle has an associated mass m_i and one can approximate the volume of the kernel occupied by the particle as $d^3\boldsymbol{r} = m_i/\rho_i$. Discretizing equation (5) and using the 'gather approach', one may approximate the smoothed field with j neighbours as

$$F_{\rm s}(\boldsymbol{r}_i) \simeq \sum_{j=1}^{N} \frac{m_j}{\rho_j} F_j W(|\boldsymbol{r}_i - \boldsymbol{r}_j|, h_i). \tag{7}$$

Thus, for the density field, $F(\boldsymbol{r}) = \rho(\boldsymbol{r}) = \rho_i$ and $F(\boldsymbol{r}') = \rho(\boldsymbol{r}') = \rho_j$ so that the SPH density for the ith particle is given by

$$\rho_i \simeq \sum_{j=1}^{N} m_j W(|\boldsymbol{r}_i - \boldsymbol{r}_j|, h_i). \tag{8}$$

To obtain an expression for the smoothed velocity field, substitute $F(\boldsymbol{r}) = \boldsymbol{v}_i$ into equation (7) for the ith particle to obtain

$$\boldsymbol{v}_{s,i} \simeq \sum_{j=1}^{N} \frac{m_j}{\rho_j} \boldsymbol{v}_j W(|\boldsymbol{r}_i - \boldsymbol{r}_j|, h_i). \tag{9}$$

Continuing with our analysis of cosmic web classification, it is noted in equation (3) that the shear tensor can be calculated using the gradient of the velocity field. The SPD approach exploits a unique property in calculating the velocity gradients; the spatial derivative of a smoothed field results in the derivative only being applied to the kernel, shown in equation (10), for which analytical solutions exist.

$$\frac{\partial F_{\rm s}(\boldsymbol{r}_i)}{\partial \boldsymbol{r}_i} \simeq \sum_{j=1}^{N} \frac{m_j}{\rho_j} F(\boldsymbol{r}_j) \frac{\partial}{\partial \boldsymbol{r}_i} W(|\boldsymbol{r}_i - \boldsymbol{r}_j|, h_i), \tag{10}$$

where $\partial/\partial\boldsymbol{r} = \nabla$. For a constant field equation (10) is generally non-zero; however, using the fact that $\rho(\nabla\boldsymbol{v}) = \nabla(\rho\boldsymbol{v}) + (\nabla\rho)\boldsymbol{v}$ one may obtain equation (11) for the velocity gradient which evaluates to zero for constant velocity fields.

$$\frac{\partial \boldsymbol{v}_{s,i}}{\partial \boldsymbol{r}_i} \simeq \frac{1}{\rho_i} \sum_{j=1}^{N} m_j(\boldsymbol{v}_i - \boldsymbol{v}_j) \frac{\partial}{\partial \boldsymbol{r}_i} W(|\boldsymbol{r}_i - \boldsymbol{r}_j|, h_i) \tag{11}$$

With the SPD techniques, the velocity shear tensor can be defined in terms of neighbouring particle quantities and kernel derivatives. This Lagrangian representation allows one to resolve and classify individual DM particles based on the properties of its neighbouring particles. More generally, it can be applied to any point set, for instance, below we will use DM haloes as the basic point set.

The smoothing length for the ith particle, h_i, is determined as the distance to the furthest of the n nearest neighbours (therefore $q \le 1$ in equation 6). The smoothing length for a fixed neighbour number makes this quantity adaptive in the sense that high-density environments will generate short smoothing lengths and low-density regions will cause long smoothing lengths. An adaptive smoothing length reduces the sampling error for regions of varying density. The variation of nearest neighbour number, n, allows one to explore the effect of the smoothing length on the classification of the cosmic web, akin to variable grid sizes (Section 3.2).

Using a three-dimensional Cartesian coordinate system such that α, β represent coordinates (x, y, z) and i, j as reference to particles to avoid confusion, the α component of the velocity gradient in the β direction for the ith particle can then be expressed as

$$\frac{\partial v^{\alpha}_{s,i}}{\partial \beta} \simeq \frac{1}{\rho_i} \sum_{j=1}^{N} m_j(\boldsymbol{v}^{\alpha}_i - \boldsymbol{v}^{\alpha}_j) \frac{\partial}{\partial \beta} W(|\boldsymbol{r}_i - \boldsymbol{r}_j|, h_i). \tag{12}$$

A k-d tree (Kennel 2004) is used to find the nearest neighbours for each particle and the shear tensor is constructed using 16, 32 and 64 neighbours as in equation (3) by taking the spatial derivatives of the relevant velocity components defined in terms of the SPD quantities and the spatial derivatives of the cubic spline kernel interpolant in equation (6) (see Appendix A).

3.4 Lagrangian method applied to DM haloes

To locate individual haloes the ROCKSTAR halo finder (Behroozi, Wechsler & Wu 2013) is employed. For the halo density calculation in equation (8), we avoid ambiguities introduced through halo and sub-halo mass determinations by using a kernel weighted halo number density instead of a mass density. Plugging halo positions and velocities into equation (12) allows one to construct the shear tensor based on the halo sample. In the same manner as for simulation particles, each halo can be classified using the velocity shear tensor (Hoffman et al. 2012). With the intention of applying the new Lagrangian method to observed galaxy samples, a maximum circular velocity ($v_{\rm max}$) cut-off of 50 km s^{-1} is employed for the haloes and subhaloes. A $v_{\rm max}$ limit applied to the halo catalogue can be used instead of a mass limit as it avoids the ambiguous calculation of the virial mass for both haloes and subhaloes and is more robust with regards to the central dynamics within haloes where galaxies are thought to be found (Kravtsov et al. 2004; Klypin, Trujillo-Gomez & Primack 2011). One may adopt the Tully–Fisher relation (Tully & Fisher 1977) to deduce a near-infrared limiting magnitude of ~ -17 (Bell & de Jong 2001; Pizagno et al. 2007; Torres-Flores et al. 2011), corresponding to a galaxy sample luminosity limit of $\sim 10^9$ L$_\odot$. Restricting the sample to a $v_{\rm max} \geq 50$ km s^{-1} range may neglect small faint dwarf galaxies however the majority of spirals and early-type galaxies are well within this range (Trujillo-Gomez et al. 2011). Locating and classifying haloes naturally skews the sampling to the denser web types, such as filament, sheets and nodes, as haloes are a biased tracers of the mass distribution in the cosmic web. Classifying individual haloes using the halo-based Lagrangian approach is computationally very cheap as halo catalogues are small relative to particle numbers.

3.5 Hubble flow

An aspect intrinsically difficult to accommodate in the grid-based approach is the inclusion of the Hubble flow. Cosmological *N*-body simulations utilize comoving coordinates thus the velocities of the simulation particles only reflect peculiar motion. As a consequence, virialized haloes which are expected to show a mean radial velocity equal to zero always show a mean inward motion proportional to the radius. In other words, virialized haloes shrink if only peculiar velocities are considered. This spurious effect can be easily corrected for by adding the radially outwards pointing Hubble flow, $\propto Hd$, with respect to an arbitrary centre (naturally the position of the central object).

The local nature of the Lagrangian approach effortlessly permits the inclusion of the Hubble flow between a given particle and its neighbours. Incorporating the Hubble flow naturally counteracts the artificial contraction between particles which may explain why $\lambda^{\rm th}$ has to be set to some arbitrary value greater than zero when failing to account for the radially outward flow. Doing so, using $\lambda^{\rm th} = 0$, leads to very similar results when compared to classification without the inclusion of the Hubble flow and setting $\lambda^{\rm th} > 0$. This allows for a straightforward interpretation of the eigenvalues as now negative eigenvalues correspond to expansion and positive eigenvalues indicate contraction along a specific eigenvector.

4 RESULTS

In this section, we fist discus the results obtained with the grid-based method. This serves as benchmark model which is to be compared with the literature on the one side and with the results based on the SPD method on the other side. Subsequently, the SPD method is applied to the simulation particle distribution and the halo sample. Finally, the results effected by the Hubble flow correction are discussed.

4.1 Grid-based method

The normalized distribution of eigenvalues for the grid-based velocity shear tensor can be found in Fig. 1 (top), using various grid sizes. The distributions are consistent with the results found in Libeskind et al. (2012b), following an approximate lognormal distribution. Probability density functions (PDFs) for the 128^3 and 256^3 grids display the characteristic peaks (widths) increasing (decreasing) from $\lambda_1 \rightarrow \lambda_3$. Wider widths in λ_1 relative to λ_3 suggest there is more variation in the strength of expansion (collapse) along the corresponding eigenvector.

A finer grid increases the proportion of λ_3 eigenvalues found in the lower limit of the range, evident in the decreasing peaks. Distribution peaks for λ_2 steadily rise for a finer grid, the PDFs for λ_1 are relatively unchanged. The effects of constraining or relaxing expansion (collapse) through varying grid size is purely numerical.

Volume filling fractions ($V_{\rm ff}$) and mass fractions ($M_{\rm f}$) for the various grid sizes can be found in Table 1. The fractions are in agreement with current literature (Hoffman et al. 2012; Metuki et al. 2014) and show voids occupy the largest volume of the cosmic web followed by sheets, filaments and nodes. Filaments and sheets are shown to be the most massive web types with nodes and voids making up the balance.

A finer grid results in lower mass fractions for voids and nodes. This may be explained by the fact that a higher spatial resolution tends to 'de-homogenize' the eigenvalues, i.e. if all three eigenvalues are above (below) the threshold for a cell at low resolution then the fine structure within the cell resolved by the finer grid causes one or two eigenvalues to shift below (above) the threshold within the new cells transforming voids or nodes into sheets and filaments. This would naturally account for the behaviour of the mass fractions of sheets and filaments which are observed to increase with grid size. The volume filling fractions are relatively consistent for all grid sizes. We use the results based on the 256^3 grid as the benchmark.

4.2 DM particles: Lagrangian method

Fig. 1 (middle) shows the distribution of eigenvalues for the Lagrangian approach for all 1024^3 DM particles neglecting the Hubble flow. The normalized distributions obey similar statistical properties as the PDFs for the grid-based method with a lognormal representation and the same eigenvalue width dependence. One observes a similarity between the distributions of finer grids and smaller neighbour numbers; a low neighbour number requirement enforces shorter smoothing lengths, a smoothing scale that is comparable with a very fine grid. Conversely, a coarser grid is a result of a larger smoothing scale, or more neighbours.

Comparing the grid-based eigenvalues with the Lagrangian-based eigenvalues excluding Hubble flow, one notes that the peaks for the SPD formulated eigenvalues are shifted slightly towards larger values when compared to their grid-based counterparts for any neighbour number or grid size. The SPD-based PDFs tend to have more extended tails with a larger proportion of eigenvalues with absolute values $|\lambda_i| > 1$.

SPD results based on 16 neighbours need to be treated with caution due to the low number statistics. Even if the overall trends are

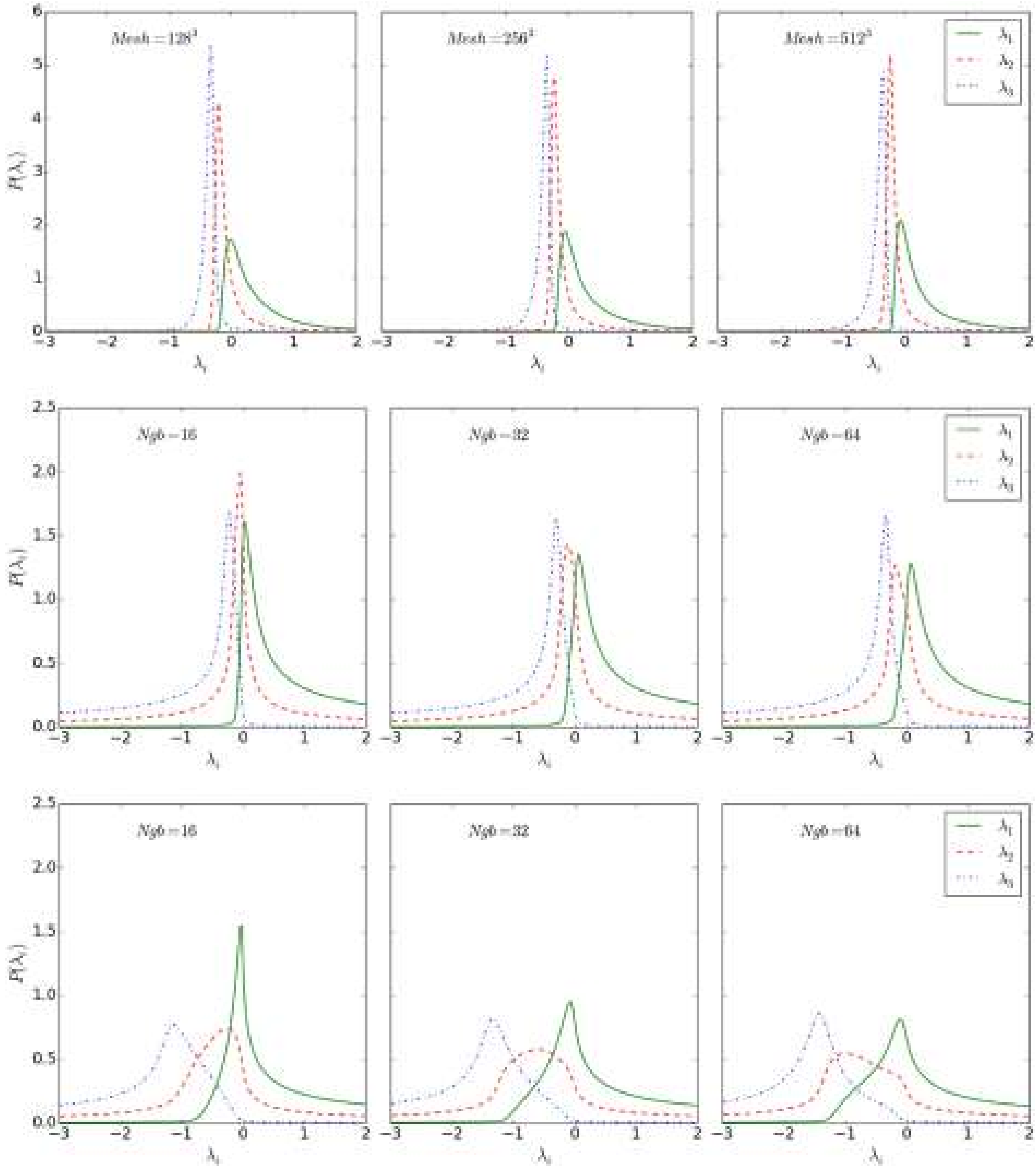

Figure 1. Top: the PDFs for eigenvalues using varying grid sizes: 128^3 (left), 256^3 (middle) and 512^3 (right). λ_1 is given by the green solid line, λ_2 is given by red dashed line and λ_3 is given by the blue dot–dashed line. Middle: the PDFs for Lagrangian-based eigenvalues using a varying number of neighbours: 16 (left), 32 (middle) and 64 (right) with the same line properties as above. Bottom: Lagrangian-based PDFs for the 1024^3 particles incorporating the Hubble flow into the velocities before the shear is determined, using the same neighbour numbers and line properties as above. Distributions are approximately lognormal; a finer mesh is attributed with shorter smoothing lengths or fewer neighbours (neglecting the Hubble flow).

similar to the grid-based approach, we mainly use the 16 neighbour PDFs to explore the impact of small neighbour numbers on the eigenvalue distribution. The 16 nearest neighbour results are not discussed further.

Using 64 neighbours leads to a spurious behaviour for the PDFs, which is most obvious for the λ_2 eigenvalue distribution and is evident by a bump around zero. The effect is even more pronounced in Fig. 1 (bottom right) using 64 neighbours incorporating the Hubble flow. This is believed to be a non-physical artefact as a result of known integral interpolant errors, $\mathcal{O}(h^2)$, associated with larger smoothing lengths due to larger neighbour numbers (Monaghan 2005).

The Lagrangian method, without Hubble flow, using 32 neighbours produces eigenvalue distributions and mass fraction statistics, seen in Table 2, that best match current literature (Cautun et al. 2012; Hoffman et al. 2012; Libeskind et al. 2012b; Metuki et al. 2014).

Table 1. Volume and mass filling fractions: mesh-based method using $\lambda = 0.44$.

	Mesh	Voids	Sheets	Filaments	Nodes
$V_{\rm ff}$	128^3	67.80 %	26.27 %	5.40 %	0.53 %
	256^3	67.46 %	27.28 %	4.87 %	0.39 %
	512^3	68.93 %	26.81 %	4.02 %	0.24 %
$M_{\rm f}$	128^3	17.88 %	31.96 %	34.28 %	15.88 %
	256^3	13.80 %	36.28 %	38.18 %	11.74 %
	512^3	12.47 %	40.63 %	38.73 %	8.17 %

Table 2. Mass fractions: SPH particle method with and without Hubble flow comparing $\lambda^{\rm th} = 0.44$ & $\lambda^{\rm th} = 0.0$ for 32 neighbours.

Without Hubble flow	Voids	Sheets	Filaments	Nodes
$\lambda^{\rm th} = 0.44$	10.62 %	50.70 %	37.53 %	1.15 %
$\lambda^{\rm th} = 0.0$	2.92 %	51.36 %	44.31 %	1.42 %
With Hubble flow	Voids	Sheets	Filaments	Nodes
$\lambda^{\rm th} = 0.44$	14.77 %	49.50 %	34.70 %	1.04 %
$\lambda^{\rm th} = 0.0$	10.61 %	50.81 %	37.50 %	1.13 %

PDFs for 32 neighbours display the properties of decreasing peaks and increasing widths for $\lambda_3 \rightarrow \lambda_1$ which can also be observed in the benchmark grid-based PDFs. In addition to this, the choice of 32 particles is a standard number of neighbours in SPH simulations. For this reason, the SPD halo analysis will resume using 32 neighbours as the benchmark.

Fig. 1 (bottom) shows the normalized eigenvalue PDFs for the Lagrangian method taking into account the Hubble flow. The expansion (collapse) is again more relaxed relative to the grid-based approach, exhibiting more pronounced tails and a larger range. Other statistical properties, such as lognormality and decreasing widths still hold, however, these features are far less obvious. One may observe an approximate symmetry using 32 and 64 neighbours whereby λ_3 is a negative reflection of λ_1 around $\lambda_i \sim -0.5$. Libeskind et al. (2012b) suggests this relation would imply expansion and collapse are equivalent processes but in opposite directions.

The mass fraction for each web type is shown in Table 2 with and without Hubble flow using $\lambda^{\rm th} = 0.44$ and 0.0. Using $\lambda^{\rm th} = 0.44$ without Hubble flow results in mass fractions for voids and filaments that are similar to those for the grid classification; however, sheets occupy a larger proportion of the total mass within the cosmic web while nodes are responsible for a very small amount of the web mass. The low node fractions for all SPD classifications may be attributed to the fact that for a given particle, collapse along all three axes is quite difficult to achieve. Each particle experiences a range of tidal forces, due to its neighbouring particle distribution, which in turn will mitigate a complete gravitational collapse inward. Mesh-based approaches do not suffer from this problem as particles are enclosed in individual cells and the CIC interpolation smooths out the gravitational tidal forces to a large degree.

Accounting for the Hubble flow naturally introduces an expansion in all directions, increasing void classifications at any given threshold. Using $\lambda^{\rm th} = 0.0$ with Hubble flow produces almost identical mass fractions to $\lambda^{\rm th} = 0.44$ without Hubble flow, validating the inclusion of the Hubble flow in the classification calculation. This also explains why it is necessary to introduce a threshold value greater than zero in the grid-based approach.

The top panels of Fig. 2 show the number fraction, $N_{\rm f}$, for web types as a function of the threshold value $\lambda^{\rm th}$. On the left we find the results without Hubble flow. On the right-hand panel, the Hubble flow is added, i.e. each neighbour particle is attributed with an additional radial velocity according to the Hubble law before the shear tensor is computed. The number fraction curves with and without Hubble flow are almost identical, except that inclusion of the Hubble flow requires a shift of the threshold value towards the left by approximately 0.44. This value roughly corresponds to the threshold value employed for the grid approach. Consequently, the curves show very similar number fractions when a threshold values of 0.44 and 0 are used for the data without and with Hubble flow, respectively.

The bottom panels of Fig. 2 show the same curves for the halo sample. Details will be explored further in Section 4.3. Here we only remark that the shapes of curves without (left) and with (right) the Hubble flow are very similar if shifted by ~ -0.44, exactly as observed for the particle sample.

Volume filling fractions are not straightforwardly extractable using the Lagrangian method as one does not classify the entire cosmological volume composed of individual cells but rather individual particles, which does not allow for a trivial summation of the volume.

The top panel of Fig. 3 shows the contoured DM distribution within a slice of $0.5\,h^{-1}$ Mpc thickness projected along the z axis on to the x–y plane. The filamentary web structure is highlighted by the grey-scale contours whereby regions of increasing density are clearly identifiable by the lighter shades of grey. The lightest contours enclose the densest regions of the slice where many particles have collapsed to form nodes, while less dense elongated filaments are captured by the light grey contours forming the web-like structure in the space between the nodes. The darker shades of grey to black indicate lower density regions where one expects to observe sheet and void web types.

The middle and bottom panels of Fig. 3 display the same slice classifying each particle using a 256^3 grid-based method (middle) and 32 neighbours Lagrangian method with Hubble flow (bottom), using $\lambda^{\rm th} = 0.44$ and 0.0, respectively. The SPD-based classification scheme (bottom) resolves more details, for example many more small DM particles within the filaments are identified as nodes. The very same particles are classified as filaments or sheets by the grid-based approach. This result is due to the adaptive nature of the SPD approach. Despite the larger number of classified nodes depicted here, the mass fraction for nodes derived from the Lagrangian method is lower compared to the grid-based approach.

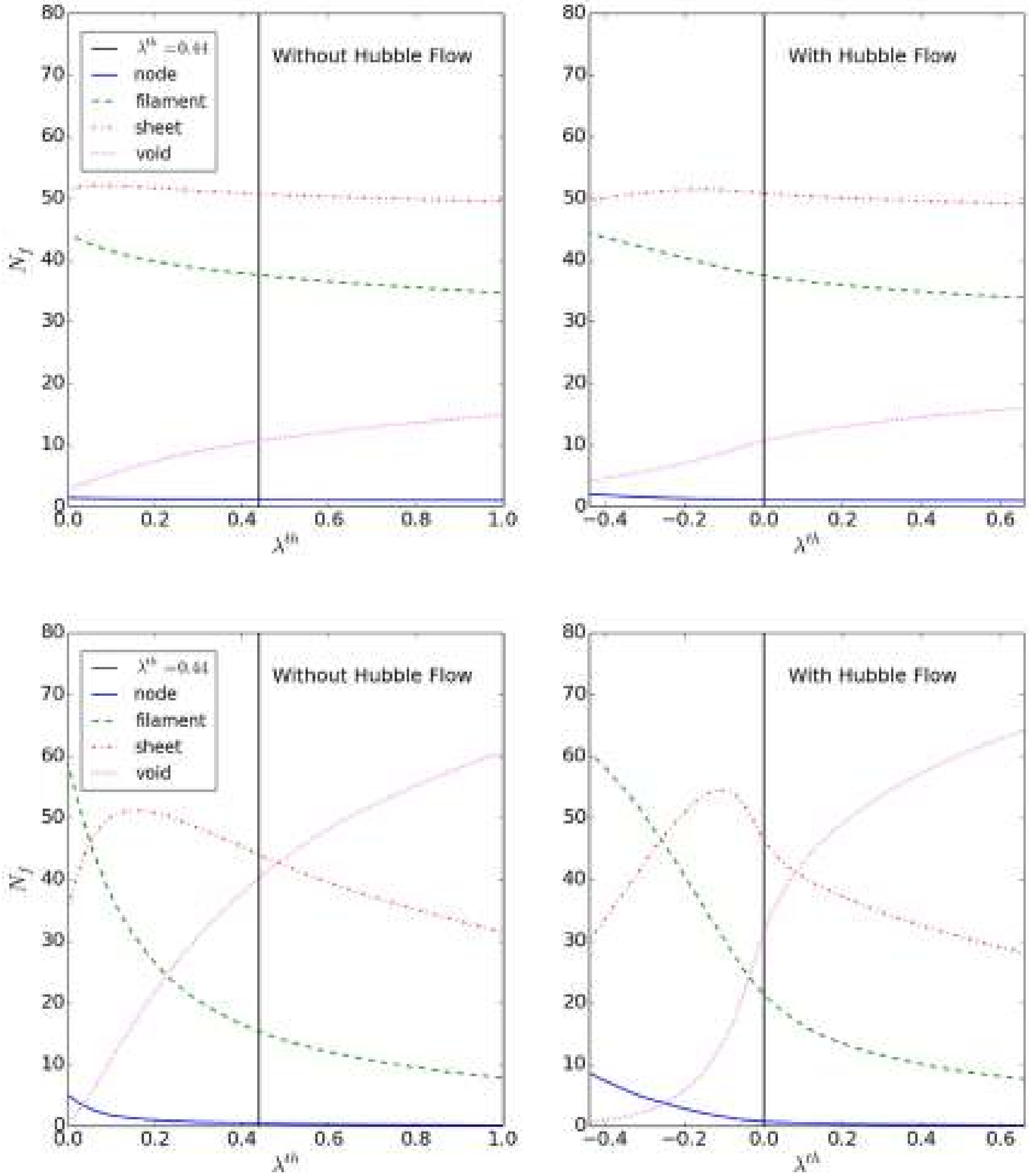

Figure 2. Changing $\lambda^{\rm th}$ and its effect on the $N_{\rm f}$ of classified web types for the DM particles (top) and haloes (bottom) without (left) and with (right) Hubble flow. Threshold values are given by the black vertical lines at $\lambda^{\rm th} = 0.44$ and $\lambda^{\rm th} = 0.0$ excluding and including the Hubble flow, respectively. Nodes are shown by the solid blue line, filaments are dashed green, sheets dot–dashed red and voids dotted magenta. Number fractions are very similar at any threshold value both with and without Hubble flow when shifting the Hubble flow threshold value by $\sim-$ 0.44.

4.3 Lagrangian application to haloes

The goal of the cosmic web classification discussed above is to determine the environment that the galaxies inhabit. This allows one to investigate the impact of the environment on galaxy evolution which is crucial to understanding the diversity of galaxy populations. Galaxies are thought to be hosted by DM haloes. Thus, once the web classification (independent of whether grid or particle based) is completed the various web types have to be assigned to DM haloes (i.e. galaxies). This is accomplished with interpolation schemes which allow for the transition between the grid or particle distributions to halo locations.

Alternatively, the Lagrangian method introduced above can be directly applied to the halo sample, i.e. the velocity shear tensor and its eigenvalues can be computed for an individual halo by utilizing the positions and velocities of its nearest neighbour haloes. For the subsequent analysis, the velocity shear tensor was computed based on the 32 nearest neighbour haloes.

The two bottom panels of Fig. 2 show the fraction of haloes belonging to a particular web type as a function of the threshold value $\lambda^{\rm th}$. The bottom-left panel of Fig. 2 displays the halo classification without Hubble flow; nodes and filaments are monotonically decreasing with nodes making up a very small percentage as $\lambda^{\rm th}$ increases. Voids are underrepresented at low threshold values. Sheet

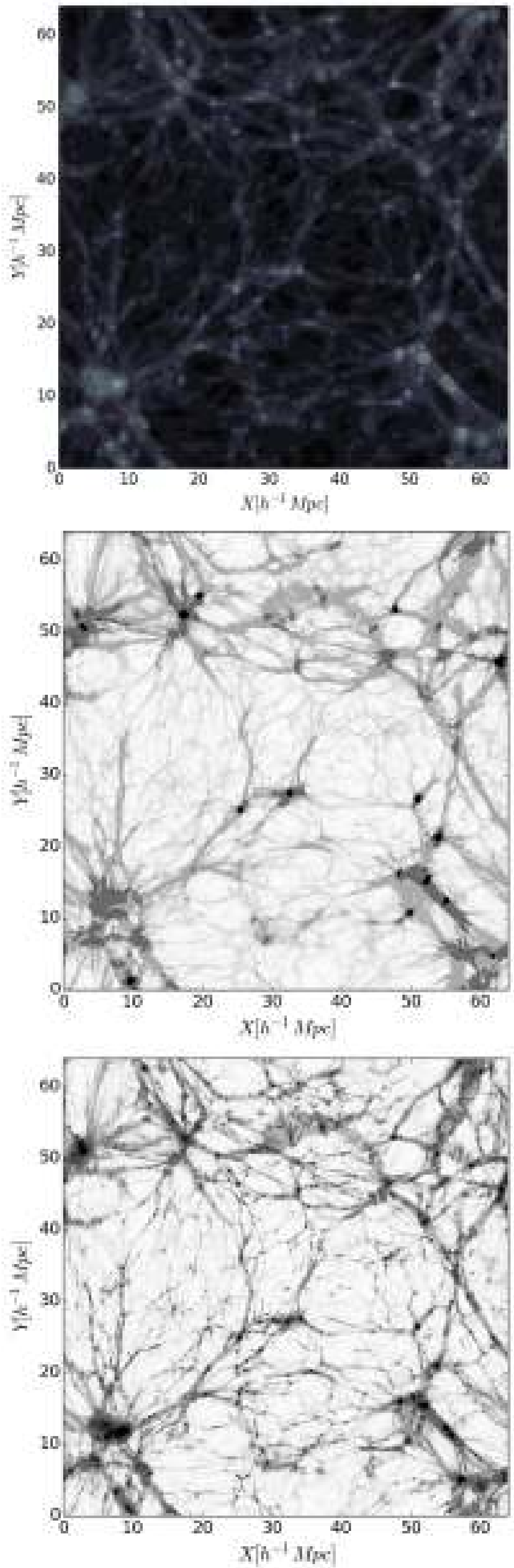

Figure 3. A slice $0.5\,h^{-1}$ Mpc thick showing the log scaled DM density distribution (top). Contours enclose increasingly overdense regions with a lighter grey-scale. The mesh-based classification using $\lambda^{\rm th} = 0.44$ is shown in the middle subfigure and the Lagrangian classifier including Hubble flow using $\lambda^{\rm th} = 0.0$ is shown in the bottom subfigure. Voids, sheets, filaments and nodes are represented by the light, medium, dark grey and black dots, respectively.

fractions initially rise when moving to a higher threshold value but begin to decrease after $\lambda^{\rm th} \gtrsim 0.15$.

The addition of the Hubble flow in the bottom-right panel of Fig. 2 does not drastically change the shape of the number fraction curves for different web types but seems to just shift the curves leftwards. Observe the similarity of the curves to the right of the given threshold values (black vertical line) with and without Hubble flow. The threshold values at $\lambda^{\rm th} = 0.44$ without Hubble flow and $\lambda^{\rm th} = 0.0$ with Hubble flow offer very similar number fractions which is further confirmed in Table 3. As already discussed for the particle-based classification scheme, one is compelled to conclude that the determination of $\lambda^{\rm th} = 0.44$ by visual inspection (Hoffman et al. 2012) can be understood as an effective quantity accommodating for the Hubble flow lacking in the grid-based method.

The halo eigenvalue PDFs are presented in Fig. 4 both with and without Hubble flow. The left-hand panel of Fig. 4 neglects the Hubble flow. The results are in agreement with both the grid-based as well as the SPD particle-based distributions in Fig. 1 (top and middle), obeying similar statistical properties. Including the Hubble flow produces the distributions displayed in the right-hand panel of Fig. 4). These curves exhibit a reversal of properties, the widths are increasing and peaks are decreasing moving from $\lambda_1 \rightarrow \lambda_3$. Although the method is still SPD based, the wide tails seen in the particle distributions of Fig. 1 (middle and bottom) have vanished. This has the effect of constraining the strength of expansion (collapse) in the halo-based regime.

Maximum circular velocity, $v_{\rm max}$, is a measure of the gravitational potential well for each halo and serves as a proxy for galaxy luminosity. Fig. 5 shows the maximum circular velocity function for the different web types. Haloes classified as nodes are higher density web types and as such make up the majority of high $v_{\rm max}$ haloes extending to $\sim$1200 km s^{-1}. Underdense web types such as voids are associated with lower $v_{\rm max}$ values $\lesssim 450$ km s^{-1}. The majority of haloes between 400 and 1000 km s^{-1} are classified as filaments which are followed by sheets. We observe a correlation between web type and $v_{\rm max}$ using the SPD approach similar to the mass–web type relation found in Hahn et al. (2007b), Cautun et al. (2012) and Metuki et al. (2014).

Fig. 6 shows a 5 h^{-1} Mpc slice of the haloes classified using the SPD approach with Hubble flow and $\lambda^{\rm th} = 0.0$. The halo size is plotted proportional to the maximum circular velocity. The apparent structure further supports the $v_{\rm max}$–web type correlation. Voids are generally relatively small circles increasing for sheets, filaments and nodes, respectively. Fig. 6 establishes the success of the Lagrangian, halo-based, web classification approach. It is an effective way to determine the environment within which haloes reside.

Finally, we examine the density–web type relation via the fractional density $\Delta = \rho/\bar{\rho}$ for each halo by constructing spheres of radius $0.5\,h^{-1}$ Mpc around the centre of each halo and calculating Δ within that sphere, referred to as *background density* in the following. The eigenvalues of the velocity shear tensor were calculated by incorporating the Hubble flow and the classification was performed using a threshold value of zero. The normalized distribution of halo background densities classified by web type can be seen in Fig. 7, left-hand panel.

For $\Delta \lesssim 10$ the behaviour meets one's expectations. The web types are tiered with void haloes being found at the lowest background densities followed by filament, sheet and node type haloes, respectively. However, the behaviour at high background densities is counterintuitive. Akin to the background density problem discussed in Hoffman et al. (2012), we find that at high background

Table 3. SPH halo number fractions ($N_{\rm f}$) using 32 neighbours with and without Hubble flow comparing $\lambda^{\rm th} = 0.0$ & $\lambda^{\rm th} = 0.44$.

Without Hubble flow	Voids	Sheets	Filaments	Nodes
$\lambda^{\rm th} = 0.44$	40.25 %	43.96 %	15.37 %	0.41 %
$\lambda^{\rm th} = 0.0$	0.82 %	35.04 %	59.03 %	5.01 %
With Hubble flow	Voids	Sheets	Filaments	Nodes
$\lambda^{\rm th} = 0.44$	58.52 %	31.76 %	9.52 %	0.20 %
$\lambda^{\rm th} = 0.0$	31.31 %	46.50 %	21.44 %	0.74 %

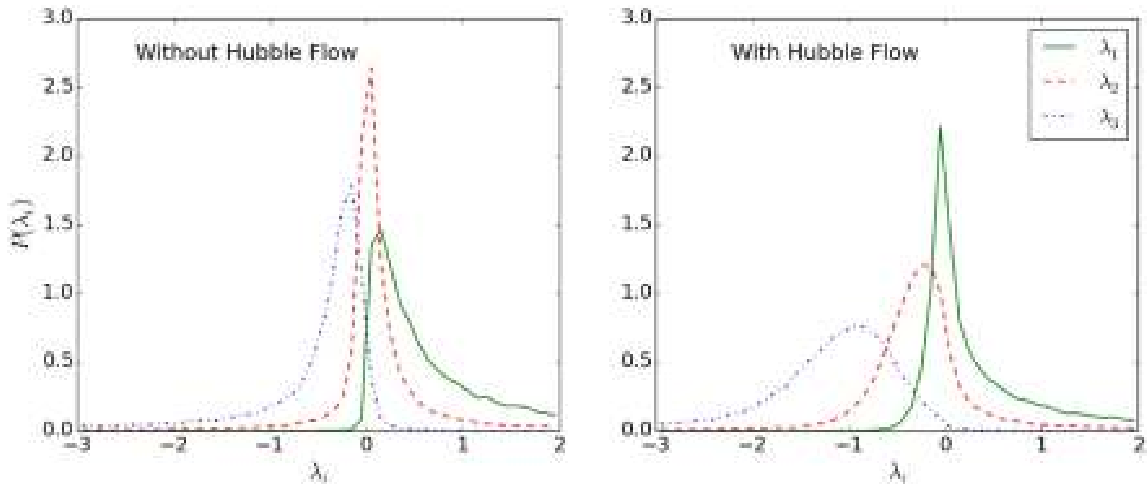

Figure 4. Left: the normalized PDFs for halo eigenvalues using 32 neighbours without Hubble flow. Colour codes and line styles are defined as in Fig. 1. Right: PDFs for halo eigenvalues taking into account the Hubble flow for 32 neighbours. Including the Hubble flow reverses the statistical properties previously observed, a more varied strength of expansion (collapse) is seen along the respective eigenvectors moving from $\lambda_1 \rightarrow \lambda_3$.

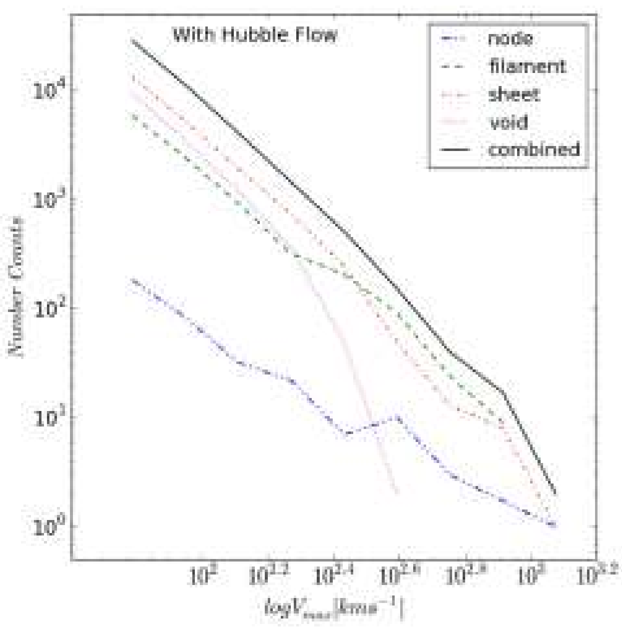

Figure 5. Maximum circular velocity as a function of web type for nodes (blue dash–double dotted), filaments (green dashed), sheets (red dash–dotted) and voids (dotted magenta). The computation of the shear tensor was based on the 32 nearest neighbour haloes with the Hubble flow added to the halo velocities. For the separation of the eigenvalues (collapsing/expanding) a threshold value of 0.0 was implemented. The velocity function for voids is very steep indicating that there are no high-velocity haloes in voids. On the other hand, the node velocity function is quite flat allowing for the highest circular velocity haloes to be classified as node haloes.

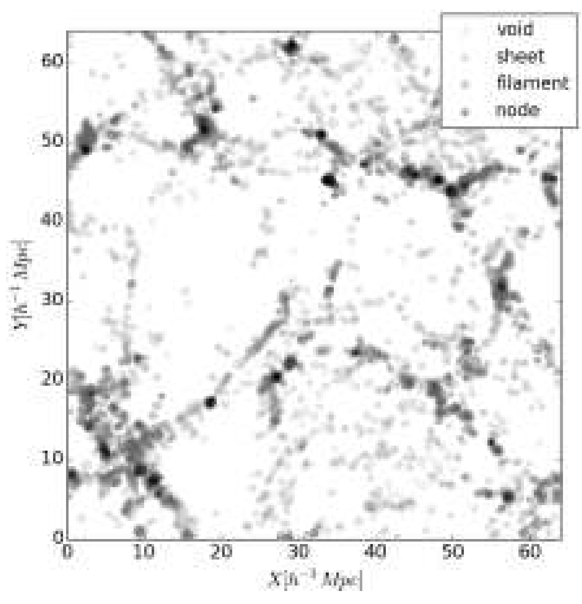

Figure 6. A 5 h^{-1} Mpc slice showing the classified haloes using 32 neighbour haloes accounting for the Hubble flow. The size of the markers are scaled according to the $v_{\max}$ of each halo. Larger haloes are generally classified as residing in a denser web type, the smallest haloes classified as void haloes and the largest as filament and node haloes.

densities, the PDFs for haloes associated with sheet, filament and node web types show only week differences. In addition, a small number of instances can be observed where void type haloes are associated with high background densities.

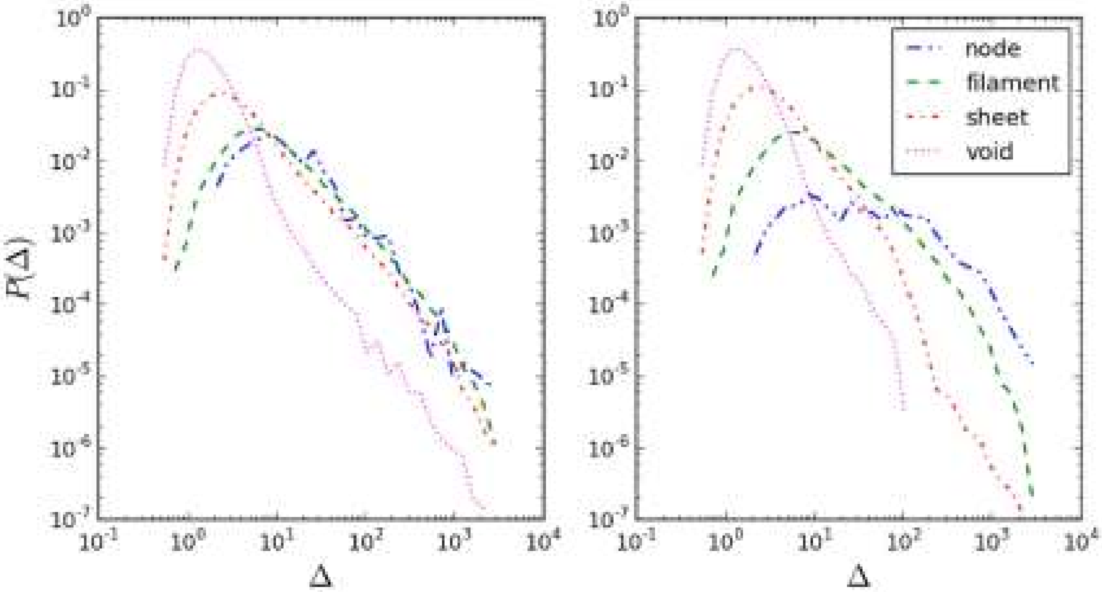

Figure 7. The PDFs for halo fractional density, measured in halocentric spheres of $0.5\,h^{-1}$ Mpc, per web type possessing the same line properties as in Fig. 5. Contrary to expectations, the left-hand panel shows very similar behaviour for sheet, filament and node web types at high fractional densities. Also, the (small number) of high densities for void haloes is counterintuitive. The right-hand panel shows the PDFs of the halo fractional densities after reclassification - assigning the densest web type in the parent-subhalo system to all haloes within the system. This correction offers a more intuitive density–web type correlation as lower density web types (voids, sheets) are now severely restricted in the fractional density domain and only high-density web types (nodes, filaments) exhibit large fractional densities.

The classification problems may be largely due to the inclusion of subhaloes in classification scheme. The dynamic resolution of the SPD approach captures the small-scale dynamics between host and subhaloes, negating the gradient of the velocity field seen on larger scales.

Misclassifications may be remedied through a reclassification process by adopting the following modification: assign to a given main halo and all its subhaloes, the highest density web type found within that particular halo–subhalo system. This correction assigns the classification of the parent halo to its subhaloes only 20 per cent of the time indicating that the classification of the main halo is strongly influenced by small-scale dynamics. With this scheme, an improvement in the density–web type relation can be achieved as demonstrated in the right-hand panel of Fig. 7.

Corrected background density PDFs exhibit more favourable properties as the higher density web types now possess the largest background densities. Void haloes exhibit maximum overdensities of ∼100, increasing for sheets ($\Delta \lesssim 3600$), filaments ($\Delta \lesssim 3800$) and nodes ($\Delta \lesssim 4000$), respectively. Correcting the classification also improves overall number fractions for the haloes; nodes, sheets, filaments and voids now contribute 5.50, 33.41, 42.51 and 18.59 per cent to the number fraction, respectively, compared with Table. 3 with Hubble flow, $\lambda^{\rm th} = 0.0$. Since haloes trace the densest regions of the cosmic web, an increase in higher density web types such as nodes and filaments and a decrease in underdense voids and sheets is a welcomed result following the reclassification. It must be noted that computing the fractional densities using a more trivial grid-based approach yields very similar results.

Using $v_{\rm max}$ as the limiting quantity for the halo catalogue serves to ensure the halo sample resembles galaxy surveys. To observe the background density for web types of main haloes only, we recompute the shear tensor eigenvalues using the existing $v_{\rm max}$ limit. The results of which may be found in Fig. 8. The density–web type correlation, for main haloes only, shows a significant improvement when compared to the left-hand panel of Fig. 7. Low-density web types dominate the fraction of background densities found below $\Delta \lesssim 10$, while node haloes are seen to occupy the majority of mid-to-high background densities. A few outlying haloes classified as

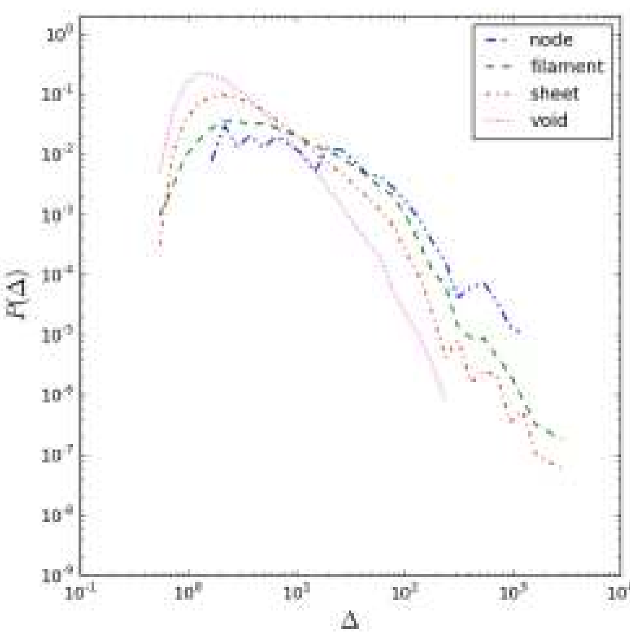

Figure 8. Recomputing the shear tensor using parent haloes only. Voids, sheets, filaments and nodes are identified using the same line properties as in Fig. 5. The background density–web type relation is largely improved by further limiting the sample. As expected, the majority of low-density web types are assigned smaller densities $\rho \lesssim 10\bar{\rho}$. Meanwhile, the main haloes exhibit a more tiered effect at higher background densities comparable to the right-hand panel of Fig. 7.

sheets and filaments extend out to the maximum background density of $\Delta \sim 10^{3.5}$.

5 CONCLUSIONS

Galaxy formation and evolution is a poorly understood topic and classifying the cosmic web serves as a crucial step in the analysis of the galaxy–environment relationship. Existing methods of cosmic web classification have used Eulerian, grid-based, techniques to classify the cosmic web using a visually defined threshold value.

Here we have proposed a new Lagrangian, SPD-based, method for the classification of the cosmic web. The SPD approach offers an alternative numerical method for classifying the cosmic web that benefits from the SPH implementation used to define particle quantities. The SPD-based classifier draws on the local properties of the underlying discretized density and velocity field to calculate the shearing rate of a fluid in the kernel volume for a given particle or halo.

The variable smoothing length allows for greater adaptivity, as is evident by the methods' ability to resolve and classify smaller substructure compared to grid-based methods. This capability may be an advantage or disadvantage, depending on the problem envisaged.

Our analysis set out to reproduce results obtained with the Eulerian approach as a benchmark. Good agreement between (particle-based) Eulerian and Lagrangian classification schemes is demonstrated. The distribution of eigenvalues for the Eulerian approach and the Lagrangian approach possess similar statistical properties. The mass and number classification fractions in the SPD approach are underestimated for nodes but are otherwise very similar for the remaining web types. The lack of node classifications may be due to the nature of the SPD approach as it captures tidal forces that may prevent a complete collapse along all three eigenvectors.

The Lagrangian representation classifies individual DM particles according to the properties of the nearby particle neighbourhood and allows for an easy inclusion of the Hubble flow between neighbouring particles or haloes. The addition of the Hubble flow removes the need for an arbitrary threshold value and sets the threshold value to zero irrespective of simulation parameters.

Classifying the cosmic web using the new SPD scheme is ideally suited to studying galactic properties as galaxies and the haloes in which they reside are a function of the external environment and trace the densest regions of the DM phase space. Directly applying the new technique to the halo sample yields good agreement with halo classifications based on the interpolation of the particle-based Eulerian approach. High maximum circular velocity haloes are more likely to be classified as a denser web type. Haloes in high-density regions, classified as nodes and filaments, exhibit large $v_{\max}$ values whilst underdense regions such as voids are typically endowed with much smaller $v_{\max}$ values.

The fractional density distribution initially showed a poor correlation with web type largely due to misclassified subhaloes, however by modifying the classification routine, so all halo–subhalo systems are assigned the highest density web type within the system, helps to correct for the misclassified haloes. This reduces the upper limit of the fractional densities in lower density web types and improves the number fractions for node and filament haloes.

ACKNOWLEDGEMENTS

The authors gratefully acknowledge valuable suggestions from the referee, Noam Libeskind, and fruitful discussions with Sean February and the use of computing resources at the Centre for High Performance Computing (CHPC South Africa) as well as the support from the National Astrophysics and Space Science Programme (NASSP).

REFERENCES

Aragón-Calvo M. A., Van De Weygaert R., Jones B. J. T., 2010a, MNRAS, 408, 2163
Aragón-Calvo M. A., Platen E., van de Weygaert R., Szalay A. S., 2010b, ApJ, 723, 364
Aragón-Calvo M. A., Jones B. J. T., van de Weygaert R., van der Hulst J. M., 2007a, A&A, 474, 315
Aragón-Calvo M. A., van de Weygaert R., Jones B. J. T., van der Hulst J. M., 2007b, ApJ, 655, L5
Behroozi P. S., Wechsler R. H., Wu H.-Y., 2013, ApJ, 762, 109
Bell E. F., de Jong R. S., 2001, ApJ, 550, 212
Blanton M. R., Eisenstein D., Hogg D. W., Schlegel D. J., Brinkmann J., 2005, ApJ, 629, 143
Bond J. R., Kofman L., Pogosyan D., 1996, Nature, 380, 603
Cautun M., van de Weygaert R., Jones B. J. T., 2012, MNRAS, 429, 1286
Cautun M., van de Weygaert R., Jones B. J. T., Frenk C. S., 2014, MNRAS, 441, 2923
Colombi S., Pogosyan D., Souradeep T., 2000, Phys. Rev. Lett., 85, 5515
Dressler A., 1980, ApJ, 236, 351
Falck B. L., Neyrinck M. C., Szalay A. S., 2012, ApJ, 754, 126
Faltenbacher A., 2010, MNRAS, 408, 1113
Forero-Romero J. E., Hoffman Y., Gottlöber S., Klypin A., Yepes G., 2009, MNRAS, 396, 1815
Frisch U., Matarrese S., Mohayaee R., Sobolevski A., 2002, Nature, 417, 260
Gao L., Springel V., White S. D. M., 2005, MNRAS, 363, L66
Gingold R. A., Monaghan J. J., 1977, MNRAS, 181, 375
Hahn O., Porciani C., Carollo C. M., Dekel A., 2007a, MNRAS, 375, 489
Hahn O., Carollo C. M., Porciani C., Dekel A., 2007b, MNRAS, 381, 41
Hernquist L., Katz N., 1989, ApJS, 70, 419
Hoffman Y., Metuki O., Yepes G., Gottlöber S., Forero-Romero J. E., Libeskind N. I., Knebe A., 2012, MNRAS, 425, 2049
Kennel M. B., 2004, preprint (arXiv:physics/0408067)
Klypin A. A., Trujillo-Gomez S., Primack J., 2011, ApJ, 740, 102
Kravtsov A. V., Berlind A. A., Wechsler R. H., Klypin A. A., Gottlober S., Allgood B., Primack J. R., 2004, ApJ, 609, 35
Kuhlen M., Vogelsberger M., Angulo R., 2012, Phys. Dark Universe, 1, 50
Libeskind N. I., Hoffman Y., Knebe A., Steinmetz M., Gottlöber S., Metuki O., Yepes G., 2012a, MNRAS, 421, L137
Libeskind N. I., Hoffman Y., Forero-Romero J., Gottlober S., Knebe A., Steinmetz M., Klypin A., 2012b, MNRAS, 428, 2489
Lucy L. B., 1977, AJ, 82, 1013
Metuki O., Libeskind N. I., Hoffman Y., Crain R. A., Theuns T., 2014, MNRAS, 446, 1458
Monaghan J. J., 2005, Rep. Prog. Phys., 68, 1703
Nuza S. E., Kitaura F.-S., Hess S., Libeskind N. I., Mueller V., 2014, MNRAS, 445, 15
Pizagno J. et al., 2007, AJ, 134, 945
Platen E., Van De Weygaert R., Jones B. J. T., 2007, MNRAS, 380, 551
Schaap W. E., van de Weygaert R., 2000, A&A, 363, L29
Sousbie T., 2011, MNRAS, 414, 350
Springel V., 2005, MNRAS, 364, 1105
Springel V., 2010, ARA&A, 48, 391
Torres-Flores S., Epinat B., Amram P., Plana H., Mendes de Oliveira C., 2011, MNRAS, 416, 1936
Trujillo-Gomez S., Klypin A., Primack J., Romanowsky A. J., 2011, ApJ, 742, 16
Tully R., Fisher J., 1977, A&A, 54, 661
Valdarnini R., 2012, A&A, 546, A45

APPENDIX A: SPD-BASED SHEAR TENSOR

The expression for the velocity shear tensor can be derived by rewriting the deformation tensor $\partial v_\alpha/\partial r_\beta$ as

$$\frac{\partial v_\alpha}{\partial r_\beta} = \frac{\partial v_\alpha}{\partial r_\beta} + \frac{1}{2}\frac{\partial v_\beta}{\partial r_\alpha} - \frac{1}{2}\frac{\partial v_\beta}{\partial r_\alpha} = \frac{1}{2}\left(\frac{\partial v_\alpha}{\partial r_\beta} + \frac{\partial v_\beta}{\partial r_\alpha}\right) + \frac{1}{2}\left(\frac{\partial v_\alpha}{\partial r_\beta} - \frac{\partial v_\beta}{\partial r_\alpha}\right), \tag{A1}$$

where $\alpha, \beta = x, y, z$. The first, symmetric part is used to define the velocity shear tensor scaled by the Hubble factor as

$$\Sigma_{\alpha\beta} = -\frac{1}{2H_0}\left(\frac{\partial v_\alpha}{\partial r_\beta} + \frac{\partial v_\beta}{\partial r_\alpha}\right). \tag{A2}$$

For a smoothed field using the SPH approach, we have for the ith particle and j neighbours, $\boldsymbol{r}$ is the position vectors so that

$$F_{\rm s}(\boldsymbol{r}_i) \simeq \sum_{j=1}^{N} \frac{m_j}{\rho_j} F_j W(|\boldsymbol{r}_i - \boldsymbol{r}_j|, h_i), \tag{A3}$$

where $h = h_i$ for the 'gather' method and $h = h_j$ for the 'scatter' method. For the smoothed velocity field

$$\boldsymbol{v}_i \simeq \sum_{j=1}^{N} \frac{m_j}{\rho_j} \boldsymbol{v}_j W(|\boldsymbol{r}_i - \boldsymbol{r}_j|, h), \tag{A4}$$

the velocity can also expressed as in equation (11) using $\nabla(\rho\boldsymbol{v})_i = \rho_i(\nabla\boldsymbol{v}_i) + \boldsymbol{v}_i(\nabla\rho_i)$. Applying the gradients, the derivatives only act on the kernel so that

$$\nabla(\rho_i\boldsymbol{v}) \simeq \sum_{j=1}^{N} m_j v_j \nabla W(|\boldsymbol{r}_i - \boldsymbol{r}_j|, h) \tag{A5}$$

here we use the fact that $\rho_i = \sum_{j=1}^{N} m_j W(|\boldsymbol{r}_i - \boldsymbol{r}_j|, h)$. Applying the gradient yields $\nabla\rho_i = \sum_{j=1}^{N} m_j \nabla W(|\boldsymbol{r}_i - \boldsymbol{r}_j|, h)$. By rearranging terms in the chain rule equation and substituting the gradient and divergence terms into the equation and solving for $(\nabla\boldsymbol{v})_i$ one obtains

$$\nabla\boldsymbol{v}_i \simeq \frac{1}{\rho_i}\left[\sum_{j=1}^{N} m_j v_j \nabla W(|\boldsymbol{r}_i - \boldsymbol{r}_j|, h) - v_i \sum_{j=1}^{N} m_j \nabla W(|\boldsymbol{r}_i - \boldsymbol{r}_j|, h)\right] \approx \frac{1}{\rho_i}\sum_{j=1}^{N} m_j (v_j - v_i)\nabla W(|\boldsymbol{r}_i - \boldsymbol{r}_j|, h). \tag{A6}$$

The partial derivatives of one component, say the x-component of the ith particle $v_{x,i}$, of the velocity is given by

$$\frac{\partial v_{x,i}}{\partial x_i} = \frac{1}{\rho_i}\sum_{j=1}^{N} m_j (v_{x,j} - v_{x,i})\frac{\partial}{\partial x_i} W(|\boldsymbol{r}_j - \boldsymbol{r}_i|, h). \tag{A7}$$

Since the kernel is evaluated using $W(|\boldsymbol{r}_i - \boldsymbol{r}_j|, h)$, we let $r = |\boldsymbol{r}_i - \boldsymbol{r}_j| = \sqrt{(x_i - x_j)^2 + (y_i - y_j)^2 + (z_i - z_j)^2}$ and $q = r/h$, then for the x component we have the partial derivatives of the kernel function given by the following expressions. The y and z components follow accordingly. First, we note that

$$\frac{\partial W(r,h)}{\partial x} = \frac{\partial W(r,h)}{\partial r}\frac{\partial r}{\partial x}. \tag{A8}$$

So we may evaluate equation (A7) using equation (A8) to obtain

$$\frac{\partial}{\partial x_i} W(|\boldsymbol{r}_i - \boldsymbol{r}_j|, h) = \begin{cases} \frac{8}{\pi h^5}(18q - 12)(x_i - x_j) & 0 \le q \le \frac{1}{2} \\ -\frac{8}{\pi h^5}\frac{6}{q}(1-q)^2(x_i - x_j) & \frac{1}{2} < q \le 1 \\ 0 & \text{Otherwise} \end{cases}. \tag{A9}$$

This paper has been typeset from a TEX/LATEX file prepared by the author.

5. Halo Clustering in a Lagrangian Cosmic Web

> "The most beautiful thing we can experience is the mysterious. It is the source of all true art and science."
>
> Albert Einstein

5.1. Halo Clustering

The current galaxy formation paradigm suggests galaxies form inside dark matter halos (see Kauffmann et al. 1993; Steinmetz & Navarro 2002, and references within) and that the distribution of galaxies can be understood through how galaxies populate halos as well as the clustering of halos themselves (Springel et al. 2005b). Halo clustering is independent of baryonic physics and allows one to test cosmological models of structure formation. Initial indications that galaxy formation is biased was first given by Kaiser (1984) who suggested, using Abell clusters, that clustering was due to peaks in the primordial Gaussian density distribution. This was later supported by Bardeen et al. (1986), concluding bias prevails under these high peak conditions.

The degree of halo clustering is measured using the spatial *two - point correlation* function (2PCF) (Peebles 1980), which determines the excess probability dP of finding a pair of galaxies with a separation distance $r = |\mathbf{x_1} - \mathbf{x_2}|$, when compared a random distribution. Eq. 30 below gives the mathematical description of the 2PCF $\xi(r)$, where $\bar{n}$ is given as the mean galaxy density and dV_i is the volume element surrounding galaxy $i = 1, 2$.

$$dP = \bar{n}^2[1 + \xi(r)]dV_1 dV_2 \tag{30}$$

If clustering is no different from a random distribution, $\xi(r) = 0$. Any value for which $\xi(r) > 0$ indicates galaxies are more clustered and $\xi(r) < 0$ would suggest galaxies are underclustered, when compared to a random distribution. The 2PCF is related to the power spectrum $P(k)$ by the Fourier transform (Eq. 31) and fully describes the statistical properties of Gaussian random fields (Bardeen et al. 1986).

$$\xi(\mathbf{r}) = \frac{1}{2\pi^2} dk\, k^2 P(k) \frac{sin(kr)}{kr} \tag{31}$$

It has been observed that halo clustering is dependent on both the large scale mass distribution as well as the halo assembly history (Kaiser 1984; Cole & Kaiser 1989; Mo & White 1996; Gao et al. 2005a; Gao & White 2007; Croton et al. 2007; Dalal et al. 2008; Faltenbacher & White 2010). The assembly history incorporates all known properties of the halo such as shape, spin, concentration, merger history and formation time.

Cosmic web type has *also* been shown to vary with the density field as well as the assembly history of halos classified as node, filament, sheet and void halos (Hahn et al. 2007b,a; Aragón-Calvo et al. 2007b; Hoffman et al. 2012; Libeskind et al. 2012b,a, 2014). This leads to the question of whether or not halo clustering is web type dependant, and if so, can halo clustering be explained by the manifestation of the web type properties imposed on halos.

5.2. Section Outline & Credit

In this section, the web type dependence of halo clustering is explored. The chapter is presented as an arxiv preprint paper that *has been submitted* to Monthly Notices of the Royal Astronomical Society. Credit between Faltenbacher and Fisher is assigned as follows. The creative element of the preprint was an idea of Fisher as is the initial work checking the viability of the results. The cross-correlation functions and matter auto-correlation functions were computed using data provided by Fisher and FORTRAN code supplied by Faltenbacher. Finally the drafting of the preprint was the responsibility of Fisher.

Cosmic Web Type Dependence of Halo Clustering

J. D. Fisher*, A. Faltenbacher
Department of Physics, University of Witwatersrand, Braamfontein, 2000, South Africa

Accepted XXX. Received YYY; in original form ZZZ

ABSTRACT
We use the Millennium simulation to show that halo clustering varies significantly with cosmic web type. Halos are classified as node, filament, sheet and void halos based on the eigenvalue decomposition of the velocity shear tensor. This classification allows us to examine the clustering of halos as a function of web type in different mass ranges. We find that node halos show positive bias for all mass ranges probed, even for 10^{11} and $10^{12}\,h^{-1}\mathrm{M}_{\odot}$ mass bins where the clustering of the entire halo sample is anti-biased. In all mass bins filament halos show negligible bias, whereas void and sheet halos are anti-biased. The zero-crossing of the void and sheet correlation functions occur at much smaller scales $\gtrsim 5\,h^{-1}$Mpc when compared to the same correlation functions for the entire halo sample. Our results suggest that the mass dependence of halo clustering is rooted in the composition of web types in the mass bin. The substantial fraction of node type halos for halo masses $\gtrsim 2\times 10^{13}h^{-1}\mathrm{M}_{\odot}$ leads to positive bias. Filament type halos prevail at intermediate masses, $10^{12}-10^{13}h^{-1}\mathrm{M}_{\odot}$, resulting in unbiased clustering. The large contribution of sheet type halos at low halo masses $\lesssim 10^{12}h^{-1}\mathrm{M}_{\odot}$ generates anti-biasing.

Key words: cosmology: dark matter - large-scale structure of Universe – methods: numerical

1 INTRODUCTION

For a long time, N-body simulations have been used to test cosmological theories of clustering evolution and the formation of structure (e.g., Centrella & Melott 1983; Klypin & Shandarin 1983; Davis et al. 1985; Frenk et al. 1988). Comparison of the N-body results to the observed galaxy redshift surveys such as 2dF (Colless et al. 2001) & SDSS (York et al. 2000) has contributed substantially to the present understanding of the clustering behaviour of galaxies.

Galaxy formation and evolution can be understood through two main processes: how galaxies populate dark matter halos and the clustering of halos themselves. The clustering of dark matter halos is thought be largely independent of baryonic physics and can therefore be studied using state-of-the-art N-body simulations. The clustering of halos was initially thought to be dependant on the large scale density fields (Kaiser 1984; Cole & Kaiser 1989; Mo & White 1996). Subsequent studies on the shape, concentration, content, spin and formation time of halos displayed similar mass dependencies (Frenk et al. 1988; Dubinski & Carlberg 1991; Franx et al. 1991; Warren et al. 1992; Cole & Lacey 1996; Bullock 2002; Jing & Suto 2002; Bailin & Steinmetz 2005; Allgood et al. 2006; Bett et al. 2007; Macciò et al. 2008). Both clustering and halo properties exhibit a correlation with the mass of the halo. Therefore, it was a natural progression to confirm the clustering dependence on the aforementioned halo properties (Gao et al. 2005; Harker et al. 2006; Wechsler et al. 2006; Gao & White 2007; Allgood et al. 2006; Bett et al. 2007; Faltenbacher & White 2010). For example: low mass halos tend to be more spherical, as do halos for a given mass formed at a higher redshift; low mass halos that have formed earlier then exhibit a higher degrees of clustering (Gao et al. 2005). However, the problem of identifying the most important properties for halo clustering is problematic. This led to the notion of assembly bias, by incorporating all halo properties into the assembly history allowed for a second parameter to describe clustering (Croton et al. 2007; Gao & White 2007; Hahn et al. 2007a,b; Dalal et al. 2008; Li et al. 2008; Faltenbacher & White 2010). In this analysis we introduce the *cosmic web type of the halo* as sub-dividing criterion for an "assembly bias" study.

The large scale filamentary structure of the Universe, initially described by Bond et al. (1996) as the cosmic web, consists of increasingly dense substructure known as voids, sheets, filaments and nodes. The cosmic web is characterised by the large scale tidal fields induced by these substructures, correlating the properties of dark matter halos residing within them (Bond et al. 1996; Colberg et al. 1999; Kauffmann et al. 1999; Altay et al. 2006; Faltenbacher et al. 2009). Various algorithms now exist to classify the large scale structure of the Universe into its constituent web types (e.g., Aragón-Calvo et al. 2007; Hahn et al. 2007a; Forero-Romero et al. 2009; Aragón-Calvo et al. 2010; Falck et al. 2012; Hoffman et al. 2012). Using the Millennium simulation, we wish to describe the dependence of halo clustering on web type by classifying the cosmic web with the algorithm proposed by Fisher et al. (2016), based on the 'V-Web' algorithm given by Hoffman et al. (2012). Faltenbacher & White (2010) demonstrated that the structure of the velocity field is tightly correlated with the environment

* E-mail: justindavidfisher@gmail.com

and this classification scheme naturally incorporates the dynamics of the velocity field in its definition through the velocities of the neighbouring halos.

The outline of this paper is as follows: we list the simulation methodology and classification procedure in Sec. 2. We then examine the clustering properties of the 2PCF, as well as the mass dependence of this clustering for the different web types in Sec. 3. Finally, we offer some concluding remarks in Sec. 4.

2 METHOD

In this section we give some details about the publicly available Millennium simulation (Lemson & Virgo Consortium 2006) used for this analysis. We decided to use the original Millennium simulation, which is now over 10 years old, for two reasons: 1) our results are generic, i.e. they should not depend on the exact cosmological model; 2) for comparison reasons we wanted our analysis to be as close as possible to the seminal work by Gao et al. (2005). Subsequently, auto and cross-correlation functions are reviewed. Finally, core elements of the Lagrangian web classification algorithm introduced by Fisher et al. (2016) are discussed to the extent needed for the understanding of the analysis.

2.1 Simulation & Halo Sample

The following analysis is based the Millennium simulation (Springel et al. 2005). The first in a series of publicly available, high resolution, cosmological N-body simulations performed within the Millennium Simulation Project (Lemson & Virgo Consortium 2006). A ΛCDM cosmological model is adopted with CDM and baryonic density $\Omega_{dm} = 0.205$ and $\Omega_b = 0.045$ at z=0 respectively. The Hubble parameter is set to $h = 0.73$ ($H_0 = 100\,\mathrm{km\,s^{-1}\,Mpc^{-1}}$). The primordial power spectrum index is n=1 and a normalization value is $\sigma_8 = 0.9$. The evolution of 2160^3 particles in a 500 Mpc/h cube is followed resulting in a mass resolution of $8.6 \times 10^8\,h^{-1}M_\odot$.

To identify the halos, a friends-of-friends (FOF) (Davis et al. 1985) group finder with a linking length b=0.2 is employed and a minimum number limit of 20 particles is imposed. FOF groups are then decomposed into a distinct set of self-bound subhalos using SUBFIND (Springel et al. 2001), the most massive of which is then assigned as the main halo. The current analysis will be restricted to main halos.

2.2 Quantifying Halo Clustering: The Two-Point Correlation Function

The degree of clustering is quantified using the spatial *two - point correlation* function (2PCF) (Peebles 1980). Commonly one distinguishes between two variations of the 2PCF: (i) the *two-point auto-correlation* function which compares counts of pairs of points drawn from the same sample with the counts drawn from a corresponding random sample, while (ii) the *two-point cross-correlation* function compares counts of pairs drawn from a main and a reference sample with the counts from the main and a corresponding random sample. In this paper, we utilise halo samples, defined by mass and web type, as main samples (Q-sample) and an random subset of 10 million simulation particles as reference sample (R-sample). For symmetry reasons, the random sample counts ($\mathscr{R}$-sample) can be determined analytically. We compute the auto correlation function for the R-sample:

$$\xi(r)_{mm} = \frac{RR(r)}{\mathscr{R}\mathscr{R}(r)} - 1 \,, \tag{1}$$

where $RR(r)$ indicates the number of pairs from the reference sample with a spatial separation of r. $\mathscr{R}\mathscr{R}(r)$ is the correspondingly normalised number of counts of pairs drawn from a random sample (computed analytically). The cross correlation is computed for pairs from the Q and the R sample:

$$\xi(r)_{hm} = \frac{QR(r)}{Q\mathscr{R}(r)} - 1 \,, \tag{2}$$

where $QR(r)$ are the counts of mixed pairs drawn from the halo sample (Q) and the reference sample (R). As for the auto correlation function, the correctly normalised counts for the main and the random sample, $Q\mathscr{R}(r)$, can be computed analytically.

We will present the halo-matter cross correlation on distance scales from 0.1 h^{-1}Mpc to 50 h^{-1}Mpc. This range covers two distinct regimes for the mass range of halos analysed here, namely: the one halo term and the two halo term. The one halo term is based on the halo-particle cross pairs within the halo, yielding information about the internal structure of the halos. The two halo term is based on cross halo-particle cross pairs with the particles lying outside the virial radius of the halo and possibly inside the virial radius of a second, distant halo. Halo clustering is usually measured in the linear regime at distances around 10 h^{-1}Mpc.

The comparison of the matter auto-correlation function, $\xi(r)_{mm}$ (Eq. 1), and the halo - matter cross-correlation function, $\xi(r)_{hm}$ (Eq. 2), determines the clustering strength of the halo sample relative to the overall clustering of matter. If the amplitudes of the halo correlation function are larger than that of the mass correlation function, the halo sample is said to show positively biased clustering. The reverse behaviour is referred to as anti-biased halo clustering.

2.3 Cosmic Web Classification Algorithm

Classifying individual halos into web types is done using the Lagrangian classifier given by Fisher et al. (2016). This is accomplished by constructing the velocity shear tensor (see Hoffman et al. 2012) using techniques borrowed from smoothed particle hydrodynamics (SPH) given as:

$$\frac{\partial \mathbf{v}^{\alpha}_{s,i}}{\partial \beta} \simeq \frac{1}{\rho_i} \sum_{j=1}^{N} m_j (\mathbf{v}^{\alpha}_i - \mathbf{v}^{\alpha}_j) \frac{\partial}{\partial \beta} W(|\mathbf{r}_i - \mathbf{r}_j|, h_i) \,. \tag{3}$$

where the Greek indices refer to the coordinate system (x, y, z) and the Latin indices represent the particle labels. m_j is mass of the j^{th} particle[1], $\mathbf{v}$ is the velocity and $W(|\mathbf{r}_i - \mathbf{r}_j|, h_i)$ is the smoothing kernel. We adopt a cubic spline kernel (Monaghan & Lattanzio 1985), given by Springel (2010) as:

$$w(q) = \frac{8}{\pi h^3} \begin{cases} 1 - 6q^2 + 6q^3, & 0 \le q \le \frac{1}{2} \\ 2(1-q)^3, & \frac{1}{2} < q \le 1 \\ 0, & \text{Otherwise} \end{cases} \tag{4}$$

with the kernel dropping to zero at $r = h$. h is known as the smoothing length and is defined as the distance to the furtherest neighbour. The adaptive smoothing length, ensuring exactly 32 neighbours are

[1] In this work, we use the number density instead of the mass density.

accounted for, prevents local density and velocity field sampling errors.

Once Eq. 3 has been constructed, the velocity shear tensor is diagonalised to obtain its eigenvalues which are then sorted. Defining an eigenvalue threshold value λ^{th} allows one to classify the halo web type by counting how many of its eigenvalues are greater than the threshold value. Nodes, filaments, sheets and voids have 3, 2, 1 and 0 eigenvalues greater than the threshold value respectively.

An eigenvalue greater than the threshold value is interpreted as a collapse along its corresponding eigenvector (Hoffman et al. 2012). Expansion along a given eigenvector then occurs when the corresponding eigenvalue is less than the threshold value. Nodes collapse and voids expand along all 3 axes. Sheets collapse along one of its axis and expand along two axes while filaments are observed to collapse along two axes and expand along the third. In this work we adopt a threshold value of zero.

Hoffman et al. (2012) concluded that the threshold value be taken as a free parameter, determined visually as $\lambda^{th} = 0.44$. Fisher et al. (2016), introducing a Lagrangian approach for the determination of the velocity shear tensor, showed that adding the Hubble flow to the peculiar velocity field (Hoffman's analysis is based on the peculiar velocity field) allows one to set $\lambda^{th} = 0$. Zero seems to be the most natural discriminator between contraction ($\lambda^{th} > 0$) and expansion ($\lambda^{th} < 0$) along the eigenvectors of the velocity shear tensor.

2.4 Hubble Flow

One subtle aspect of the classification algorithm that needs clarification is the in/exclusion of the Hubble flow. It was shown in Fisher et al. (2016) that the inclusion of the Hubble flow prevents contamination of the classification scheme by the artificial shrinking of virialised structures. Therefore, inclusion of the Hubble flow is particularly important if the classification scheme allows for one to include dynamical information from within virialised structures. This is the case if simulation particles or subhalo populations (i.e. not only main halos) are employed for sampling the velocity field.

If the velocity field is sampled by main halos only, the dynamics within the virialised regions do not contribute to the classification scheme. In this case the inclusion of the Hubble flow may not be necessary. On the contrary, the restriction of the sample to main halos causes sph-kernels to extend to rather large distances where the Hubble expansion begins to dominate. The expansion measured this way is not a result of the local gravitational field. Therefore, the current analysis is based on the peculiar velocity field *without Hubble flow* as we use main halos only to sample the velocity field.

The utilisation of peculiar velocities in combination with the sampling of the velocity field over relatively large distances allows the threshold value for the classification, defining collapse or expansion, set to $\lambda^{th} = 0$. A zero threshold value permits a natural interpretation as positive and negative eigenvalues correspond to collapse and expansion respectively.

3 RESULTS & DISCUSSION

The results reported here are based on the main halo sample with top-hat masses above $9 \times 10^{10}\, h^{-1}\mathrm{M}_{\odot}$. The peculiar velocities of the these halos are used to sample the large scale velocity field and to determine the velocity shear tensor at the halos' location. According to the number of positive and negative eigenvalues, the halos are classified as node, filament, sheet and void halos. In the first part of this section we discuss the overall number statistics of the various halo types. The second part compares the matter cross-correlation functions of halo samples for the different cosmic web types. Finally, we present the mass dependence of the clustering of halos for a given web type. Therefore, the clustering behaviour is investigated for halos in narrow mass bins (same as used in Gao et al. 2005)

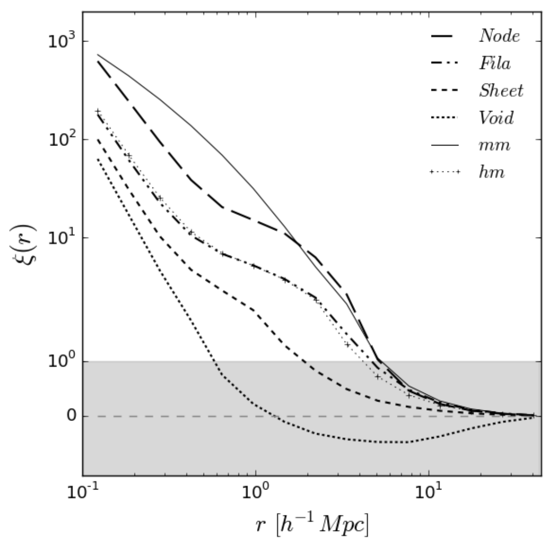

Figure 1. The halo-matter cross-correlation function per web type compared to the matter auto-correlation function (solid line) and the halo-matter cross-correlation for the entire halo sample (thin dotted line with '+' markers). All halos with top-hat masses $\geq 9 \times 10^{10}\, h^{-1}\mathrm{M}_{\odot}$ are included. The matter distribution is sampled by a subset of 10 Million randomly selected simulation particles. Note: the y-scale is logarithmic for $\xi > 1$ and linear for $\xi < 1$ indicated by the shaded region. The dashed gray line indicates $\xi = 0$. A value of $\xi < 0$ indicates less clustering than the random sample. Nodes (large dashes), filaments (dash-dot), sheets (small dashes) and voids (dotted) exhibit very different clustering behaviour. The effect is largely tiered, with the web types of higher infall dimensionality demonstrating significantly more clustering. Voids are under-clustered at larger scales.

3.1 Classification results

The web type number fractions for the classification of the Millennium main halo sample, including all main halos with top-hat masses $\geq 9 \times 10^{10}\, h^{-1}\mathrm{M}_{\odot}$, are: 8.76% node, 62.38% filament, 28.14% sheet and 0.72% void halos. The statistics indicate a skewness towards web types with a larger number of positive eigenvalues of the velocity shear tensor. It is self evident that environments of higher infall dimensionality are more conducive to the formation of halos. One does not expect to find many halos in void regions as shear forces are causing an expansion along all 3 dimensions. On the other hand, the relatively small number of node halos may indicate that only a small volume fraction of the universe shows infall along all three dimensions. It can be concluded that filament halos constitute the largest subset of halos in the mass range considered here.

3.2 Halo clustering dependence on web type

Fig. 1 shows the two point cross and auto-correlation functions for the halo and the overall matter distributions, respectively. The matter distribution is sampled by a subset of 10 Million randomly selected simulation particles. The classification is based on the velocity field sampled by all main halos with masses $\geq 9\times10^{10}\,h^{-1}\mathrm{M}_{\odot}$. We use a linear scale below $\xi = 1$ to show any under-clustering that may be present. The level of clustering varies significantly with web type as the cross-correlation functions are staggered according to the infall dimensionality of the web type.

The halo-matter cross correlation functions are computed for distances from $100\,h^{-1}$kpc to $50\,h^{-1}$Mpc. This allows one to sample the one halo term (inside the virial radius of the main halos) and the two halo term (outside the virial radius) for all halo masses considered here. The tiered behaviour observed on small scales $\lesssim 1\,h^{-1}$Mpc reveals a size and mass segregation of the halos corresponding to web type. Void halos are preferentially found among the smallest, least massive halos in the entire sample. The opposite holds for node halos which occupy the largest and most massive halo ranges. Filament and sheet halos occupy the intermediate mass and size ranges.

The staggered arrangement observed for the two halo term at distances $\gtrsim 1\,h^{-1}$Mpc is a seamless continuation of the behaviour on small scales. Halos residing in low infall dimensionality web types exhibit large anti-bias with respect to the matter auto-correlation function. Void halos are shown to be the least clustered web type, the degree of clustering observed to be less than a random distribution (i.e. $\xi(r)_{void} < 0$ for $r > 1\,h^{-1}Mpc$). The dashed horizontal line allows one to easily read off the zero-crossing scales. The anti-bias largely decreases for filaments and nodes on larger scales. This behaviour is to be expected as clustering has been shown to depend on the halo mass with higher mass halos showing stronger clustering.

The thin dotted line with the '+' markers in Fig. 1 shows the halo-matter cross-correlation function for the entire halo sample. The similarity to the filament halo cross-correlation function is obvious. It is caused by the dominant fraction of filament type halos in the halo sample (62.38%). The entire halo sample shows a marginal anti-bias which is a result of the mass distribution within the entire sample, i.e. in numbers the anti-biased halos at the lower end of the mass range dominate over the strongly biased halos at the high mass end.

The tiered behaviour of the halo-matter cross-correlation functions on all scales indicates that halos residing in web types with the highest infall dimensionality are usually found in higher density environments. Similarly, low infall dimensionality corresponds to low density regions. Thus, as expected, there is a direct correlation between infall dimensionality and density of the environment. It is, however, the working hypothesis of this analysis that the velocity shear tensor analysis is capable of dissolving degeneracies inherent in the determination of cosmic web type based on density criteria alone.

So far the sampling of the velocity field, and ultimately the computation of the eigenvalues of the velocity shear tensor, is based on the entire halo sample, comprised of all main halos $\geq 9\times10^{10}\,h^{-1}\mathrm{M}_{\odot}$ in the simulation box. The determination of the velocity gradient uses the 32 nearest neighbour main halos. The most massive halos in the simulation show masses above $10^{15}\,h^{-1}M_{\odot}$. It is expected that they are surrounded by a plethora of low mass halos with a few times $10^{11}\,h^{-1}\mathrm{M}_{\odot}$. Thus, the velocity shear tensor associated with high mass halos may frequently be based on a set of low mass halos a factor of 10^4 less massive than the main halo, close to the virial radius.

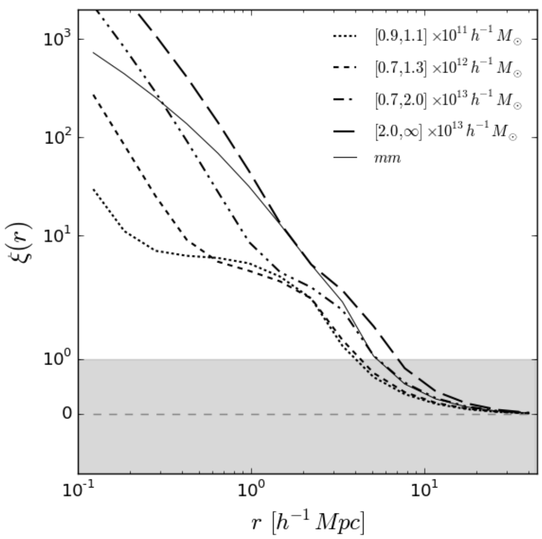

Figure 2. The cross-correlation functions for halos in each mass bin and the matter auto-correlation function. Higher mass halos are more strongly correlated relative to low mass halos and halos above the characteristic mass M_* tend to be more bias while less massive halos exhibit more anti-bias.

These regions are know to be contaminated by backsplash halos, i.e. halos which have been part of the main halo before being ejected (e.g., Moore et al. 2004; Warnick et al. 2008). To check the effect of the backsplash halos we have computed the shear tensor excluding neighbour halos within two times the virial radius and obtained very similar results, with the encouraging exception that the very high mass void halos disappear. In the following section, which presents the main results, we only use narrow mass bins for the sampling of the velocity field and calculation of the velocity shear tensor (the same mass bins used for the computation of the correlation functions). We do not investigate the impact of backsplash halos any further. The impact of backsplash halos for the narrow mass bin samples should be negligible as the backsplash halos usually are orders of magnitude less massive than the main halos.

3.3 Mass Dependence of Web Type Clustering

Akin to the work in Gao et al. (2005), we examine the mass dependence of halo clustering in four narrow mass bins to accurately observe the bias. The sampling of the velocity field and consequently the determination of the cosmic web type is confined to halos in the same mass bin. For the highest mass bin the velocity shear tensor is computed based on halos more massive than $2\times10^{13}\,h^{-1}\mathrm{M}_{\odot}$ resulting in an average distance to the 32nd neighbour of $35\,h^{-1}$Mpc. To a certain extent, this takes the different sizes of the halos into account but results in a small fraction, 0.3%, of void halos in the highest mass bin. Therefore, we also have used the entire halo sample to compute the web types of halos in the various mass bins and find qualitative agreement despite the contamination by backsplash halos (see discussion above). Since the former approach determines web type and clustering based on the same halo sample we have decided to present the results of this, more consistent approach.

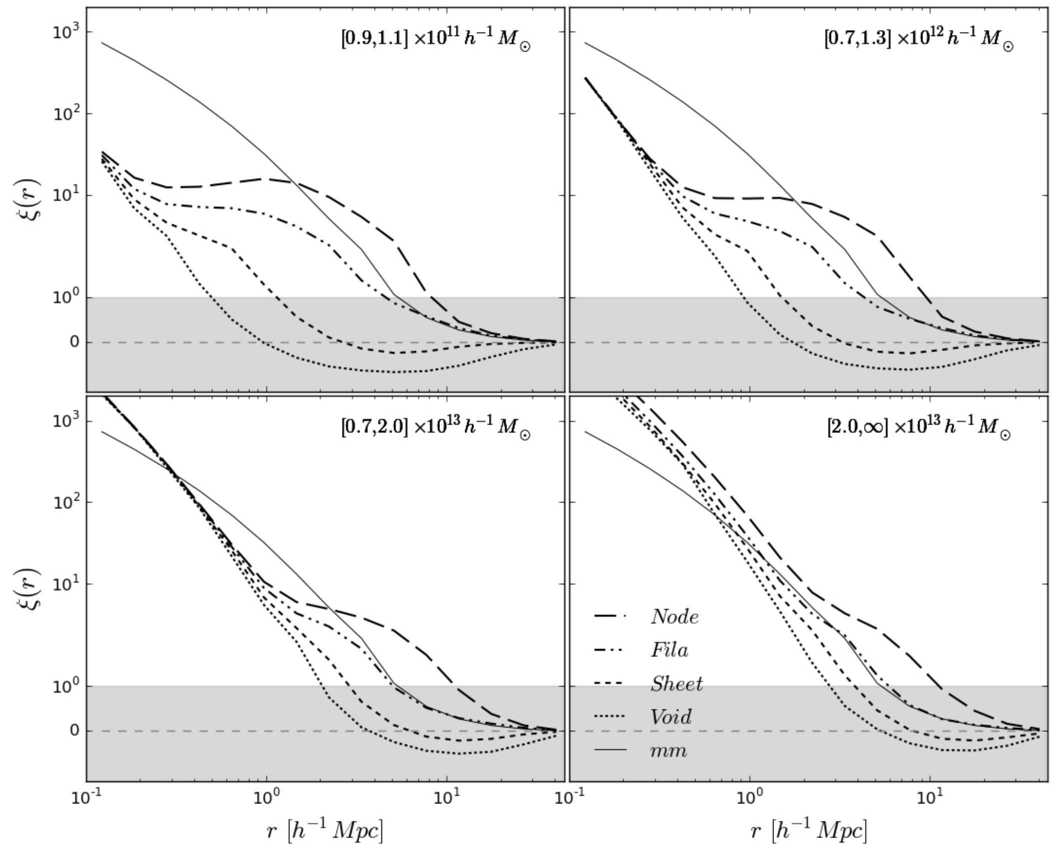

Figure 3. The halo correlation function per web type and the matter autocorrelation function in four increasing mass bins. Clustering is seen to vary significantly with web type for all mass bins. Low mass halos differ considerably in size, density and exhibit a large anti-bias on smaller scales. For all masses at large radii, void and sheet halos are under-clustered and node halos are consistently bias.

Fig. 2 shows the halo-mass cross-correlation functions for all halos in the indicated mass bins, again on linear scales for $\xi(r) \leq 1$. As expected, clustering increases with mass. The correlation functions are tiered. Gao et al. (2005) defines the characteristic mass $M_* = 6.15 \times 10^{12} M_\odot$ as the bias anti-bias limit. In the lower mass bins, less than the characteristic mass, a anti-bias, measured at scales from 5 to $20\,h^{-1}$Mpc, can be observed. Conversely, the highest mass bin is defined greater than M_* and one observes a large bias factor. Halos in the second highest bin have masses most similar to M_* and they display very little bias on the two halo term scales.

In Fig. 3, we calculate the web type clustering per mass bin. All panels of Fig. 3 display the same behaviour as in Fig. 1 whereby the web type cross-correlation functions are tiered by web type. At small scales, the halo-matter cross-correlation function measures the average density profiles of the halo sample and it can be seen that the profiles converge independent of web type. The deviation seen in the highest mass bin is a result of the large mass range covered by this mass bin, which causes a behaviour reminiscent of Fig. 1 where the correlation function for the entire mass range is displayed.

Arguably the most striking feature in Fig. 3 is the similarity of the correlation functions for a given web type independent of mass. In all four mass bins the node halos are strongly biased at scales $\gtrsim 5\,h^{-1}$Mpc, the filament halos seem to follow the matter autocorrelation function closely and sheet and void halos are strongly anti-biased with the zero-crossing occurring at much smaller scales, when compared to the entire halo sample. The exact scale of the zero-crossing seems to be influenced by the average halos radius in the specific sample but the negative amplitudes are very similar for a given web type independent of mass.

On larger scales, the clustering of low mass halos ($\lesssim 10^{13} M_\odot$) has been shown to depend substantially on halo formation time (Gao et al. 2005), that is, less massive halos formed at higher redshifts have lower concentrations, more substructure and a higher degree of clustering (Gao & White 2007). The top panels of Fig 1 would then suggest highly clustered node halos formed first, followed by filaments, sheets and nodes. This is in agreement with the results found in Harker et al. (2006); Hahn et al. (2007a,b) and may follow from the hierarchical structure formation paradigm: as primordial over-densities begin to collapse at higher redshifts they will form halos earlier on and will continue to attract objects (particles and halos) throughout the halo evolution. It may then also be inferred by the relatively poor clustering of void halos that these halos formed at later times.

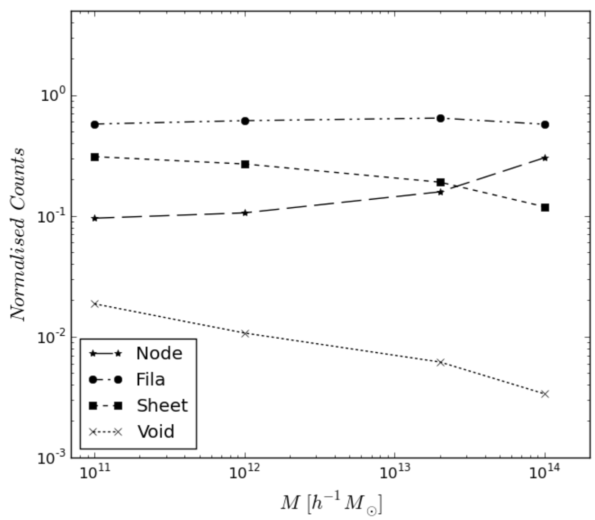

Figure 4. Normalised halo web type fractions as a function of the four mass bins. Lines have been added to guide the eye. The highest mass bin has an infinite upper limit so the abscissa values for these points are chosen arbitrarily. Filament halos dominate for all halo masses with a relatively high contribution of sheet halos at lower masses. For the highest mass bin, node halos account for a substantial fraction of the overall halos. Void halos do not contribute more than 1% at any mass bin.

3.4 Dependence of Web Type Fractions on Mass

The above analysis has revealed that same mass halos show different clustering behaviour depending on their web type. In order to gain insight into the mass dependence of the bias for the entire halo sample, as seen in Fig. 2, we now investigate which web types are responsible for the overall clustering per mass bin.

Fig. 4 illustrates the web type fractions per mass bin (for visual impression, the last bin mass value is set to 10^{14}, otherwise plotted using the midpoint of the respective bin). The fraction of halo web types is largely mass dependant. Node halo fractions are monotonically increasing with mass so that in the highest mass bin they account for the second largest fraction of all halos, followed by sheets and voids. Filaments are dominant in all mass bins. In the low mass regime, filament halos are seen to occupy the largest fraction of halos followed by sheet halos. Sheet and void fractions decrease with mass, the latter being less than 1% for all mass bins.

Fig.4 suggests that filaments and sheets determine the overall clustering in the lower mass ranges ($\sim 10^{11}$ to $\sim 10^{12}\,h^{-1}\mathrm{M}_\odot$) causing anti-bias. For intermediate mass ranges ($\sim 10^{12}$ to $\sim 10^{13}\,h^{-1}\mathrm{M}_\odot$), filament halos dominate which results in marginal bias. Finally, the substantial fraction of node halos along with filament halos in the high mass ranges ($\gtrsim 5\times10^{14}\,h^{-1}\mathrm{M}_\odot$) generates positively biased halo clustering.

4 CONCLUSIONS

We have employed main halos, with top-hat masses $\geq 9\times10^{10}\,h^{-1}\mathrm{M}_\odot$, to sample the cosmic velocity field and compute the velocity shear tensor. Based on the infall dimensionality (i.e. the number of positive eigenvalues , indicative of infall, for the associated velocity shear tensor) halos are classified into cosmic web types, namely node, filament, sheet and void halos. With the classification scheme in place, the clustering of different web type halos can be analysed.

Our main findings are summarised here:

1) The overall number fractions are: 8.76% node, 62.38% filament, 28.14% sheet and 0.72% void halos. The expansion in all three directions inhibits the formation of void halos. Node halos are rare because a converging velocity field may be restricted to very small volumes. Filament and sheets occupy a relatively large cosmic volume and can provide sufficient matter supply to host a large number of halos.

2) The halo-matter cross-correlation functions for different web types show tiered behaviour on all distance scales probed (0.1 - 50 h^{-1} Mpc). There is a direct correlation between infall dimensionality and density of the environment, i.e. on average nodes, filaments, sheet and void halos live in environments with decreasing density. However, it is expected that the velocity shear tensor allows for a more unique determination of the web type as compared to classification schemes based on the environmental density alone.

3) The halo-matter cross-correlation functions for different web types computed in narrow mass bins: $\sim 10^{11}$; $\sim 10^{12}$; $\sim 10^{13}$ and $> 2\times10^{11}\,h^{-1}\mathrm{M}_\odot$ reveals strong differences in the bias of the considered halo sub-sample. Node halos in all mass bins show positive bias. Filament halos in all mass bins display marginal bias on scales from 5 to 50 h^{-1} Mpc. Sheet and void halos are anti-biased in all mass bins. The clustering behaviour of the different web types seems almost independent of mass.

4) Inspired by the findings reported under point 3, we determined the number fraction of halos of a given web type per mass bin in order to understand the structure of the clustering for the entire halo sample. We find that filament and sheet halos dominate at the low mass range ($10^{11}-10^{12}\,h^{-1}\mathrm{M}_\odot$) causing a marginal anti-bias of the entire halo sample. In the mass range $10^{12}-10^{13}\,h^{-1}\mathrm{M}_\odot$ the contribution of sheet halos decreases and node halos become more frequent. This is reflected in the diminishing bias of the halo clustering in this mass range. Finally, for halo mass above few times $10^{13}\,h^{-1}\mathrm{M}_\odot$ node and filament halos prevail causing positive bias of the overall halo sample.

In conclusion, the isolated clustering analysis of halos for a given web type provides general insight into halo clustering behaviour. At the same time it builds confidence in the Lagrangian classification scheme which has been introduced recently in our foregoing paper. Further analysis into the evolution of halo bias with this approach may prove interesting and is left for future publications.

ACKNOWLEDGEMENTS

The authors acknowledge the use of data from the publicly available Millennium Simulation (http://www.mpa-garching.mpg.de/millennium), carried out by the Virgo Consortium. We would also like to acknowledge the support from the National Astrophysics and Space Science programme (NASSP).

REFERENCES

Allgood B., Flores R. a., Primack J. R., Kravtsov a. V., Wechsler R. H., Faltenbacher A., Bullock J. S., 2006, Monthly Notices of the Royal Astronomical Society, 367, 1781

Altay G., Colberg J. M., Croft R. a. C., 2006, Monthly Notices of the Royal Astronomical Society, 370, 1422

Aragón-Calvo M. A., Jones B. J. T., van de Weygaert R., van der Hulst J. M., 2007, Astronomy and Astrophysics, 474, 315

Aragón-Calvo M. a., Platen E., van de Weygaert R., Szalay A. S., 2010, The Astrophysical Journal, 723, 364

Bailin J., Steinmetz M., 2005, The Astrophysical Journal, 627, 647

Bett P., Eke V., Frenk C. S., Jenkins A., Helly J., Navarro J., 2007, Monthly Notices of the Royal Astronomical Society, 376, 215

Bond J. R., Kofman L., Pogosyan D., 1996, Nature, 380, 603

Bullock J., 2002, The shapes of galaxies and their dark halos : Yale Cosmology Workshop : New Haven, Connecticut, USA, 28-30 May 2001

Centrella J., Melott A. L., 1983, Nature, 305, 196

Colberg J. M., White S. D. M., Jenkins A., Pearce F. R., 1999, Monthly Notices of the Royal Astronomical Society, 308, 593

Cole S., Kaiser N., 1989, Monthly Notices of the Royal Astronomical Society, 237, 1127

Cole S., Lacey C., 1996, Monthly Notices of the Royal Astronomical Society, 281, 716

Colless M., et al., 2001, Monthly Notices of the Royal Astronomical Society, 328, 1039

Croton D. J., Gao L., White S. D. M., 2007, Monthly Notices of the Royal Astronomical Society, 374, 1303

Dalal N., White M., Bond J. R., Shirokov A., 2008, The Astrophysical Journal, 687, 12

Davis M., Efstathiou G., Frenk C. S., White S. D. M., 1985, The Astrophysical Journal, 292, 371

Dubinski J., Carlberg R. G., 1991, The Astrophysical Journal, 378, 496

Falck B. L., Neyrinck M. C., Szalay A. S., 2012, The Astrophysical Journal, 754, 126

Faltenbacher A., White S. D. M., 2010, The Astrophysical Journal, 708, 469

Faltenbacher A., Li C., White S. D. M., Jing Y.-P., Mao S., Wang J., 2009, Research in Astronomy and Astrophysics, 9, 41

Fisher J. D., Faltenbacher A., Johnson M., 2016, Monthly Notices of the Royal Astronomical Society, p. stw370

Forero-Romero J. E., Hoffman Y., Gottlöber S., Klypin A., Yepes G., 2009, Monthly Notices of the Royal Astronomical Society, 396, 1815

Franx M., Illingworth G., de Zeeuw T., 1991, The Astrophysical Journal, 383, 112

Frenk C. S., White S. D. M., Davis M., Efstathiou G., 1988, The Astrophysical Journal, 327, 507

Gao L., White S. D. M., 2007, Monthly Notices of the Royal Astronomical Society: Letters, 377, L5

Gao L., Springel V., White S. D. M., 2005, Monthly Notices of the Royal Astronomical Society: Letters, 363, L66

Hahn O., Porciani C., Carollo C. M., Dekel A., 2007a, Monthly Notices of the Royal Astronomical Society, 375, 489

Hahn O., Carollo C. M., Porciani C., Dekel A., 2007b, Monthly Notices of the Royal Astronomical Society, 381, 41

Harker G., Cole S., Helly J., Frenk C., Jenkins a., 2006, Monthly Notices of the Royal Astronomical Society, 367, 1039

Hoffman Y., Metuki O., Yepes G., Gottlöber S., Forero-Romero J. E., Libeskind N. I., Knebe A., 2012, Monthly Notices of the Royal Astronomical Society, 425, 2049

Jing Y. P., Suto Y., 2002, The Astrophysical Journal, 574, 538

Kaiser N., 1984, The Astrophysical Journal, 284, L9

Kauffmann G., Colberg J. M., Diaferio a., White S. D. M., 1999, Monthly Notices of the Royal Astronomical Society, 303, 188

Klypin A. A., Shandarin S. F., 1983, Monthly Notices of the Royal Astronomical Society, 204, 891

Lemson G., Virgo Consortium t., 2006, ArXiv Astrophysics e-prints,

Li Y., Mo H. J., Gao L., 2008, Monthly Notices of the Royal Astronomical Society, 389, 1419

Macciò A. V., Dutton A. a., van den Bosch F. C., 2008, Monthly Notices of the Royal Astronomical Society, 391, 1940

Mo H. J., White S. D. M., 1996, Monthly Notices of the Royal Astronomical Society, 282, 347

Monaghan J. J., Lattanzio J., 1985, Astronomy and Astrophysics, 149, 135

Moore B., Diemand J., Stadel J., 2004, in Diaferio A., ed., IAU Colloq. 195: Outskirts of Galaxy Clusters: Intense Life in the Suburbs. pp 513–518 (`arXiv:astro-ph/0406615`), doi:10.1017/S1743921304001127

Peebles P. J. E., 1980, The large-scale structure of the universe. Princeton University Press, Princeton, N.J.

Springel V., 2010, Annual Review of Astronomy and Astrophysics, 48, 391

Springel V., White S. D. M., Tormen G., Kauffmann G., 2001, Monthly Notices of the Royal Astronomical Society, 328, 726

Springel V., et al., 2005, Nature, 435, 629

Warnick K., Knebe A., Power C., 2008, MNRAS, 385, 1859

Warren M. S., Quinn P. J., Salmon J. K., Zurek W. H., 1992, The Astrophysical Journal, 399, 405

Wechsler R. H., Zentner A. R., Bullock J. S., Kravtsov A. V., Allgood B., 2006, The Astrophysical Journal, 652, 71

York D. G., et al., 2000, The Astronomical Journal, 120, 1579

This paper has been typeset from a TEX/LATEX file prepared by the author.

6. Future Work and Outlook: Properties of Halos in a Lagrangian Cosmic Web

> "In first place we must observe that the universe is spherical. This is either because that figure is the most perfect, as not being articulated, but whole and complete in itself; or because it is the most capacious and therefore best suited for that which is to contain and preserve all things."
>
> Nicolaus Copernicus

The first studies on the formation of dark matter halos using simulation data began with (Frenk et al. 1988). It was found that halo evolution is largely governed by the merger history of halos. Halos on galactic scales were shown to only have formed after $z \sim 3$ and the central regions of dark matter halos exhibited a constant circular velocity - as observed in spiral galaxies.

The shapes of halos are thought to be maintained by the halos' velocity dispersion (Warren et al. 1992) and have been shown to be flat and triaxial, with a slightly larger fraction of halos more prolate than oblate (Frenk et al. 1988; Dubinski & Carlberg 1991; Cole & Lacey 1996). A thorough investigation into the dependence of the sphericity of halos on mass and redshift is given by Bullock (2002). These results concluded that low mass halos are more spherical than high mass halos and, for a given mass, halos are more spherical at low redshifts.

An examination of halo properties under the Lagrangian classification scheme proposed in Chapter 4 is undertaken. An analysis of the shapes of halo web types can be found in Subsection 6.3, following which the fractional anisotropy of the velocity shear is presented in Subsection 6.4. Finally, the web type correlation with halo spin is given in Subsection 6.5. The analysis is done per web type in an attempt to understand how halo properties are correlated with the environment. This work sets the scene for future study.

6.1. Outlook

In Chapter 5, it has been shown that halo clustering varies with web type so that the mass dependence of halo clustering can be explained by the fraction of web types found at a given mass. The ultimate aim of this section is to explore three halo properties that are included in the halo assembly model with a view to investigating whether any web type assembly history correlations exist. If conclusive, this may suggest halo clustering can be explained entirely by the properties of the halo environment within the cosmic web.

6.2. Method

The method followed in this section uses the same Gadget-2 simulation and Rockstar halo finder as in Section 4. The Lagrangian velocity shear tensor is computed using main halos only, 32 neighbours and no Hubble flow. However, as in Section 5, the threshold value is set to zero since only main halos are used to sample the velocity field. The classification is performed at z=0. All halo parameters (spin, shape, angular momentum etc), unless otherwise indicated, are given straight forwardly from the output of the Rockstar Halo Finder (Behroozi et al. 2013).

6.3. Halo Sphericity and Triaxality

Triaxial halo shapes can be classified in the family of Ellipsoids characterised by their 3 axes: (a, b, c) and are generally expressed using the following ratios: $s = c/a$ - commonly referred to as sphericity, $p = c/b$ and $q = b/a$ (Allgood et al. 2006). s, p and q can fully describe the three main classes of ellipsoids given by Allgood et al. (2006) as:

- Prolate: $a > b \approx c \rightarrow s \approx q < p$ (Sausage shaped)
- Oblate: $a \approx b > c \rightarrow s \approx p < q$ (Pancake shaped)
- Triaxial: $a > b > c \rightarrow s < q < 1$

One also observes the special case of the sphere where $a = b = c$. Spherical, oblate and prolate shaped halos can be seen in the left, middle and right panels of Fig. 21 respectively. The halos are modelled by constructing and diagonalising the inertia tensor (Eq. 32) as the orientation of the halo (at position $\mathbf{x}$) can be expressed using the eigenvectors $(\mathbf{a}, \mathbf{b}, \mathbf{c})$ and eigenvalues of the inertia tensor, corresponding to the 3 axes $(\sqrt{|\mathbf{a}|}, \sqrt{|\mathbf{b}|}, \sqrt{|\mathbf{c}|}) = (a, b, c)$ (Bullock 2002; Allgood et al. 2006).

$$\mathcal{I}_{ij} = \sum_n x_{i,n} x_{j,n} \tag{32}$$

In the calculation of the halo inertia tensor seen in Eq. 32, $x_{i,n}$ is the ith coordinate of the nth DM particle within the given halo.

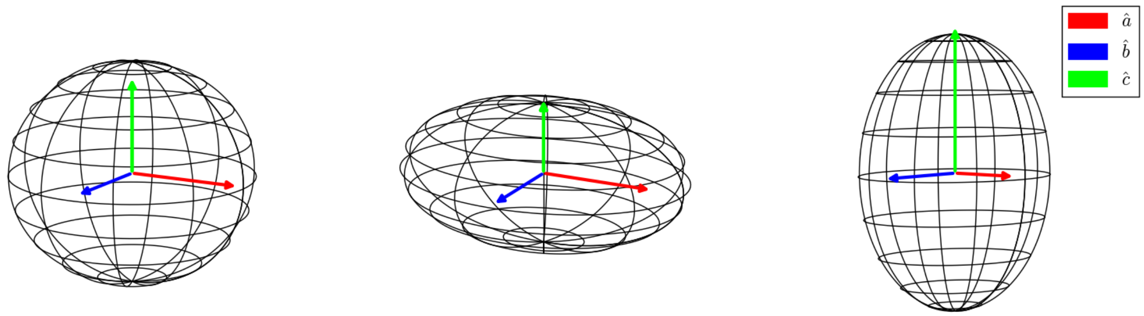

Fig. 21.— Spherical (left), oblate (middle) and prolate (right) shaped halos governed by their principal axes (a, b, c)

Franx et al. (1991) classified halos into the 3 families of ellipsoids by defining the triaxality parameter (Eq. 33).

$$T = \frac{1 - q^2}{1 - s^2} \tag{33}$$

$0 \leq T < 1/3$ suggests the halo is oblate in shape, $1/3 \leq T < 2/3$ indicates a triaxial shape while $2/3 \leq T \leq 1$ suggests the halo is in fact prolate (Allgood et al. 2006). Fig. 22 shows the mean sphericity and triaxality distribution for nodes, sheets, filaments and voids as a function of mass. Results are shown for every mass bin that has a halo count greater than ten. The results are consistent with Allgood et al. (2006); Bett et al. (2007) and Hahn et al. (2007b). Higher mass halos are less spherical and tend towards prolate shapes. The sphericity fit given for all halos by Allgood et al. (2006) as $< s > (M_{vir}, z = 0) = \alpha(M_{vir}/M_*)^\beta$, where $\alpha = 0.54$ and $\beta = -0.05$, is shown by the black dashed line.

Void halos are less massive and posses low sphericities relative to other web types. One observes, in the low mass regime, higher density web types are more spherical, however, after crossing the characteristic mass limit $M_* \approx 6 \times 10^{12}\, h^{-1} M_\odot$ (Gao et al. 2005a) the relation is reversed. In the high mass regime, lower density web types become more spherical. Node and filament halos occupy a higher proportion of high mass halos per bin and, as the sphericity is mass dependent, one finds higher density web type halos exhibit less sphericity by virtue of their mass.

A similar result is found for the triaxality of the halos. At low masses, halos that have a higher infall dimensionality (see Section 5) such as nodes and filaments are less triaxial in shape and more oblate relative to the other web types. Between $10^{12} h^{-1} M_\odot \lesssim M_{vir} \lesssim 10^{13} h^{-1} M_\odot$ one finds that higher density web types become more triaxial tending towards prolate shapes while sheets remain relatively triaxial at higher masses.

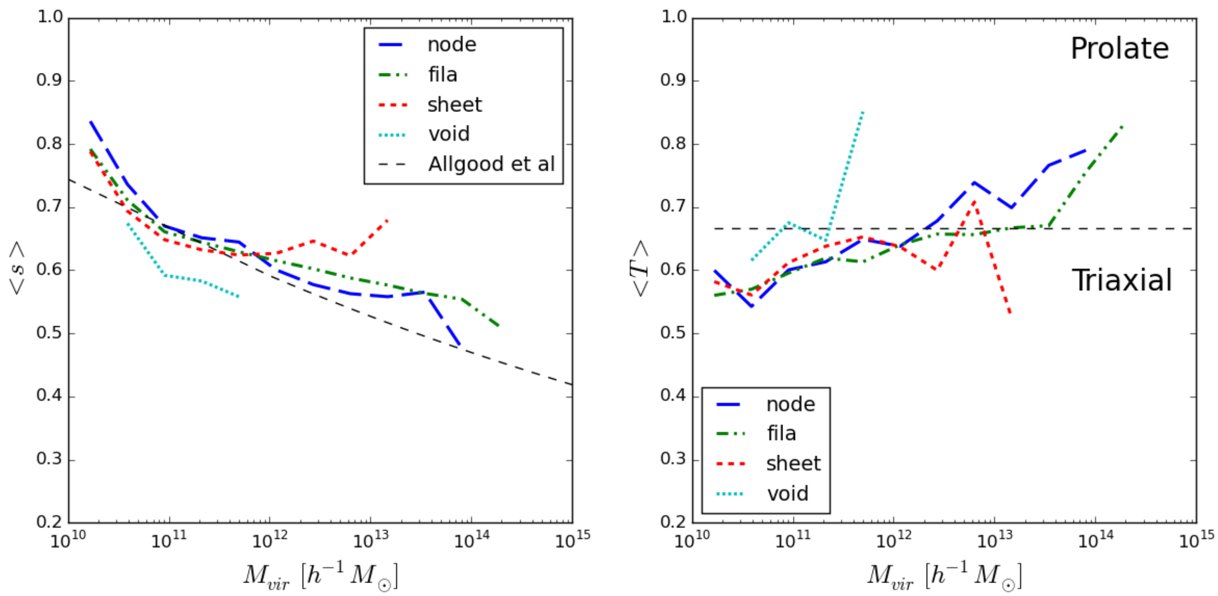

Fig. 22.— Mean sphericity (left) and triaxality (right) for nodes (large blue dashes), filaments (green - dash dot), sheets (red - dashed) and voids (cyan - dotted)

6.4. Fractional Anisotropy

A novel idea borrowed from the field of brain imaging is the fractional anisotropy (FA), which describes the diffusion anisotropy of a given process (Basser & Pierpaoli 1996). FA was later adopted by Libeskind et al. (2012a) to describe the degree of shear anisotropy for a given halo. The classification scheme relies on constructing the velocity shear tensor and obtaining the eigenvalues which then describe a collapse or expansion along a given axis. The FA of the shear tensor describes the uniformity of the expansion or collapse for a given halo (Libeskind et al. 2012a). FA is given by Eq. 34 and is bounded between 0 and 1. A FA value of 1 indicates the expansion or collapse is largely anisotropic while an FA of zero indicates a completely isotropic process.

$$FA = \frac{1}{\sqrt{3}}\sqrt{\frac{(\lambda_1-\lambda_2)^2+(\lambda_1-\lambda_3)^2+(\lambda_2-\lambda_3)^2}{\lambda_1^2+\lambda_2^2+\lambda_3^2}} \tag{34}$$

The fractional anisotropy distribution for the different web types is shown in Fig. 23. As mentioned in Section 4, nodes collapse ($\lambda_i > \lambda^{th}\,\forall i = 1,2,3$) and voids expand ($\lambda^{th} > \lambda_i\,\forall i = 1,2,3$) along all three axes. Also, it was suggested, by the symmetry of the λ_1 and λ_3 halo eigenvalue PDFs, that expansion and collapse appear to be the same process, just in reverse. This is confirmed in Fig. 23. FA values for node and void halos appear to be distributed similarly over a lower FA range indicating collapse and expansion is more isotropic. These results are in contrast with Libeskind et al. (2012a), who, using Eulerian techniques, suggested that collapse and expansion are different processes. Libeskind et al. (2012a) found that while node halos experience largely isotropic collapse, void halos undergo significant anisotropic expansion.

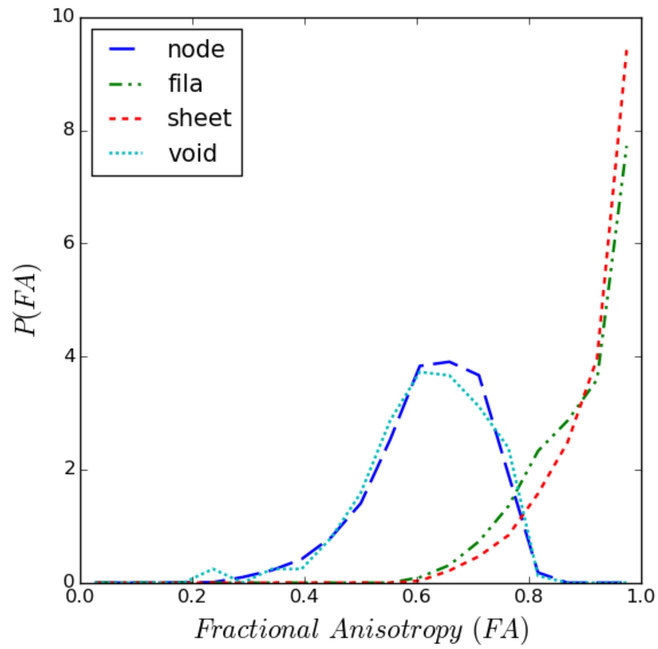

Fig. 23.— The fractional anisotropy for the different web types. Colours and linestyles are as in Fig 22. Nodes and voids exhibit significant isotropic collapse and expansion respectively, possessing similar FA distributions. Sheets and filaments expand and collapse along their respective axes very anisotropically. These findings suggest the expansion process experienced by voids is just the reversed process of collapse by nodes.

Fig. 23 demonstrates sheets and filaments are the most anisotropic halos. This is intuitive as these web types are very unstable. Filaments expand along 1 axis and collapse along 2 axes while sheets expand along 2 axes, collapsing along the third. Eulerian based techniques describe the FA filament probability density more uniformly across the entire FA range while the distribution of sheet halos is moderately anisotropic (Libeskind et al. 2012a).

The mass dependence of shear FA can be found in Fig. 24. The median FA for each web type is shown for all mass bins that have a halo count greater than ten. The error bars show a 1σ deviation from the median. Per web type, FA values for low mass halos are observed to

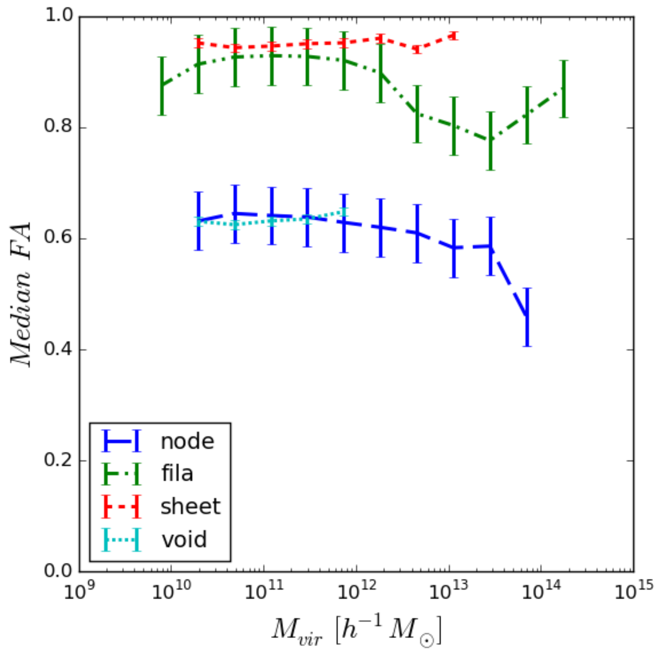

Fig. 24.— Median FA values as a function of mass for all web types. For low mass halos, a weak mass dependence is found. For more massive halos, filament halos have higher median FA values suggesting a more anisotropic shear. High mass node halos experience a more isotropic collapse.

show little mass dependence as is indicated by the constant FA for all web types. Nodes and voids exhibit similar FA values throughout the void mass range. In the high mass regime, the shear for filament halos is more anisotropic as indicated by the increasing median FA values. Node halos exhibit decreasing FA values at higher masses, suggesting a more isotropic velocity shear.

It must be noted that further exploration of the FA measure suggests it is an extremely sensitive measure for such a noisy 'signal'. It is believed that comparing the eigenvalues with those from a random distribution, similar to the computation of the two-point cross-correlation function, would help extract a more robust measure of the velocity shear FA.

6.5. Halo Spin Parameter

The halo spin parameter (λ), first given by Peebles (1969) describes the excess amount of ordered coherent rotation relative to random motions (Bett et al. 2007). λ is dimensionless and defined for each halo as:

$$\lambda = \frac{J\sqrt{|E|}}{M^{5/2}G} \tag{35}$$

where J is the magnitude of the angular momentum vector $\mathbf{J}$, M is the mass of the halo, G is the gravitational constant and E is the total energy. In the linear regime, halo spin can be explained through tidal torque theory and the gravitational collapse of protohalos (Porciani et al. 2002). The acquisition of angular momentum originates due to tidal torques from local overdensities. However, this explanation is insufficient (Porciani et al. 2002). It has been shown by Vitvitska et al. (2002) that the origin of angular momentum may also be a result of halo satellite accretion and merging with other halos.

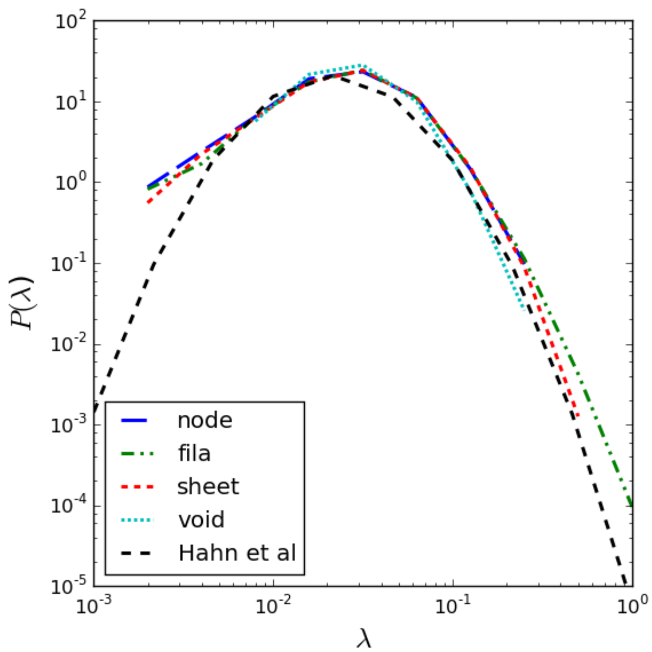

Fig. 25.— Probability density functions for node, sheet, filament and void halo spin. The black line is the log-normal fit given by Hahn et al. (2007b) with best fit parameters $\lambda_0 = 0.035$ and $\sigma = 0.7$.

The halo spin parameter has shown little dependence on mass or cosmology (Macciò et al. 2008). However, since it is a function of the merger history of the halo it would be natural to assume an environmental dependence. Fig. 25 shows the probability density functions for the spin parameter as a function of web type. The distribution can be fitted using a log-normal distribution of the form:

$$P(\lambda) = \frac{1}{\lambda\sigma\sqrt{2\pi}} exp\left[-\frac{ln^2(\lambda/\lambda_0)}{2\sigma^2}\right] \tag{36}$$

where the best fit parameters are determined by the shape parameter λ_0 and the scale parameter σ. For the halo sample in this analysis, the best fit parameters are found by Maximum Likelihood Estimates with $\lambda_0 = 0.032$ and $\sigma = 0.6$. The black dotted line in Fig. 25 shows the fit determined by Hahn et al. (2007b) with $\lambda_0 = 0.035$ and $\sigma = 0.7$.

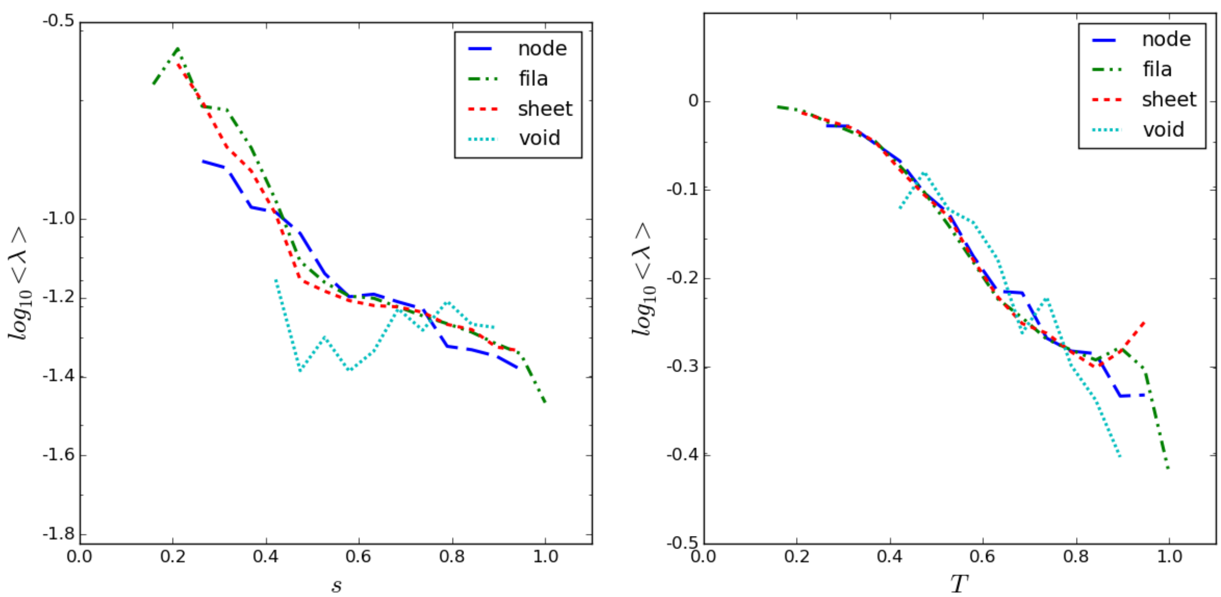

Fig. 26.— **Left panel**: sphericity as a function of median spin for the different web types. **Right panel**: triaxality as a function of median spin for cosmic web types. Higher spins are associated with a less spherical and more oblate halo shape. Spherical, prolate halos are correlated with low spins.

Fig. 25 shows little spin dependence on web type for low spin values. High spin halos are more associated with sheet and filament halos respectively. There are no node or void halos with a spin greater than ~ 0.3. These results echo the relationship found for the FA in Section 6.4. It has been established that halo properties depend greatly on the internal velocity structure of the halo itself (e.g. Faltenbacher & White 2010). Here one observes a manifestation of this dependence; it is suggested here that isotropic velocity shear negates the growth of linear angular momentum.

These results are in disagreement with Hahn et al. (2007b) who demonstrated, using the tidal tensor classification scheme and a low mass range ($M < 5 \times 10^{11}\, h^{-1} M_{\odot}$), that the highest spin halos in decreasing order are: nodes, sheets, filaments and voids. There was also a very weak web type-spin dependence for halos in the high mass range ($> 5 \times 10^{12}\, h^{-1} M_{\odot}$).

Finally, the correlation between spin and shape can be found in Fig. 26. Again, median sphericity and triaxality values are only shown where the bin particle count is greater than 10. Higher spin halos are less spherical and more oblate. Conversely, low spin halos are correlated with a more spherical but prolate halo. Voids show little spin-sphericity correlation while nodes, sheets and filaments exhibit increasingly stronger correlations. Prolate halos would be observed in instances where shearing rates on the major axis of the spheroid are significantly higher. Thus, low spin halos are expected to be more spherical.

There exists a weak correlation between web type spin and triaxality. All web types exhibit the same behaviour whereby high spin halos are more oblate while low spins are correlated with more prolate shapes. There are very few oblate void and node halos as is confirmed in Fig. 22. The strength of the divergent velocity field as well as the isotropic nature of the velocity shear ensures node and void halos have a relatively limited upper spin limit, which is then directly correlated with more prolate shapes. Sheets and filaments exhibit significant shear anisotropy, yielding strong tidal torques and higher spin, less spherical and more oblate halos.

7. Conclusion

> "Not only is the Universe stranger than we think, it is stranger than we can think."
>
> Werner Heisenberg

Nodes, sheets, filaments and voids are the components of the cosmic web that define the mass distribution of the Universe. These substructures are characterised by their regions of varying density, as well as the velocity structure of the objects found within these web types. Halo, and hence galaxy, morphology has been shown to vary significantly with the environment, therefore, understanding the link between morphology and environment is needed to establish a consistent theory of galaxy formation and evolution.

In an effort to explore the cosmic environment, various cosmic web classification algorithms have been proposed. This work details a new classification algorithm unique in its Lagrangian approach that uses SPH defined quantities to calculate the velocity shear experienced by particles or halos. The classification method is based on the approach given by Hoffman et al. (2012), who showed that a velocity shear based classification scheme offers better resolution and traces the density field better compared to other tidal torque based schemes.

This research report begins by looking at cosmological N-body simulations and how they are are used to simulate the gravitational collapse of dark matter particles. Various methods and algorithms are discussed with particular reference to the GADGET-2 simulation code and ROCKSTAR halo finder. The mathematical formalism of SPH is introduced in reference to the SPH defined shear tensor defined in the subsequent chapter.

Section 4 introduced the SPD classification methodology based on particles and halos. Compared to Eulerian based techniques, the newly proposed classification scheme has an adaptive resolution well suited to following the most massive regions of the simulation. The SPD approach calculates the velocity shear for a given object by incorporating information from an objects local neighbourhood that is defined within the kernel volume. The results exhibits comparable statistics with current literature.

A Lagrangian definition negates the use of a grid and can be directly applied to observed galaxy samples. When subhalos are included, one observes a few misclassified halos that contribute to low node fractions and background densities that are poorly correlated with web type. These background densities may be corrected for by assigning the highest density web type of a given halo-subhalo system to the entire system. Using main halos only improves the misclassification rate, higher infall dimensionality web type fractions and background densities significantly.

Theories detailing structure formation use the degree of halo clustering to test cosmological models. Halo clustering dependence on mass and assembly history has been well established. Section 5 uses the Millennium simulation data to look at the correlation between halo clustering and web type. It has been shown that higher infall dimensionality web types are associated with higher clustering statistics. Particularly for low mass halos, sheets and voids are underclustered at large separation scales. In the high mass regime, node halos exhibit strong bias while filaments show almost no bias. Sheets and voids are associated with more anti-bias respectively. Halo clustering has been shown to be dependant on the fraction of web types, at a given mass.

Finally, the web type dependence on halo shape, spin and fractional anisotropy is examined. At high masses, node and filament halos were shown to to be less spherical and more prolate relative to other lower density web types. This may be explained by the well established mass sphericity dependence, i.e. filament and node halos occupy the highest fraction of high mass halos per bin. Less spherical, more triaxial shaped halos have lower spins confirmed by the overall spin distribution for each web type. Web types with the highest spin in increasing order are given as: nodes, voids, sheets and filaments. Nodes and voids have similar, relatively low upper spin limits. It is suggested here this may be explained by the relatively isotropic collapse and expansion of the velocity shear for node and void halos respectively. Sheets and filament halos have a largely anisotropic velocity shear which may contribute to the growth of linear angular momentum and as a result halo spin.

The results hint that both the mass and assembly history (e.g. spin, shape, formation time) dependence of halo clustering may manifest itself in the properties of the halos classified as a particular web type. For example: nodes and filaments exhibit higher degrees of clustering in all mass ranges. Clustering in the low mass regime has been shown to be tightly correlated with formation time. Thus, in the low mass regime, nodes and filaments can be associated with halos that have formed earlier. This concurs with the idea of hierarchical structure formation; small overdensities in the early Universe will collapse at higher redshifts, forming substructure earlier on. The overdense regions will continue to attract matter as structures flow into one another becoming more dense and clustering more strongly.

REFERENCES

Aarseth, S. 2003, Gravitational N-Body Simulations: Tools and Algorithms, 1st edn., ed. P. Landshoff, D. Nelson, & S. Weinberg (Cambridge: Cambridge University Press)

Aarseth, S. J. & Hoyle, F. 1963, Monthly Notices of the Royal Astronomical Society, 126, 223

Allgood, B., Flores, R. a., Primack, J. R., Kravtsov, a. V., Wechsler, R. H., Faltenbacher, A., & Bullock, J. S. 2006, Monthly Notices of the Royal Astronomical Society, 367, 1781

Appel, A. W. 1985, SIAM Journal on Scientific and Statistical Computing, 6, 85

Aragón-Calvo, M. A., Jones, B. J. T., van de Weygaert, R., & van der Hulst, J. M. 2007a, Astronomy and Astrophysics, 474, 315

Aragón-Calvo, M. a., Platen, E., van de Weygaert, R., & Szalay, A. S. 2010a, The Astrophysical Journal, 723, 364

Aragón-Calvo, M. a., Van De Weygaert, R., & Jones, B. J. T. 2010b, Monthly Notices of the Royal Astronomical Society, 408, 2163

Aragón-Calvo, M. a., van de Weygaert, R., Jones, B. J. T., & van der Hulst, J. M. 2007b, The Astrophysical Journal, 655, L5

Bagla, J. S. & Padmanabhan, T. 1997, Pramana - Journal of Physics, 49, 161

Bardeen, J. M., Bond, J. R., Kaiser, N., & Szalay, A. S. 1986, The Astrophysical Journal, 304, 15

Barnes, J. & Hut, P. 1986, Nature, 324, 446

Basser, P. J. & Pierpaoli, C. 1996, Journal of magnetic resonance, Series B, 560

Behroozi, P. S., Wechsler, R. H., & Wu, H.-Y. 2013, The Astrophysical Journal, 762, 109

Benz, W. 1988, Computer Physics Communications, 48, 97

—. 1990, The Numerical Modelling of Nonlinear Stellar Pulsations, ed. J. R. Buchler (Dordrecht: Springer Netherlands), 269–288

Bertschinger, E. 1998, Annual Review of Astronomy and Astrophysics, 36, 599

Bertschinger, E. & Gelb, J. M. 1991, Computers in Physics, 5, 164

Bett, P., Eke, V., Frenk, C. S., Jenkins, A., Helly, J., & Navarro, J. 2007, Monthly Notices of the Royal Astronomical Society, 376, 215

Blanton, M. R., Eisenstein, D., Hogg, D. W., Schlegel, D. J., & Brinkmann, J. 2005, The Astrophysical Journal, 629, 143

Bond, J. R., Kofman, L., & Pogosyan, D. 1996, Nature, 380, 603

Bullock, J. 2002, The shapes of galaxies and their dark halos : Yale Cosmology Workshop : New Haven, Connecticut, USA, 28-30 May 2001

Cole, S. & Kaiser, N. 1989, Monthly Notices of the Royal Astronomical Society, 237, 1127

Cole, S. & Lacey, C. 1996, Monthly Notices of the Royal Astronomical Society, 281, 716

Colless, M., Dalton, G., Maddox, S., Sutherland, W., Norberg, P., Cole, S., Bland-Hawthorn, J., Bridges, T., Cannon, R., Collins, C., Couch, W., Cross, N., Deeley, K., De Propris, R., Driver, S. P., Efstathiou, G., Ellis, R. S., Frenk, C. S., Glazebrook, K., Jackson, C., Lahav, O., Lewis, I., Lumsden, S., Madgwick, D., Peacock, J. A., Peterson, B. A., Price, I., Seaborne, M., & Taylor, K. 2001, Monthly Notices of the Royal Astronomical Society, 328, 1039

Colombi, S., Pogosyan, D., & Souradeep, T. 2000, Physical review letters, 85, 5515

Croton, D. J., Gao, L., & White, S. D. M. 2007, Monthly Notices of the Royal Astronomical Society, 374, 1303

Dalal, N., White, M., Bond, J. R., & Shirokov, A. 2008, The Astrophysical Journal, 687, 12

Davis, M., Efstathiou, G., Frenk, C. S., & White, S. D. M. 1985, The Astrophysical Journal, 292, 371

Dressler, A. 1980, The Astrophysical Journal, 236, 351

Dubinski, J. & Carlberg, R. G. 1991, The Astrophysical Journal, 378, 496

Efstathiou, G., Davis, M., White, S. D. M., & Frenk, C. S. 1985, The Astrophysical Journal Supplement Series, 57, 241

Falck, B. L., Neyrinck, M. C., & Szalay, A. S. 2012, The Astrophysical Journal, 754, 126

Faltenbacher, A., Li, C., White, S. D. M., Jing, Y.-P., Mao, S., & Wang, J. 2009, Research in Astronomy and Astrophysics, 9, 41

Faltenbacher, A. & White, S. D. M. 2010, The Astrophysical Journal, 708, 469

Fisher, J. D., Faltenbacher, A., & Johnson, M. 2016, Monthly Notices of the Royal Astronomical Society, stw370

Forero-Romero, J. E., Hoffman, Y., Gottlöber, S., Klypin, A., & Yepes, G. 2009, Monthly Notices of the Royal Astronomical Society, 396, 1815

Franx, M., Illingworth, G., & de Zeeuw, T. 1991, The Astrophysical Journal, 383, 112

Frenk, C. S., White, S. D. M., Davis, M., & Efstathiou, G. 1988, The Astrophysical Journal, 327, 507

Gao, L., Springel, V., & White, S. D. M. 2005a, Monthly Notices of the Royal Astronomical Society: Letters, 363, L66

Gao, L. & White, S. D. M. 2007, Monthly Notices of the Royal Astronomical Society: Letters, 377, L5

Gao, L., White, S. D. M., Jenkins, A., Frenk, C. S., & Springel, V. 2005b, Monthly Notices of the Royal Astronomical Society, 363, 379

Gingold, R. A. and Monaghan, J. J. 1977, Monthly Notices of the Royal Astronomical Society, 181, 375

Gottloeber, S., Mueller, V., Muecket, J. P., & Wambsganss, J., eds. 1998, Large Scale Structure: Tracks and Traces, ed. S. Gottloeber, V. Mueller, J. P. Muecket, & J. Wambsganss

Hahn, O., Carollo, C. M., Porciani, C., & Dekel, A. 2007a, Monthly Notices of the Royal Astronomical Society, 381, 41

Hahn, O., Porciani, C., Carollo, C. M., & Dekel, A. 2007b, Monthly Notices of the Royal Astronomical Society, 375, 489

Hernquist, L. & Katz, N. 1989, The Astrophysical Journal Supplement Series, 70, 419

Hockney, R. W. & Eastwood, J. W. 1981, Computer Simulation Using Particles, 1st edn. (New York: McGraw-Hill)

Hoffman, Y., Metuki, O., Yepes, G., Gottlöber, S., Forero-Romero, J. E., Libeskind, N. I., & Knebe, A. 2012, Monthly Notices of the Royal Astronomical Society, 425, 2049

Holmberg, E. 1941, The Astrophysical Journal, 94, 385

Huchra, J., Davis, M., Latham, D., & Tonry, J. 1983, The Astrophysical Journal Supplement Series, 52, 89

Hultman, J. & Pharasyn, A. 1999, Astronomy & Astrophysics, 347, 769

Ivezić, v., Connolly, A. J., VanderPlas, J. T., & Gray, A. 2014, Statistics, Data Mining, and Machine Learning in Astronomy: A Practical Python Guide for the Analysis of Survey Data, Princeton Series in Modern Observational Astronomy (Princeton University Press)

Kaiser, N. 1984, The Astrophysical Journal, 284, L9

Kauffmann, G., White, S. D. M., & Guiderdoni, B. 1993, Monthly Notices of the Royal Astronomical Society, 264, 201

Kitaura, F.-S., Angulo, R. E., Hoffman, Y., & Gottlöber, S. 2012, Monthly Notices of the Royal Astronomical Society, 425, 2422

Kluźniak, W. & Lee, W. H. 1998, The Astrophysical Journal, 494, L53

Klypin, A. 2000, arXiv preprint astro-ph/0005502, 1

Klypin, A. A. & Shandarin, S. F. 1983, Monthly Notices of the Royal Astronomical Society, 204, 891

Knebe, A., Knollmann, S. R., Muldrew, S. I., Pearce, F. R., Aragon-Calvo, M. A., Ascasibar, Y., Behroozi, P. S., Ceverino, D., Colombi, S., Diemand, J., Dolag, K., Falck, B. L., Fasel, P., Gardner, J., Gottlöber, S., Hsu, C.-H., Iannuzzi, F., Klypin, A., Lukić, Z., Maciejewski, M., McBride, C., Neyrinck, M. C., Planelles, S., Potter, D., Quilis, V., Rasera, Y., Read, J. I., Ricker, P. M., Roy, F., Springel, V., Stadel, J., Stinson, G., Sutter, P. M., Turchaninov, V., Tweed, D., Yepes, G., & Zemp, M. 2011, Monthly Notices of the Royal Astronomical Society, 415, 2293

Kravtsov, A. V., Klypin, A. A., & Khokhlov, A. M. 1997, The Astrophysical Journal Supplement Series, 111, 73

Libeskind, N. I., Hoffman, Y., Forero-Romero, J., Gottlober, S., Knebe, A., Steinmetz, M., & Klypin, A. 2012a, Monthly Notices of the Royal Astronomical Society, 428, 2489

Libeskind, N. I., Hoffman, Y., & Gottlober, S. 2014, Monthly Notices of the Royal Astronomical Society, 441, 1974

Libeskind, N. I., Hoffman, Y., Knebe, A., Steinmetz, M., Gottlöber, S., Metuki, O., & Yepes, G. 2012b, Monthly Notices of the Royal Astronomical Society: Letters, 421, L137

Liu, G.-R. & Liu, M. B. 2003, Smoothed particle hydrodynamics: a meshfree particle method (World Scientific)

Lucy, L. B. 1977, The Astronomical Journal, 82, 1013

Macciò, A. V., Dutton, A. a., & van den Bosch, F. C. 2008, Monthly Notices of the Royal Astronomical Society, 391, 1940

Metuki, O., Libeskind, N. I., Hoffman, Y., Crain, R. a., & Theuns, T. 2014, Monthly Notices of the Royal Astronomical Society, 446, 1458

Mo, H. J. & White, S. D. M. 1996, Monthly Notices of the Royal Astronomical Society, 282, 347

Monaghan, J. 1985, Computer Physics Reports, 3, 71

Monaghan, J. J. 1992, Annual Review of Astronomy and Astrophysics, 30, 543

Monaghan, J. J. & Lattanzio, J. 1985, Astronomy and Astrophysics, 149, 135

Monaghan, J. J. & Lattanzio, J. C. 1991, The Astrophysical Journal, 375, 177

Morris, J. P. 1996, Analysis of smoothed particle hydrodynamics with applications (Monash University Australia)

Nuza, S. E., Kitaura, F.-S., Hess, S., Libeskind, N. I., & Mueller, V. 2014, Monthly Notices of the Royal Astronomical Society, 445, 15

Peebles, P. J. E. 1969, The Astrophysical Journal, 155, 393

—. 1970, The Astronomical Journal, 75, 13

Peebles, P. J. E. 1980, The large-scale structure of the universe (Princeton, N.J.: Princeton University Press)

Peter, A. H. G. 2012, arXiv preprint astro-ph/1201.3942, 15

Platen, E., Van De Weygaert, R., & Jones, B. J. T. 2007, Monthly Notices of the Royal Astronomical Society, 380, 551

Porciani, C., Dekel, A., & Hoffman, Y. 2002, Monthly Notices of the Royal Astronomical Society, 332, 325

Press, W. H. & Schechter, P. 1974, The Astrophysical Journal, 187, 425

Price, D. 2012, Journal of Computational Physics, 231, 759

Schaap, W. E. & van de Weygaert, R. 2000, Astron. Astrophys., 363, L29

Sousbie, T. 2011, Monthly Notices of the Royal Astronomical Society, 414, 350

Springel, V. 2005, Monthly Notices of the Royal Astronomical Society, 364, 1105

—. 2010, Annual Review of Astronomy and Astrophysics, 48, 391

Springel, V., White, S. D. M., Jenkins, A., Frenk, C. S., Yoshida, N., Gao, L., Navarro, J., Thacker, R., Croton, D., Helly, J., Peacock, J. a., Cole, S., Thomas, P., Couchman, H., Evrard, A., Colberg, J., & Pearce, F. 2005a, Nature, 435, 629

—. 2005b, Nature, 435, 629

Steinmetz, M. & Navarro, J. F. 2002, New Astronomy, 7, 155

Vitvitska, M., Klypin, A. A., Kravtsov, A. V., Wechsler, R. H., Primack, J. R., & Bullock, J. S. 2002, The Astrophysical Journal, 581, 799

von Hoerner, S. 1960, Z. Astrophys, 50, 184

Warren, M. S., Quinn, P. J., Salmon, J. K., & Zurek, W. H. 1992, The Astrophysical Journal, 399, 405

White, S. D. M. 1976, Monthly Notices of the Royal Astronomical Society, 177, 717

Xu, G. 1995, The Astrophysical Journal Supplement Series, 98, 355

York, D. G., Adelman, J., Anderson, Jr., J. E., Anderson, S. F., Annis, J., Bahcall, N. A., Bakken, J. A., Barkhouser, R., Bastian, S., Berman, E., Boroski, W. N., Bracker, S., Briegel, C., Briggs, J. W., Brinkmann, J., Brunner, R., Burles, S., Carey, L., Carr, M. A., Castander, F. J., Chen, B., Colestock, P. L., Connolly, A. J., Crocker, J. H., Csabai, I., Czarapata, P. C., Davis, J. E., Doi, M., Dombeck, T., Eisenstein, D., Ellman, N., Elms, B. R., Evans, M. L., Fan, X., Federwitz, G. R., Fiscelli, L., Friedman, S., Frieman, J. A., Fukugita, M., Gillespie, B., Gunn, J. E., Gurbani, V. K., de Haas, E., Haldeman, M., Harris, F. H., Hayes, J., Heckman, T. M., Hennessy, G. S., Hindsley, R. B., Holm, S., Holmgren, D. J., Huang, C.-h., Hull, C., Husby, D., Ichikawa, S.-I., Ichikawa, T., Ivezić, v., Kent, S., Kim, R. S. J., Kinney, E., Klaene, M., Kleinman, A. N., Kleinman, S., Knapp, G. R., Korienek, J., Kron, R. G., Kunszt, P. Z., Lamb, D. Q., Lee, B., Leger, R. F., Limmongkol, S., Lindenmeyer, C., Long, D. C., Loomis, C., Loveday, J., Lucinio, R., Lupton, R. H., MacKinnon, B., Mannery, E. J., Mantsch, P. M., Margon, B., McGehee, P., McKay, T. A., Meiksin, A., Merelli, A., Monet, D. G., Munn, J. A., Narayanan, V. K., Nash, T., Neilsen, E., Neswold, R., Newberg, H. J., Nichol, R. C., Nicinski, T., Nonino, M., Okada, N., Okamura, S., Ostriker, J. P., Owen, R., Pauls, A. G., Peoples, J., Peterson, R. L., Petravick, D., Pier, J. R., Pope, A., Pordes, R., Prosapio, A., Rechenmacher, R., Quinn, T. R., Richards, G. T., Richmond, M. W., Rivetta, C. H., Rockosi, C. M., Ruthmansdorfer, K., Sandford, D., Schlegel, D. J., Schneider, D. P., Sekiguchi, M., Sergey, G., Shimasaku, K., Siegmund, W. A., Smee, S., Smith, J. A., Snedden, S., Stone, R., Stoughton, C., Strauss, M. A., Stubbs, C., SubbaRao, M., Szalay, A. S., Szapudi, I., Szokoly, G. P., Thakar, A. R., Tremonti, C., Tucker, D. L., Uomoto, A., Vanden Berk, D., Vogeley, M. S., Waddell, P., Wang, S.-i., Watanabe, M., Weinberg, D. H., Yanny, B., & Yasuda, N. 2000, The Astronomical Journal, 120, 1579

Zel'dovich, Y. B. 1970, Astronomy & Astrophysics, 5, 84

This preprint was prepared with the AAS LaTeX macros v5.2.

A. Appendix A: Coursework Information & Funding

Masters coursework was undertaken at the National Astrophysics and Space Science Programme (NASSP) hosted at the University of Cape Town. Subjects included:

- Computational Astrophysics
- Advanced General Relativity
- Theoretical Cosmology
- Observational Cosmology
- Extra-galactic Astrophysics

The final average was given as 90%. The official transcript can be found in the following pages. The student was generously supported by NASSP and is awaiting the final bursary payment for fees owed to the University of the Witwatersrand. A letter from NASSP detailing the funding arrangement as well as the fee statement can be found in the following pages as well.

UNIVERSITY OF CAPE TOWN

OFFICIAL TRANSCRIPT

Statement of Academic Record

Name : Fisher,Justin David

Campus ID : FSHJUS004

Birthdate : 1990-01-15

Student Records Office
University of Cape Town
Private Bag X3
Rondebosch
7701
South Africa

Telephone: (021) 650-3595
Fax : (021) 650-5714

----- **Beginning of Honours Record** -----

2014

Programme: BSc (Honours)

Plan : Astrophysics & Space Science Specialisation

Course		Description	Credits Taken	Credits Earned	Result	
AST	4007W	Honours in Astro & Space Sci	160	160	84	1
		Class Medal: AST4007W				

Qualifies for award of degree/diploma

Degree : Bachelor of Science Honours
Confer Date : 2014-12-15
Degree Honours: in the first class
Plan : Astrophysics and Space Science

----- **Beginning of Masters Record** -----

2015

Programme: MSc (90 crsewrk/90 diss)

Plan : Astrophysics & Space Science Specialisation

Course		Description	Credits Taken	Credits Earned	Result	
AST	5003F	Astro & Space Sci Coursework	90	90	90	1

----- **Scholarships and Grants** -----

2015	Manuel & Luby Washkansky Sch	10000.00

The conduct of the Student was satisfactory.

----- **End of Transcript** -----

UNIVERSITY OF CAPE TOWN
S. RICH
FOR REGISTRAR

Registrar

See overleaf for an explanation of symbols used

Issued on 2015/08/04 at 03:21:07PM

SR778M

NASSP

Astrophysics, Cosmology and Gravity Centre (ACGC) - Department of Astronomy

Email: heyden@ast.uct.ac.za **Web site:** www.ast.uct.ac.za

University of Cape Town, Private Bag X3, Rondebosch 7701,
South Africa

Telephone: +27 21 650 4042 Fax: +27 21 650 4547

18 March 2016

To Whom It May Concern

JUSTIN DAVID FISHER

This letter serves to inform you that the abovementioned student is a National Astrophysics and Space Science Programme (NASSP) bursary holder and that NASSP will pay for his tuition in full once we receive our NRF funding which will be hopefully before the end of March 2016.

Should you require any additional information regarding this matter, please feel free to contact me on the following number (021) 650 2346.

Kind Regards

Mr O Kwayiba
NASSP ADMINISTRATOR

Fee Statement

University of the Witwatersrand, Johannesburg
Tel: +27 11 717-1888
Fax: +27 11 717-4918
E-mail: feesoffice.finance@wits.ac.za
Private Bag 3, WITS 2050
VAT No: 4390128942

Bill From: 01-01-2016 **to** 05-06-2016

Student Name	Justin Fisher
Student Number	302186
Year of Study	YS1
Degree of Registration	Master of Science (CW/RR)

Creation Date	Unit Code	Unit Description	Fee Type	Amount (In Rands)
Opening Balance				
01-Jan-16	Opening Balance			8,237.45
Academic Charges				
			Total Academic Charges:	**0.00**
Additional Charges/Credits				
26-Feb-16			Interest Charges February	72.08
			Total Additional Charges:	**72.08**
Housing Charges/Credits				
			Total Housing Charges / Credits:	**0.00**
Payments/Misc. Credits				
24-Mar-16			Payment for Student Fees	-120.00
16-May-16			Physics Bursaries And Student	-8,189.53
			Total Payments:	**-8,309.53**
TOTAL DUE:				**0.00**

***Standard VAT was charged on this Item @14%**

Internet Payments

Banking Details	Standard Bank of South Africa
Account Number	002 891 697
Branch	Braamfontein
Branch Code	004 805
Reference Number	**302186**

Online Payments

1. Click on student self-service portal and log on.
2. Click on student financials
3. Click on "Make a Payment"

Make an Online Payment (Click Here)